TECHNICAL REPORT R-85

A NONLINEAR THEORY FOR PREDICTING THE EFFECTS OF UNSTEADY LAMINAR, TURBULENT, OR TRANSITIONAL BOUNDARY LAYERS ON THE ATTENUATION OF SHOCK WAVES IN A SHOCK TUBE WITH EXPERIMENTAL COMPARISON

By ROBERT L. TRIMPI and NATHANIEL B. COHEN

Langley Research Center
Langley Field, Va.

TECHNICAL REPORT R-85

A NONLINEAR THEORY FOR PREDICTING THE EFFECTS OF UNSTEADY LAMINAR, TURBULENT, OR TRANSITIONAL BOUNDARY LAYERS ON THE ATTENUATION OF SHOCK WAVES IN A SHOCK TUBE WITH EXPERIMENTAL COMPARISON [1]

By Robert L. Trimpi and Nathaniel B. Cohen

SUMMARY

The linearized attenuation theory of NACA Technical Note 3375 is modified in the following manner: (a) an unsteady compressible local skin-friction coefficient is employed rather than the equivalent steady-flow incompressible coefficient; (b) a nonlinear approach is used to permit application of the theory to large attenuations; and (c) transition effects are considered. Curves are presented for predicting attenuation for shock pressure ratios up to 20 and a range of shock-tube Reynolds numbers. Comparison of theory and experimental data for shock-wave strengths between 1.5 and 10 over a wide range of Reynolds numbers shows good agreement with the nonlinear theory evaluated for a transition Reynolds number of 2.5×10^6.

INTRODUCTION

The increasingly widespread use of the shock tube as an aerodynamic testing facility has led to the closer investigation of the flows present in such tubes. In particular, since the deviation of these flows from those predicted by perfect fluid theory is often of large magnitude, these deviations have been investigated fairly thoroughly. Several such studies, either of an experimental or theoretical nature, may be found in references 1 to 11. Investigations of the boundary layers in shock tubes have been made in some of the aforementioned references as well as in references 12 to 17. This list of references does not cover the complete field of literature existing on these topics but is representative of the various general treatments.

Consideration of the entire flow field from the leading edge of the expansion wave to the shock wave is necessary to obtain an accurate picture of the waves traveling along the shock tube. These waves are responsible for the deviations from perfect fluid flow in shock-wave strength (attenuation) with distance, in pressure and density at a given distance with time, and so forth, which have been noted by various investigators. The analysis of reference 1 was the first to treat this complete flow. Figure 1, a reproduction with minor changes of figure 1 of reference 1, is the basic wave diagram of the unperturbed shock-tube flow showing the various flow regions to be considered with typical characteristics and particle paths. This linearized analysis (ref. 1) was based on an averaged one-dimensional nonsteady flow in which wall-shear

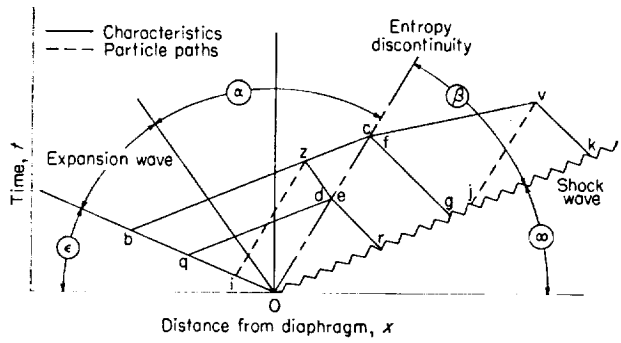

FIGURE 1.—Distance-time plot of shock-tube flow.

[1] Supersedes NACA Technical Note 4347 by Robert L. Trimpi and Nathaniel B. Cohen, 1958.

and heat-transfer effects generated pressure waves to perturb the perfect fluid flow. This averaging process essentially implied thick boundary layers. The expansion wave was treated as a "negative shock" or zero-thickness wave. The resulting perturbation equations then hinged on the evaluation of the local skin-friction coefficient c_f, which in reference 1 was assumed to be given by an equivalent incompressible steady flow. Consequently, the application of the results of reference 1 was limited to shock pressure ratios in which this assumption for c_f was valid, although the analysis was still applicable for other pressure ratios when the proper choice of c_f was employed. The assumption of incompressibility should apparently eliminate the strong shock pressure ratios from the range of validity.

Solutions to the laminar boundary-layer equations employing a linear viscosity-temperature relation (refs. 2, 3, and 14) show that the nonsteady character of the flow is such that the equivalent laminar steady-flow assumption is in error, irrespective of compressibility, for most conditions except that existing in the cold-gas region α for strong shock waves. On the other hand, the turbulent boundary layer is not nearly so sensitive to the unsteady character of the flow. Reference 15, which assumed a one-seventh-power velocity profile similar to that of reference 1, reported that even for infinite shock pressure ratios the effect of unsteadiness would produce only a maximum variation in turbulent skin friction of 5 percent in the cold gas and of 22 percent in the hot gas.

The only other attenuation analysis to date that considers the entire flow field is that of reference 2. This analysis is similar to that of reference 1 in that it is a small-perturbation approach using traveling waves and a negative shock, the major difference being that the pressure-wave generations arise because the boundary-layer-displacement thickness changes with time. (The boundary-layer-displacement thicknesses of ref. 15 are used.) Flows with thin boundary layers having a linear viscosity-temperature variation are required for this treatment to apply. The attenuations predicted by references 1 and 2 for turbulent boundary layers agreed within 10 percent for shock-pressure ratios up to 6 in spite of the marked differences assumed in the mechanism for handling the wall effects. The perturbations in the flow behind the shock show a larger difference between the two approaches.

The deviations from ideal theory discussed arise for the most part from wall effects, that is, the perturbations in the shock-tube flow caused by wall shear and heat transfer. Much recent work has been done using the shock tube as a testing medium to provide very high-temperature flows of short duration. (See, for example, refs. 9 and 18.) In these cases, deviations from ideal fluid flow will also arise because the air at high temperatures does not behave as an ideal fluid. It would be difficult to separate the real-gas effects from the wall effects; therefore, the present analysis, like those of references 1 and 2, is concerned only with the effects of wall boundary layer upon the inviscid outer flow, the fluid being considered as an ideal gas.

The turbulent theory of reference 1 has been compared with experimental data for attenuation in references 1, 7, 8, and 10 and good agreement has been found in general. Predicted pressure perturbations in the hot gas by the method of reference 1 agreed well with the experimental results reported in the same paper. Fair to good agreement between theory and experiment is reported in references 7 and 10 for the hot-gas average density variation with time in the flow behind the shock wave; poor agreement is reported for the cold-gas flow where the finite expansion fan has been treated as a negative shock.

Since the deviations from the inviscid fluid flow often become large in cases of aerodynamic shock-tube testing, the linear, or small-perturbation, theories of references 1 and 2 are no longer applicable and recourse must be made to some sort of nonlinear approach.

In order to obtain an exact theory for predicting the perturbations in a shock-tube flow, a rigorous treatment would be required first to the solution of the boundary-layer flows. The boundary-layer equations would have to be solved not only in region β but also inside and after the expansion fan which is considered to be of finite extent. For laminar flows the main difficulty would probably be the correct handling of the viscosity variation across the boundary layer. For turbulent flow a rigorous treatment appears to be impossible without a tremendous increase in knowledge of the mechanics of turbulence. Once the boundary-layer solutions were determined, the vertical

velocity at the edge of the boundary layer could, if the boundary layers were thin, be used in the manner of reference 2 to determine the local pressure waves generated.

The second major difficulty in obtaining a rigorous perturbation solution would arise from the treatment of the entropy discontinuity. The theoretical contact surface increases in extent with distance progressed down the shock tube due to mixing and diffusion (the former is the major influence). This process not only generates pressure waves but also alters the reflected and transmitted wave strengths of the pressure waves generated by the boundary layers.

If a rigorous solution such as that just described was available, then it would without question be the one to be employed. The theory of reference 1 and the theory of the present report assume that the wall effects can be averaged across the flow. This assumption introduces errors because no such physical mechanism exists for the instantaneous transmission of these effects across the flow. In the absence of the rigorous solution there is no evidence to indicate that the errors introduced by a shock-tube perturbation theory based on an averaging process are of a larger magnitude than those introduced by the neglect of the aforementioned considerations required for a rigorous solution. In addition, there is the possibility that an averaging process might be more applicable as the boundary layer fills a greater part of the shock-tube cross-sectional area. Consequently, the extension of the method of reference 1 in the present analysis is justified.

In the present paper the analysis of reference 1 is first modified to eliminate the restrictions imposed by the incompressible equivalent steady-flow assumption for local skin friction; and then a nonlinear theory is derived which permits application of the analysis to large attenuations. It will be assumed that the reader is familiar with the basic theory and assumptions of reference 1 so that repetition in this paper may be avoided. This modified theory will be compared with experimental data covering a wide range of flow variables. The theoretical and experimental studies reported herein were conducted at the Gas Dynamics Branch of the Langley Laboratory during 1955 and 1956.

SYMBOLS

a velocity of sound

$C_f=\frac{1}{\xi}\int_0^{\xi} c_f(\xi)\,d\xi$

C_n constant defined by equation (8)

c_f local skin-friction coefficient, $2\tau_w/\rho U^2$

c_v coefficient of specific heat at constant volume

c_p coefficient of specific heat at constant pressure

D hydraulic diameter, $\frac{4\times\text{Area}}{\text{Perimeter}}$

$E=1+\frac{U_w}{U_w-U}\left(\frac{\delta^*}{\theta}-1\right)$

$f_{xm}, f_{xn}, g_{xm}, g_{xn}$ functions defined by equation (39b)

$F_n=\left(2\frac{n+1}{n+3}\frac{\theta}{\delta}\right)^{\frac{2}{n+3}} C_n^{\frac{n+1}{n+3}}$

G_m or G_n constant defined by equation (36)

$\hat{g}_n=Kg_n$

K ratio of contributions of $\hat{P}$ waves to total waves generated in region β, $\frac{\sigma M_s-M_\beta}{1+M_\beta-\sigma M_s}\left(\frac{\phi \hat{P}_{,\beta}}{\Gamma_\beta}\right)$

L_n or $_{\tau,n}$ or $_{\tau}$ linear attenuation with first subscript describing boundary layer appropriate to region α and second subscript to region β; that is, $L_{\tau\,\tau,}=\frac{p_{vs}-p_{\beta o}}{p_\infty}$ for region α turbulent with $n=7$ and region β as transitional

l fixed distance along shock-tube axis

l^* distance the shock moves from a given point until the effects of transition in the flow generated at that point first influences the shock

$M=U/a$

$M_\alpha=U/a_\alpha$

$M_\beta=U/a_\beta$

$M_s=U_s/a_\infty$

m or n reciprocal of velocity exponent in boundary layer, $\frac{u}{U}=\left(\frac{y}{\delta}\right)^{\frac{1}{m}\text{ or }\frac{1}{n}}$

N arbitrarily denotes subdivisions I, II, III, etc. of hot-gas region

$NL_{n \text{ or } \tau,n \text{ or } \tau}$ nonlinear attentuation with first subscript describing boundary layer appropriate to region α and second subscript to region β

N_{Pr} Prandtl number

P,Q characteristic parameter, $\frac{2c_v}{R}a\pm U$

$\hat{P},\hat{Q}$ effective characteristic wave parameter defined by equations (43)

p static pressure

R gas constant; Reynolds number $\frac{U\xi}{\nu}$

R^* Reynolds number of transition, $\frac{U\xi^*}{\nu}$

S entropy

T temperature

T_w wall temperature

T_{aw} adiabatic wall temperature

t time

U free-stream velocity

U_s shock velocity

U_W velocity of wave which generates flow

u velocity in boundary layer

x distance along shock tube from diaphragm station

y distance from surface

Z_N function defined by equation (B12)

Γ function defined in equations (31)

γ ratio of specific heats, c_p/c_v; assumed as 1.40 for computations

Δl length of segment into which shock tube is divided for nonlinear treatment

$\frac{\Delta(\ )}{\Delta x}$ characteristic derivative in boundary layer, $\frac{\partial(\ )}{\partial x}+\frac{1}{U}\frac{\delta^*}{\theta}\frac{\partial(\ )}{\partial t}$

$\frac{\Delta(\ )}{\Delta \xi}$ characteristic derivative in boundary layer, $\frac{\partial}{\partial \xi}+\frac{1}{U}\frac{\delta^*}{\theta}\frac{1}{E}\frac{\partial(\ )}{\partial t}$

δ boundary-layer thickness; also indicates differential quantity

δ^* boundary-layer displacement thickness, $\int_0^\infty\left(1-\frac{u}{U}\right)dy$

$\frac{\delta(\ )}{\delta t}$ characteristic derivative in potential flow, $\frac{\partial(\ )}{\partial t}+(U\pm a)\frac{\partial(\ )}{\partial x}$

$\left(\frac{\delta\hat{p}}{p}\right)_\beta$ contribution to attentuation due to $\hat{P}$ waves in region β

$\eta=\frac{a_\epsilon}{a_\alpha}$

η_r	recovery factor, assumed equal to 0.85 for laminar flow and 0.90 for turbulent flow
θ	boundary-layer momentum thickness, $\int_0^\infty \frac{u}{U}\left(1-\frac{u}{U}\right)dy$
θ_o	boundary-layer momentum thickness at $\xi=\xi_o$
$\kappa=\frac{\xi_d}{\xi^*}$ for $\xi^*>\xi_d$ and if $\xi^*\leqq\xi_d$, its value is 1	
μ	coefficient of viscosity
ν	coefficient of kinematic viscosity
ξ	distance flow has progressed along surface
ξ_d	distance flow has progressed along surface at entropy discontinuity
ξ_o	distance flow has progressed along surface when $\theta=\theta_o$
ξ^*	distance flow has progressed along surface at transition
ρ	density
$\sigma=\frac{a_\infty}{a_\beta}$	
τ_w	wall shearing stress
$\phi_{P,\alpha}, \phi_{P,\beta}, \phi_{Q,\beta}, \phi_{s,\alpha}, \phi_{s,\beta}$	influence coefficients, defined in appendix A
$\phi_{\hat{P}}, \phi_{\hat{Q}}$	influence coefficients defined by equations (44)
Ω_m or Ω_n	compressibility correction
ω	exponent in viscosity-temperature law, $\mu\approx T^\omega$
I, II, III, etc.	subdivisions of hot-gas region β for nonlinear treatment (see fig. 8)

Subscripts:

Letter subscripts not included in the symbols defined above refer, in general, to values at points or within regions shown in figure 1. Numbered subscripts refer to points in figures 8 and 9. Exceptions to be noted, however, are as follows:

m,n	refers to velocity profile parameter m,n
o	perfect-fluid value
t	at time t
vs	evaluated immediately behind shock, that is, point v located at $x=U_s t$
x	at distance x
T	denotes attenuation with transition
χ	arbitrary condition in shock-tube free stream
std	denotes NACA standard atmospheric conditions

A prime on a symbol indicates a quantity evaluated at reference temperature.

THEORY

DERIVATION OF EXPRESSIONS FOR LOCAL SKIN-FRICTION COEFFICIENT

The skin-friction coefficient for the flow behind wave-induced flows will be found by an integral method. An incompressible skin-friction coefficient will first be determined and then a simple compressibility correction will be applied.

The integrated equation of motion for the incompressible boundary layer with zero pressure gradient is (see ref. 14):

$$\left(\frac{\partial\theta}{\partial x}\right)_t+\frac{1}{U}\left(\frac{\partial\delta^*}{\partial t}\right)_x=\frac{\tau_w}{\rho U^2}=\frac{1}{2}c_f \tag{1}$$

The form parameter δ^*/θ is assumed to be constant; this has been shown to be true for the unsteady wave-induced laminar flow (see ref. 14) but has not been completely established for turbulent flows. Equation (1) then becomes

$$\left(\frac{\partial\theta}{\partial x}\right)_t+\frac{1}{U}\frac{\delta^*}{\theta}\left(\frac{\partial\theta}{\partial t}\right)_x=\frac{1}{2}c_f \tag{2}$$

Since the resulting expression for c_f will ultimately be used in the attenuation formulas wherein the integral $\int c_f(\xi)d\xi$ is desired, the variable ξ is introduced. The variable ξ is defined as the distance a particle in the free stream has moved to reach the point (x,t) since acceleration by the passing wave which originated at $x=0$ at $t=0$ and which travels with velocity U_W. Thus,

$$\xi(x,t)=\frac{U}{U_W-U}(U_W t-x) \tag{3}$$

In the case of flow in a shock tube, the value of U_w is U_s for the flows induced by shock waves. If the assumption of reference 1 is followed and the expansion wave replaced by a wave of zero thickness, moving with the speed of the leading edge of the original expansion wave, then $U_w=-a_e$.

The differential equation (2) is transformed from the x,t coordinate system to the ξ,t system by using the following derivatives:

$$\left.\begin{aligned}\left(\frac{\partial f}{\partial x}\right)_t&=\left(\frac{\partial f}{\partial \xi}\right)_t\left(\frac{\partial \xi}{\partial x}\right)_t=-\frac{U}{U_w-U}\left(\frac{\partial f}{\partial \xi}\right)_t\\ \left(\frac{\partial f}{\partial t}\right)_x&=\left(\frac{\partial f}{\partial \xi}\right)_t\left(\frac{\partial \xi}{\partial t}\right)_x+\left(\frac{\partial f}{\partial t}\right)_\xi\\ &=\frac{UU_w}{U_w-U}\left(\frac{\partial f}{\partial \xi}\right)_t+\left(\frac{\partial f}{\partial t}\right)_\xi\end{aligned}\right\} \quad (4)$$

Thus equation (2) becomes

$$\left(\frac{\partial \theta}{\partial \xi}\right)_t+\frac{1}{U}\frac{\delta^*}{\theta}\frac{1}{E}\left(\frac{\partial \theta}{\partial t}\right)_\xi=\frac{1}{2E}c_f \quad (5)$$

where

$$E=1+\frac{U_w}{U_w-U}\left(\frac{\delta^*}{\theta}-1\right) \quad (6)$$

Now equations (2) and (5) are differential equations capable of solution by application of the method of characteristics. The slopes of the characteristics are

$$\frac{\Delta t}{\Delta x}=\frac{1}{U}\frac{\delta^*}{\theta}$$

for equation (2) and

$$\frac{\Delta t}{\Delta \xi}=\frac{1}{U}\frac{\delta^*}{\theta}\frac{1}{E}$$

for equation (5).

Thus, if the symbol $\Delta f/\Delta\xi$ is used to denote the derivative along a characteristic of slope $\Delta t/\Delta\xi$, equation (5) may be written as

$$\frac{\Delta \theta}{\Delta \xi}=\frac{1}{2E}c_f \quad (7)$$

For steady-flow boundary layers with zero pressure gradient, it has been established that $c_f=c_f(\delta,U,\nu)$. If this relation is assumed to hold for unsteady flows in the same form as for steady flows, then

$$c_f=C_n\left(\frac{U\delta}{\nu}\right)^{-\frac{2}{n+1}} \quad (8)$$

For turbulent flows n is the reciprocal of the exponent in the fractional power expression $\frac{u}{U}=\left(\frac{y}{\delta}\right)^{1/n}$ used to describe the turbulent boundary-layer velocity profiles. For laminar flows the value of n is one. The C_n terms are arbitrary constants to be evaluated later and may be completely different for the steady and unsteady flows.

Combining equations (8) and (7) and integrating yields:

$$\frac{\Delta\theta}{\Delta\xi}=\frac{1}{2E}C_n\left(\frac{U}{\nu}\frac{\delta}{\theta}\right)^{-\frac{2}{n+1}}\theta^{-\frac{2}{n+1}} \quad (9)$$

$$\int_{\theta_o}^{\theta}\theta^{\frac{2}{n+1}}\Delta\theta=\frac{C_n}{2E}\left(\frac{\nu}{U}\frac{\theta}{\delta}\right)^{\frac{2}{n+1}}\int_{\xi_o}^{\xi}\Delta\xi \quad (10)$$

$$\theta=\left[\theta_o^{\frac{n+3}{n+1}}+\frac{n+3}{n+1}\frac{C_n}{2E}\left(\frac{\nu}{U}\frac{\theta}{\delta}\right)^{\frac{2}{n+1}}(\xi-\xi_o)\right]^{\frac{n+1}{n+3}} \quad (11)$$

Substituting equation (11) into equation (8) to obtain c_f as a function of ξ yields:

$$c_f(\xi)=\left(2\frac{n+1}{n+3}E\frac{\theta}{\delta}\right)^{\frac{2}{n+3}}C_n^{\frac{n+1}{n+3}}\left[\frac{n+1}{n+3}\theta_o^{\frac{n+3}{n+1}}\frac{2E}{C_n}\left(\frac{\delta}{\theta}\right)^{\frac{2}{n+1}}\left(\frac{U}{\nu}\right)^{\frac{n+3}{n+1}}+\frac{U}{\nu}(\xi-\xi_o)\right]^{-\frac{2}{n+3}} \quad (12a)$$

$$c_f(\xi)=F_nE^{\frac{2}{n+3}}\left[\frac{n+1}{n+3}\frac{2E}{C_n}\left(\frac{\delta}{\theta}\right)^{\frac{2}{n+1}}\left(\frac{U\theta_o}{\nu}\right)^{\frac{n+3}{n+1}}+\frac{U}{\nu}(\xi-\xi_o)\right]^{-\frac{2}{n+3}} \quad (12b)$$

For the special case of $\theta_o=0$ at ξ_o which corresponds to flow initiation at ξ_o there results

$$c_f(\xi)=F_nE^{\frac{2}{n+3}}\left[\frac{U}{\nu}(\xi-\xi_o)\right]^{-\frac{2}{n+3}} \quad (12c)$$

The values of the various F_n terms, which are directly related to the hitherto arbitrary C_n values, will now be determined to match known solutions for certain limiting cases. If the ratio U_w/U becomes infinitely large, the solution must be the same as that for an infinite flat plate in contact with a fluid impulsively started from rest

at time $t=0$. Under these conditions

$$\left.\begin{aligned} &\xi-\xi_o=Ut \\ &E=\frac{\delta^*}{\theta} \\ &c_f(\xi)=F_n\left(\frac{\delta^*}{\theta}\right)^{\frac{2}{n+3}}\left(\frac{U^2t}{\nu}\right)^{-\frac{2}{n+3}} \end{aligned}\right\} \tag{13}$$

The solution, known as the Rayleigh solution, to such an impulsive laminar flow over a plate is

$$\left.\begin{aligned} &c_f(\xi)=1.128\left(\frac{U^2t}{\nu}\right)^{-1/2} \\ &\left(\frac{\delta^*}{\theta}\right)_{Rayleigh}=2.469 \end{aligned}\right\} \tag{14}$$

Consequently, in order to match the Rayleigh solution for the laminar case ($n=1$)

$$F_1\left(\frac{\delta^*}{\theta}\right)^{1/2}=1.128$$

or

$$F_1=0.718 \tag{15}$$

On the other hand, if U_W/U becomes infinitely small, the solution must be the same as that over a semi-infinite flat plate in steady flow (that is, the so-called Blasius problem). For these conditions

$$\left.\begin{aligned} &E=1.0 \\ &c_f(\xi)=F_n\left(U\frac{\xi-\xi_o}{\nu}\right)^{-\frac{2}{n+3}} \end{aligned}\right\} \tag{16}$$

whereas the corresponding form of the Blasius solution for laminar flow is

$$\left.\begin{aligned} &c_f=0.664\left[\frac{U}{\nu}(\xi-\xi_o)\right]^{-1/2} \\ &\left(\frac{\delta^*}{\theta}\right)_{Blasius}=2.605 \end{aligned}\right\} \tag{17}$$

Thus, if the Blasius solution were to be matched, it would be necessary for

$$F_1=0.664$$

Two possible solutions are then available for the laminar incompressible-flow case depending upon which limiting value is matched:

569768--61——2

Rayleigh limit $\left(\frac{U_W}{U}\to\infty\right)$:

$$(c_f)_{n=1}(\xi)=0.718\left(1+1.469\frac{U_W}{U_W-U}\right)^{1/2}\left[\frac{U}{\nu}(\xi-\xi_o)\right]^{-1/2} \tag{18a}$$

Blasius limit $\left(\frac{U_W}{U}\to 0\right)$:

$$(c_f)_{n=1}(\xi)=0.664\left(1+1.605\frac{U_W}{U_W-U}\right)^{1/2}\left[\frac{U}{\nu}(\xi-\xi_o)\right]^{-1/2} \tag{18b}$$

In figure 2 the values for $c_f\sqrt{\frac{U}{\nu}(\xi-\xi_o)}$ as determined by four different means are plotted against pressure ratio across a shock in an air-air shock tube. The upper branch of the curves applies to region β behind the shock, and the lower branch applies to region α behind the zero-thickness expansion wave associated with the shock of strength $p_{\beta o}/p_\infty$. In addition to the values determined from equation (18), there are shown values which would be obtained, if the fluid were assumed to be incompressible, by the integral method of reference 14 and the numerical solution to the Prandtl boundary-layer equations. (The results of ref. 15 are applicable to this numerical solution.) The agreement between both the curves of equation (18) and the referenced curves is very good. However, since the curve based on the Rayleigh limit gives a better approximation in region β, which will be shown to dominate the attenuation equations, the Rayleigh values of $F_1=0.718$ and $\delta^*/\theta=2.469$ shall be used for the remainder of this paper. Reference 17 also employed a normalized Rayleigh velocity distribution in the treatment of flow induced by shock waves.

For the turbulent case two analogous limiting processes are not available in order to determine the values of F_n. The turbulent boundary-layer theory is semiempirical and relies on experiments to supply constants for the resulting equations. Since no "Rayleigh-type" experiments have been performed, there is no limiting process $\frac{U_W}{U}\to\infty$ to apply for the turbulent case. There is, however, the semi-infinite flat-plate solution

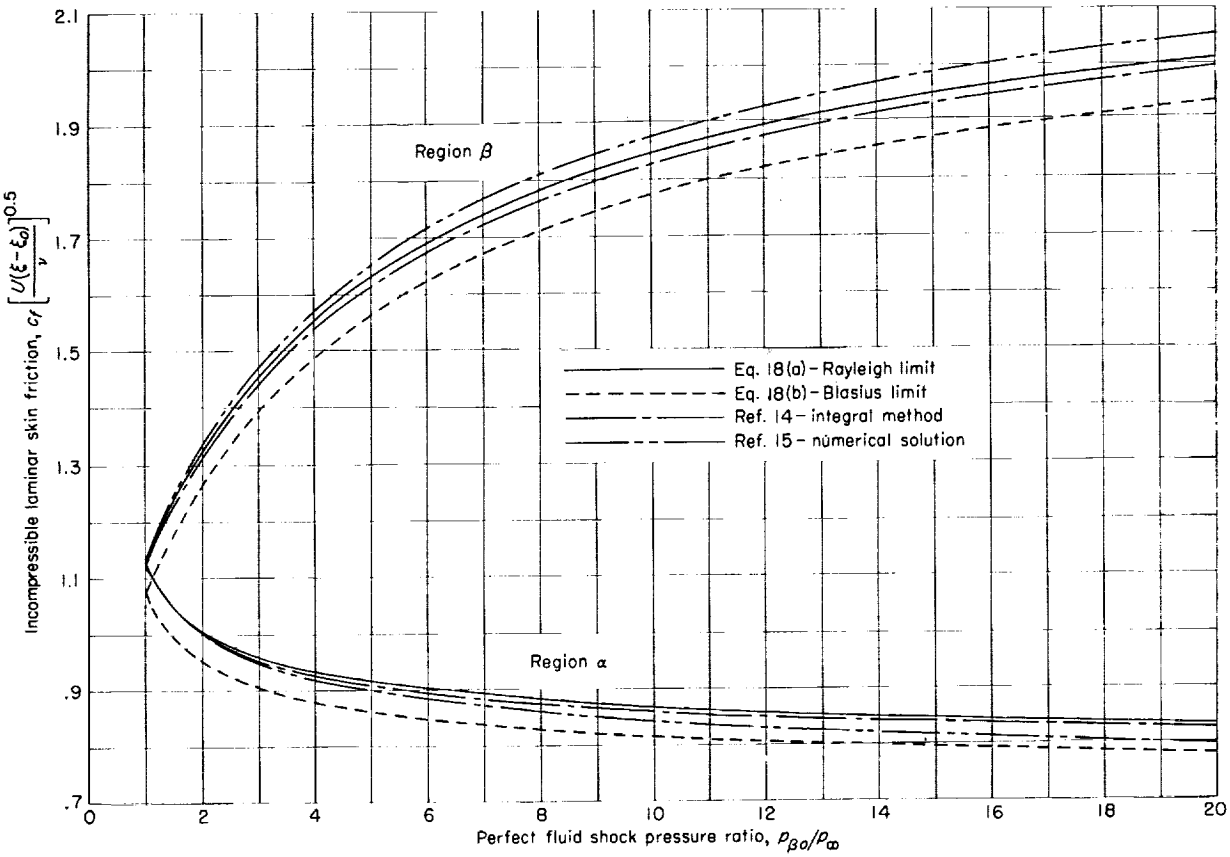

FIGURE 2.—Plot of incompressible local skin-friction coefficient for wave-induced flows having ratios of wave velocity to flow velocity corresponding to those in a shock tube of given shock pressure ratio. The expansion wave has been approximated by a negative shock. $\gamma=1.4$.

corresponding to the limit $\frac{U_W}{U}\to 0$. This solution (see refs. 1 and 19) assumes a velocity profile $\frac{u}{U}=\left(\frac{y}{\delta}\right)^{1/7}$ and results in a skin-friction coefficient expressed as

$$c_f(\xi)=0.0581\left[\frac{U(\xi-\xi_o)}{\nu}\right]^{-\frac{1}{5}} \tag{19}$$

The combination of equations (16) and (19) results in a value of $F_7=0.0581$.

For profiles of the family $\frac{u}{U}=\left(\frac{y}{\delta}\right)^{1/n}$ it may be shown that

$$\left.\begin{aligned}\frac{\theta}{\delta}&=\frac{n}{(n+1)(n+2)}\\ \frac{\delta^*}{\delta}&=\frac{1}{n+1}\\ \frac{\delta^*}{\theta}&=\frac{n+2}{n}\end{aligned}\right\} \tag{20}$$

Therefore, the expression for the one-seventh-power turbulent velocity profile skin-friction coefficient in the nonsteady incompressible flow becomes

$$c_f(\xi)=0.0581\left(1+\frac{2}{7}\frac{U_W}{U_W-U}\right)^{\frac{1}{5}}\left[\frac{U}{\nu}(\xi-\xi_o)\right]^{-\frac{1}{5}} \tag{21}$$

Since there was only a minor difference between the unsteady-flow values of c_f for laminar flow when based on the limiting cases of $\frac{U_W}{U}\to 0$ and $\frac{U_W}{U}\to\infty$, it is expected that the turbulent-flow agreement would be just as favorable if results were available for $\frac{U_W}{U}\to\infty$. Consequently, equation (21) is assumed to be a fairly close approximation to the correct answer. Equation (65) of reference 15 is very similar to equation (21) but was derived in a different way.

The skin-friction-coefficient relation of equation (19) corresponding to the one-seventh-power profile law is no longer valid at arbitrary large values of Reynolds number in incompressible steady flow. Instead a logarithmic law is often used. (See ref. 19.) However, since a power profile is easily handled by these methods, the skin friction on a semi-infinite plate for these large Reynolds numbers is found to be closely approximated by the relation

$$c_f=0.0186\left[\frac{U(\xi-\xi_o)}{\nu}\right]^{-\frac{1}{8}} \tag{22}$$

which is compatible with the relation $\frac{u}{U}=(y/\delta)^{1/13}$. If for consistency it is further assumed that δ^*/θ has the value 15/13 (the value for $n=13$), then the unsteady skin-friction coefficient would be given by

$$c_f(\xi)=0.0186\left(1+\frac{2}{13}\frac{U_W}{U_W-U}\right)^{\frac{1}{8}}\left[\frac{U(\xi-\xi_o)}{\nu}\right]^{-\frac{1}{8}} \tag{23}$$

No claim is advanced that a 1/13-power profile actually exists at these higher Reynolds numbers; it is only necessary for equation (22) to be valid for steady flow and the value of δ^*/θ to be 15/13.

It was shown in reference 14 that the skin friction in region α is correctly given by the method of characteristics using the boundary condition $\theta=0$ for $\xi=0$ at $x=-a_\epsilon t$ (that is, on the zero-thickness expansion wave) for that part of α where $x<Ut\theta/\delta^*$ and the boundary condition $\theta=0$ for $\xi=0$ at $x=U_st$ (that is, on the shock wave) for that part of α where $Ut\theta/\delta^*\leqq x\leqq Ut$. Sketch 1 shows a boundary-layer momentum characteristic. In order to determine the unsteady friction coefficient at point c in the region in question, $Ut\theta/\delta^*\leqq x\leqq Ut$, the boundary condition of $\theta=0$ on the shock wave (point a) is correct. In the analysis which follows, the boundary condition $\theta=0$ on the expansion wave (point b) is used instead. Friction coefficients are shown qualitatively in sketch 2. The solid curve represents the case with the boundary condition on the shock whereas the dashed curve represents the case with the boundary condition on the expansion wave. In the region in question it is seen that the differences are not serious. Because of the relatively small contribution of region α to attenuation as compared with the contribution of region β and also in the interest of simplicity, this error is neglected.

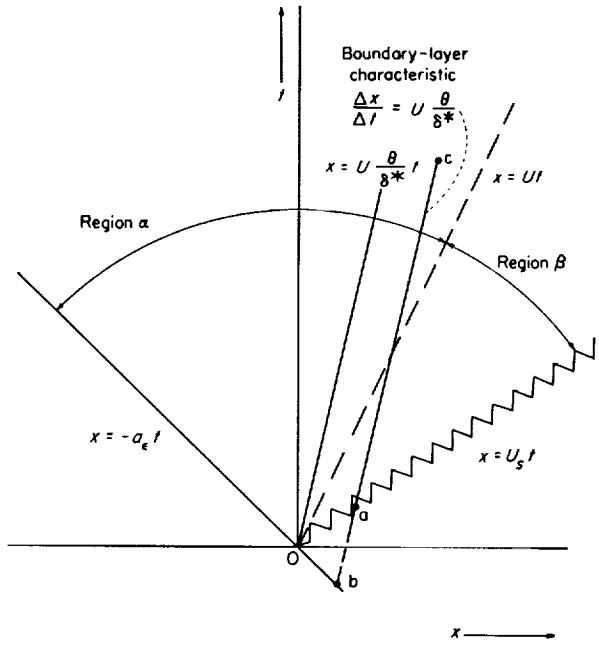

Sketch 1.

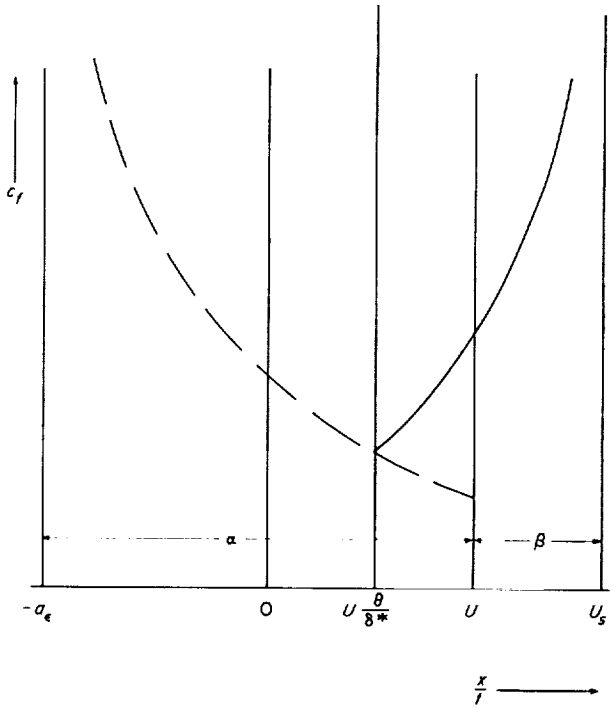

Sketch 2.

In order to handle the transitional flows which occur behind the waves in a shock tube, some approximation for c_f in the transition region must be employed. Any of a number of assumptions is possible in this region. However, in view of the many assumptions already present in the theory, the least complicating supposition will be employed in this case; namely, an instantaneous transition is assumed and the value of c_f in the turbulent region will be taken as the value which would be present had turbulent flow existed since the initiation of flow. In other words, at the transition point the local c_f changes discontinuously from the laminar to the turbulent value and the value $\xi_o=0$ then applies in both laminar and turbulent regions. This assumption was used in the logarithmic transitional curve for steady flow of reference 19. Figure 3 compares the integrated skin-friction coefficients of reference 19 with the curves obtained by the various power laws and the foregoing transitional assumption. The agreement appears to be very good.

A simple compressibility correction will be based on the intermediate temperature or T' semiempirical method. This correction, expounded in reference 20 for laminar boundary layers and in reference 21 for turbulent boundary layers, assumes that the incompressible skin-friction relations apply to compressible flow if the properties of the compressible flow are taken as some intermediate value between the wall and free-stream values. Thus, if the relation

$$c_f \equiv \frac{\tau_w}{\frac{1}{2}\rho U^2} = F_n\left(\frac{U}{\nu}\xi\right)^{-\frac{2}{n+3}} \tag{24}$$

applies to a steady incompressible flow, then

$$c_f' \equiv \frac{\tau_w}{\frac{1}{2}\rho' U^2} = F_n\left(\frac{U}{\nu'}\xi\right)^{-\frac{2}{n+3}} \tag{25}$$

will apply to a steady compressible flow for a certain choice of the primed state. The following values of the intermediate temperature T' are given (see refs. 20 and 21):

For laminar flow:

$$\frac{T'}{T} = 1 + 0.032M^2 + 0.58\left(\frac{T_w}{T} - 1\right) \tag{26a}$$

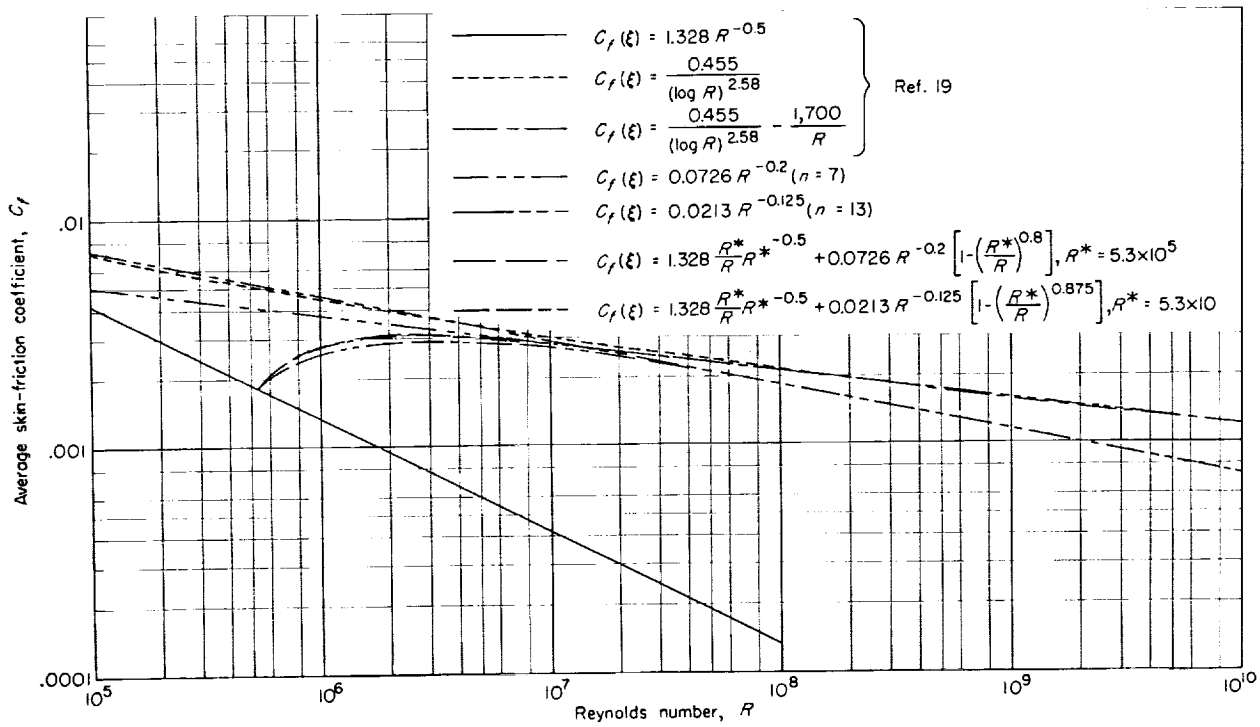

FIGURE 3.— Plot of average skin-friction coefficient against Reynolds number.

For turbulent flow:

$$\frac{T'}{T}=1+0.035M^2+0.45\left(\frac{T_w}{T}-1\right) \tag{26b}$$

It may be shown that for an arbitrary reference state, which may be either wall or free stream, equation (25) may be put in the form

$$c_f\equiv\frac{\tau_w}{\frac{1}{2}\rho U^2}=F_n\left(\frac{U}{\nu}\xi\right)^{-\frac{2}{n+3}}\left(\frac{T}{T'}\right)^{\frac{n+1}{n+3}}\left(\frac{\mu'}{\mu}\right)^{\frac{2}{n+3}} \tag{27a}$$

$$c_f=F_n\left(\frac{U}{\nu}\xi\right)^{-\frac{2}{n+3}}\Omega_n \tag{27b}$$

If a temperature-viscosity relation of the form

$$\frac{\mu}{\mu'}=\left(\frac{T}{T'}\right)^{\omega}$$

is assumed to apply, then the steady-flow compressibility correction Ω_n becomes

$$\Omega_n=\left(\frac{T}{T'}\right)^{\frac{n+1-2\omega}{n+3}} \tag{28}$$

It is assumed that this T' method is also applicable as a compressibility correction for the unsteady-flow skin-friction coefficients. Compressibility corrections in hot and cold gas Ω_n are plotted against shock pressure ratio in figure 4 for an air-air shock tube. The value $\omega=0.8$ has been used to compute these curves.

The results of this section may be summarized by the following expressions for skin-friction coefficient:

$$\left.\begin{aligned}(c_f)_{n=1}&=0.718\left(1+1.469\frac{U_w}{U_w-U}\right)^{\frac{1}{2}}\left(\frac{U}{\nu}\xi\right)^{-\frac{1}{2}}\Omega_1\\(c_f)_{n=7}&=0.0581\left(1+\frac{2}{7}\frac{U_w}{U_w-U}\right)^{\frac{1}{5}}\left(\frac{U}{\nu}\xi\right)^{-\frac{1}{5}}\Omega_7\\(c_f)_{n=13}&=0.0186\left(1+\frac{2}{13}\frac{U_w}{U_w-U}\right)^{\frac{1}{8}}\left(\frac{U}{\nu}\xi\right)^{-\frac{1}{8}}\Omega_{13}\end{aligned}\right\} \tag{29}$$

where

$$\Omega_n=\left(\frac{T}{T'}\right)^{\frac{n+1}{n+3}}\left(\frac{\mu'}{\mu}\right)^{\frac{2}{n+3}}$$

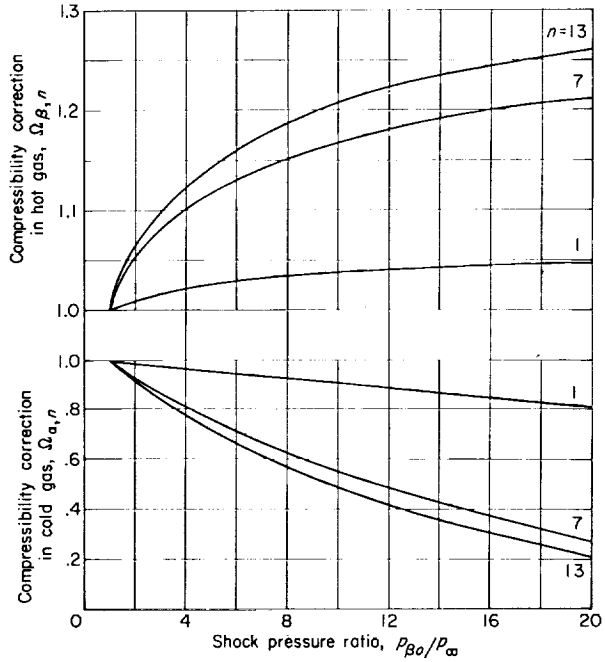

FIGURE 4.—Compressibility corrections as a function of shock pressure ratio for shock-tube flow. $\gamma=1.4$; $\omega=0.8$.

EVALUATION OF THE LINEARIZED ATTENUATION EXPRESSIONS

The basic linearized attenuation expressions derived in reference 1 are summarized in appendix A. The following expressions result from the first identity and subsequent substitution and manipulation of the pertinent equations from the appendix:

$$\frac{P_{vs}-P_{\beta o}}{a_\epsilon}=\frac{P_{vs}-P_f}{a_\epsilon}+\frac{P_f-P_c}{a_\epsilon}+\frac{P_c-P_b}{a_\epsilon}+\frac{P_b-P_{\beta o}}{a_\epsilon} \tag{30}$$

$$\frac{P_{vs}-P_{\beta o}}{a_\epsilon}=\frac{1}{D}\int_0^{\xi_d}\left[-\phi_{P,\beta}\frac{\sigma M_s-M_\beta}{\sigma M_s-M_\beta-1}+\phi_{Q,\beta}\frac{\sigma M_s-M_\beta}{\sigma M_s-M_\beta+1}\frac{P_{\beta o}-P_{\alpha o}}{P_{\beta o}+Q_{\beta o}}+\frac{\gamma-1}{\gamma}\frac{\frac{a_{\beta o}}{a_{\alpha o}}}{\left(\frac{a_{\beta o}}{a_{\alpha o}}\right)^2-1}\frac{P_{\beta o}-P_{\alpha o}}{a_\epsilon}\phi_{s,\beta}\right]c_{f,\beta}(\xi)d\xi$$

$$+\frac{1}{D}\int_0^{\xi_d}\left[\phi_{P,\alpha}\frac{M_\alpha+\eta}{M_\alpha+\eta+1}\frac{P_{\beta o}+Q_{\beta o}}{P_{\alpha o}+Q_{\beta o}}-\frac{\gamma-1}{\gamma}\frac{\frac{a_{\beta o}}{a_{\alpha o}}}{\left(\frac{a_{\beta o}}{a_{\alpha o}}\right)^2-1}\frac{P_{\beta o}-P_{\alpha o}}{a_\epsilon}\phi_{s,\alpha}\right]c_{f,\alpha}(\xi)d\xi \tag{31a}$$

$$\frac{P_{vs}-P_{\beta o}}{a_\epsilon}=\frac{1}{D}\int_0^{\xi_d}\Gamma_\beta c_{f,\beta}d\xi+\frac{1}{D}\int_0^{\xi_d}\Gamma_\alpha c_{f,\alpha}d\xi \tag{31b}$$

Since

$$\frac{p_{vs}-p_{\beta o}}{p_{\beta o}}=\frac{\gamma}{2}\frac{a_\epsilon}{a_{\beta o}}\frac{P_{vs}-P_{\beta o}}{a_\epsilon} \tag{32}$$

(see ref. 1) the following relation results

$$\frac{p_{vs}-p_{\beta o}}{p_{\beta o}}\left(\frac{\gamma}{2}\frac{a_\epsilon}{a_{\beta o}}\frac{1}{D}\right)^{-1}=\Gamma_{\beta,m}\int_0^{\kappa\xi_\beta^*}c_{f,\beta,m}d\xi+\Gamma_{\beta,n}\int_{\kappa\xi_\beta^*}^{\xi_d}c_{f,\beta,n}d\xi+\Gamma_{\alpha,m}\int_0^{\kappa\xi_\alpha^*}c_{f,\alpha,m}d\xi+\Gamma_{\alpha,n}\int_{\kappa\xi_\alpha^*}^{\xi_d}c_{f,\alpha,n}d\xi \tag{33}$$

in which the subscript m applies in the laminar range $0\leqq\xi_{\alpha,\beta}\leqq\xi_{\alpha,\beta}^*$ and the subscript n applies in the turbulent range $\xi_{\alpha,\beta}^*\leqq\xi_{\alpha,\beta}\leqq\xi_d$. The value of κ is defined as ξ_d/ξ^* for $\xi^*\geqq\xi_d$ and as 1 for $\xi^*\leqq\xi_d$.

The total linearized attenuation is thus made up of the sum of the effects of regions α and β. This relation may be expressed mathematically as

$$\frac{p_{vs}-p_{\beta o}}{p_{\beta o}}=\left(\frac{p_{vs}-p_{\beta o}}{p_{\beta o}}\right)_\alpha+\left(\frac{p_{vs}-p_{\beta o}}{p_{\beta o}}\right)_\beta \tag{34}$$

where

$$\left(\frac{p_{vs}-p_{\beta o}}{p_{\beta o}}\right)_\alpha=\frac{\gamma}{2}\frac{a_\epsilon}{a_{\beta o}}\frac{1}{D}\left(\Gamma_{\alpha,m}\int_0^{\kappa\xi_\alpha^*}c_{f,\alpha,m}d\xi+\Gamma_{\alpha,n}\int_{\kappa\xi_\alpha^*}^{\xi_d}c_{f,\alpha,n}d\xi\right) \tag{35a}$$

$$\left(\frac{p_{vs}-p_{\beta o}}{p_{\beta o}}\right)_\beta=\frac{\gamma}{2}\frac{a_\epsilon}{a_{\beta o}}\frac{1}{D}\left(\Gamma_{\beta,m}\int_0^{\kappa\xi_\beta^*}c_{f,\beta,m}d\xi+\Gamma_{\beta,n}\int_{\kappa\xi_\beta^*}^{\xi_d}c_{f,\beta,n}d\xi\right) \tag{35b}$$

Now, with c_f expressed in the form

$$c_{f,n}(\xi)=F_nE_n^{\frac{2}{n+3}}\left(\frac{U}{\nu}\xi\right)^{-\frac{2}{n+3}}\left(\frac{T}{T'}\right)^{\frac{n+1-2\omega}{n+3}} \tag{36a}$$

or

$$c_{f,n}(\xi)=G_n\Omega_n\left(\frac{U}{\nu}\xi\right)^{-\frac{2}{n+3}} \tag{36b}$$

integration of equations (35) results in the following equations. (The subscript x designates either

region α or region β.)

$$\left(\frac{p_{vs}-p_{\beta o}}{p_{\beta o}}\right)_{\chi,m,n}=\frac{\gamma}{2}\frac{a_\epsilon}{a_{\beta o}}\frac{1}{D}\left\{\Gamma_m\frac{m+3}{m+1}G_m\Omega_m\left(\frac{U}{\nu}\right)^{-\frac{2}{m+3}}(\kappa\xi^*)^{\frac{m+1}{m+3}}+\Gamma_n\frac{n+3}{n+1}G_n\Omega_n\left(\frac{U}{\nu}\right)^{-\frac{2}{n+3}}\left[(\xi_d)^{\frac{n+1}{n+3}}-(\kappa\xi^*)^{\frac{n+1}{n+3}}\right]\right\}_\chi$$

$$=\frac{\gamma}{2}\frac{a_\epsilon}{a_{\beta o}}\frac{l}{D}\left\{\Gamma_m G_m\Omega_m\frac{m+3}{m+1}\left(\frac{U}{a_\infty}\frac{\nu_\infty}{\nu}\right)^{-\frac{2}{m+3}}\left(\frac{\xi_d}{l}\right)^{\frac{m+1}{m+3}}\left(\frac{\kappa\xi^*}{\xi_d}\right)^{\frac{m+1}{m+3}}\left(\frac{a_\infty l}{\nu_\infty}\right)^{-\frac{2}{m+3}}\right.$$

$$\left.+\Gamma_n G_n\Omega_n\frac{n+3}{n+1}\left(\frac{U}{a_\infty}\frac{\nu_\infty}{\nu}\right)^{-\frac{2}{n+3}}\left(\frac{\xi}{l}\right)^{\frac{n+1}{n+3}}\left[1-\left(\frac{\kappa\xi^*}{\xi_d}\right)^{\frac{n+1}{n+3}}\right]\left(\frac{a_\infty l}{\nu_\infty}\right)^{-\frac{2}{n+3}}\right\}_\chi \tag{37}$$

Rearrangement of terms of equation (37) produces

$$\left(\frac{p_{vs}-p_{\beta o}}{p_\infty}\right)_{\chi,m,n}\left[\frac{l}{D}\left(\frac{a_\infty l}{\nu_\infty}\right)^{-\frac{2}{n+3}}\right]^{-1}=\frac{\gamma}{2}\frac{a_\epsilon}{a_{\beta o}}\frac{p_{\beta o}}{p_\infty}\left\{\Gamma_m G_m\Omega_m\frac{m+3}{m+1}\left(\frac{U}{a_\infty}\frac{\nu_\infty}{\nu}\right)^{-\frac{2}{m+3}}\left(\frac{\xi_d}{l}\right)^{\frac{m+1}{m+3}}\left(\frac{\kappa\xi^*}{\xi_d}\right)^{\frac{m+1}{m+3}}\left(\frac{a_\infty l}{\nu_\infty}\right)^{\frac{2(m-n)}{(m+3)(n+3)}}\right.$$

$$\left.+\Gamma_n G_n\Omega_n\frac{n+3}{n+1}\left(\frac{U}{a_\infty}\frac{\nu_\infty}{\nu}\right)^{-\frac{2}{n+3}}\left(\frac{\xi_d}{l}\right)^{\frac{n+1}{n+3}}\left[1-\left(\frac{\kappa\xi^*}{\xi_d}\right)^{\frac{n+1}{n+3}}\right]\right\}_\chi \tag{38}$$

$$\left(\frac{p_{vs}-p_{\beta o}}{p_\infty}\right)_{\chi,m,n}\left[\left(\frac{l}{D}\right)^{\frac{n+1}{n+3}}\left(\frac{a_\infty D}{\nu_\infty}\right)^{-\frac{2}{n+3}}\right]^{-1}=g_{\chi m}\Omega_{\chi m}\left(\frac{\kappa\xi^*}{\xi_d}\right)^{\frac{m+1}{m+3}}\left[\left(\frac{l}{D}\right)\left(\frac{a_\infty D}{\nu_\infty}\right)\right]^{\frac{2(m-n)}{(m+3)(n+3)}}+g_{\chi n}\Omega_{\chi n}\left[1-\left(\frac{\kappa\xi^*}{\xi_d}\right)^{\frac{n+1}{n+3}}\right] \tag{39a}$$

where

$$\left.\begin{aligned}g_{\chi m}&=f_{\chi m}\left(\frac{U_\chi}{a_\infty}\frac{\nu_\infty}{\nu_\chi}\right)^{-\frac{2}{m+3}}\\ f_{\chi m}&=\frac{\gamma}{2}\frac{a_\epsilon}{a_{\beta o}}\frac{p_{\beta o}}{p_\infty}\frac{m+3}{m+1}\Gamma_{\chi m}G_{\chi m}\left(\frac{\xi_d}{l}\right)^{\frac{m+1}{m+3}}\end{aligned}\right\} \tag{39b}$$

Note that $f_{\chi m}$ is a function only of the shock pressure ratio $p_{\beta o}/p_\infty$ and the value of m for any region χ. The term $g_{\chi m}$ requires in addition a temperature-viscosity relation which may be either an exponential type or some other form, such as the Sutherland equation.

For the case of no transition when the flow is either completely laminar or completely turbulent, equation (39a) reduces to

$$\frac{p_{vs}-p_{\beta o}}{p_\infty}=\left(\frac{l}{D}\right)^{\frac{m+1}{m+3}}\left(\frac{a_\infty D}{\nu_\infty}\right)^{-\frac{2}{m+3}}g_{\chi m}\Omega_{\chi m}$$

or

$$\frac{p_{vs}-p_{\beta o}}{p_\infty}=\left(\frac{l}{D}\right)^{\frac{n+1}{n+3}}\left(\frac{a_\infty D}{\nu_\infty}\right)^{-\frac{2}{n+3}}g_{\chi n}\Omega_{\chi n} \tag{40}$$

The attenuation in this case for a given initial value of $p_{\beta o}/p_\infty$ is obviously dependent only on the two parameters expressed as hydraulic diameters of shock-wave travel l/D and shock-tube Reynolds number $a_\infty D/\nu_\infty$.

For the case with transition three parameters are required to describe the phenomenon at a given initial value of $p_{\beta o}/p_\infty$, the third parameter is the transition Reynolds number R^* and enters into

the analysis in the following manner:

$$\frac{\xi^*}{\xi_d}=\frac{U\xi^*}{\nu}\frac{\nu_\infty}{a_\infty D}\frac{D}{l}\frac{a_\infty}{U}\frac{\nu}{\nu_\infty}\frac{l}{\xi_d} \tag{41}$$

When equation (41) is substituted into equation (39a), the linear transitional attenuation relation becomes:

$$\left(\frac{p_{ts}-p_{\beta o}}{p_\infty}\right)_{\chi,m,n}\left[\left(\frac{l}{D}\right)^{\frac{n+1}{n+3}}\left(\frac{a_\infty D}{\nu_\infty}\right)^{-\frac{2}{n+3}}\right]^{-1}=g_{\chi m}\Omega_{\chi m}\left(\frac{a_\infty}{U}\frac{\nu}{\nu_\infty}\frac{l}{\xi_d}\right)^{\frac{m+1}{m+3}}(R^*)^{\frac{m+1}{m+3}}\left(\frac{l}{D}\frac{a_\infty D}{\nu_\infty}\right)^{-\frac{n+1}{n+3}}(\kappa)^{\frac{m+1}{m+3}}$$
$$+g_{\chi n}\Omega_{\chi n}\left[1-\left(\frac{a_\infty}{U}\frac{\nu}{\nu_\infty}\frac{l}{\xi_d}\right)^{\frac{n+1}{n+3}}(R^*)^{\frac{n+1}{n+3}}\left(\frac{l}{D}\frac{a_\infty D}{\nu_\infty}\right)^{-\frac{n+1}{n+3}}(\kappa)^{\frac{n+1}{n+3}}\right] \tag{42}$$

where the term $\frac{a_\infty}{U}\frac{\nu}{\nu_\infty}\frac{l}{\xi_d}$ is a function of $p_{\beta o}/p_\infty$. Thus, at a given value of $p_{\beta o}/p_\infty$ the linearized attenuation is a function only of l/D, $a_\infty D/\nu_\infty$, and R^*.

The attenuation functions $g_{\chi m}$, the compressibility corrections $\Omega_{\chi m}$ and their products are presented in table I for shock pressure ratios from 1.0 to 20.0 and for m equal to 1, 7, and 13. It may be seen by inspection of equation (40) that, for given shock tube l/D, Reynolds number $a_\infty D/\nu_\infty$, and no transition, the attenuation contribution of the region χ is directly proportional to the product $(\Omega g)_{\chi m}$. In order to demonstrate graphically the behavior of these compressible attenuation functions, they have been plotted in figures 5(a) and 5(b). The magnitude of the contribution of region β to attenuation increases monatomically with increasing pressure ratio, is always negative in sign, and thus tends to increase attenuation. On the other hand, for low pressure ratios the contribution of region α tends to increase

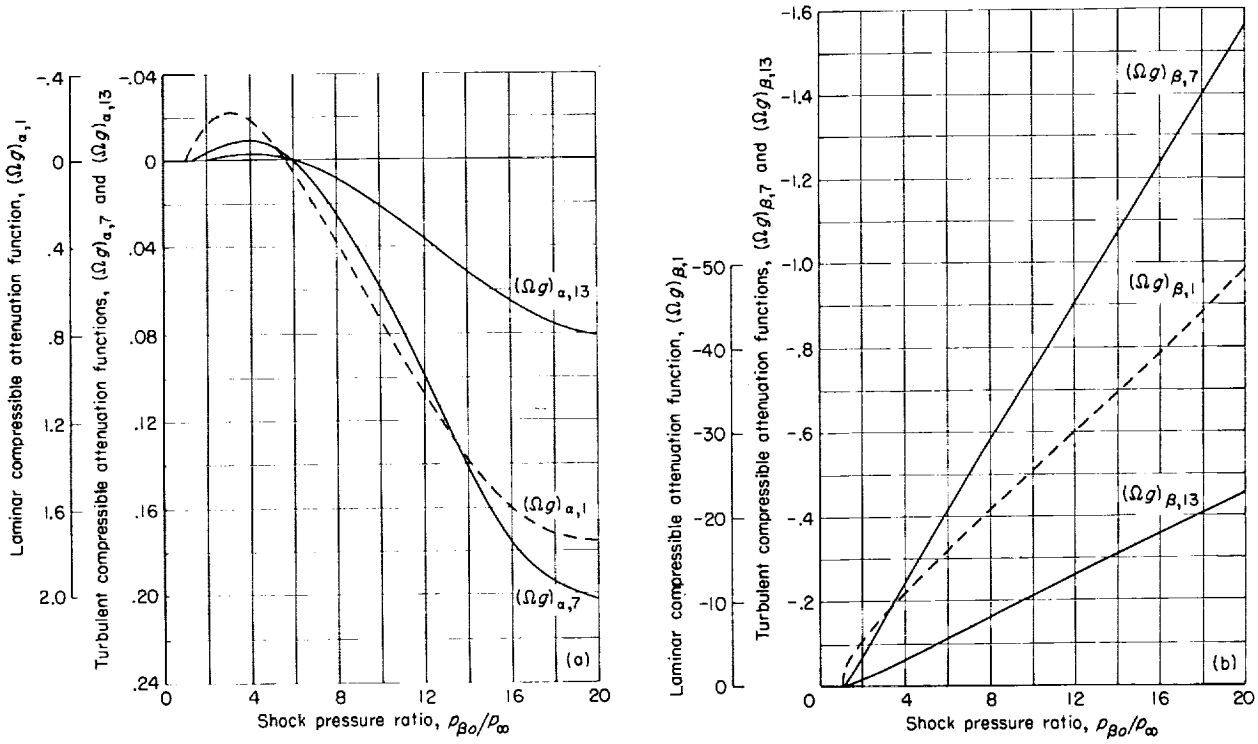

(a) Region α.

(b) Region β.

FIGURE 5. Variation of compressible linear attenuation functions with shock pressure ratio. $\gamma=1.4$; $\omega=0.8$.

attenuation; above a shock pressure ratio of about 5.9, the trend is reversed and region α contributes compression waves that tend to decrease attenuation. This reversal is discussed more fully in reference 1.

When no transition is considered, the attenuation function for the entire flow field is found by adding the contributions of regions α and β. For the cases where the profile exponent m is the same in both regions, the total compressible attenuation function has been computed and is shown in table I and in figure 6 for values of m of 1, 7, and 13. This function is given as

$$\frac{p_{vs}-p_{\beta_0}}{p_\infty}\left[\left(\frac{l}{D}\right)^{\frac{m+1}{m+3}}\left(\frac{\nu_\infty}{a_\infty D}\right)^{\frac{2}{m+3}}\right]^{-1}=(\Omega g)_{\alpha,m}+(\Omega g)_{\beta,m}$$

The results of using the methods of references 1 and 2 are also shown in figures 6(a) and 6(b) for values of m of 1 and 7, respectively.

For the laminar case the curve in figure 6(a) representing the method of reference 1 falls far below that of the present report, primarily because of the importance of the neglected unsteadiness effects as discussed in the introduction. The results of reference 2 are also below that of the present report (approximately 25 percent for

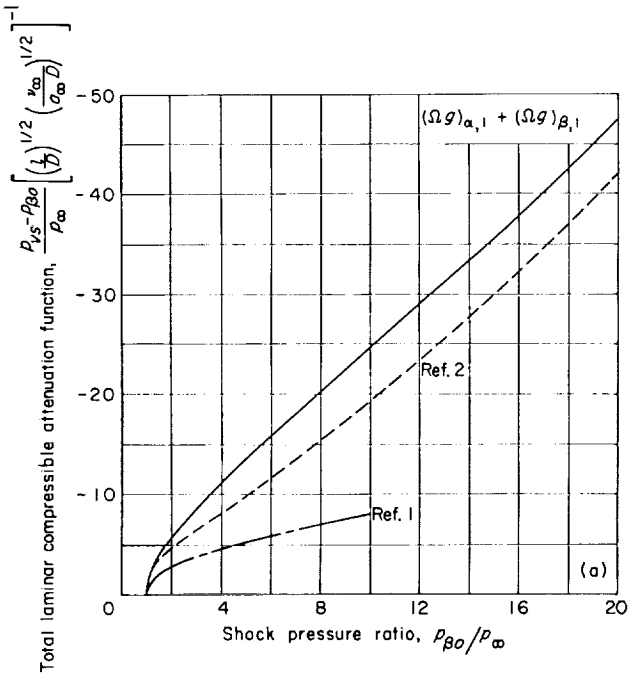

(a) Laminar flow; $m=1$.

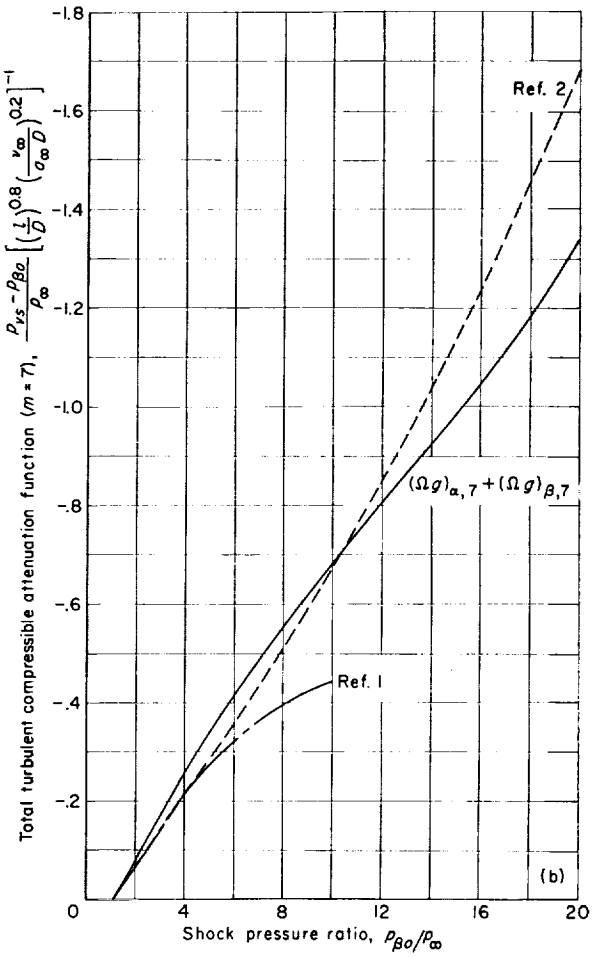

(b) Turbulent flow; $m=7$.

FIGURE 6.—Continued.

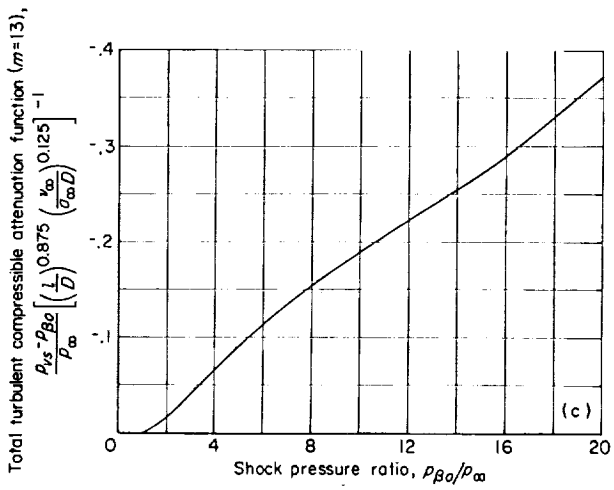

(c) Turbulent flow; $m=13$.

FIGURE 6.—Concluded.

FIGURE 6.—Plot of total compressible linear attenuation functions against shock pressure ratio. $\gamma=1.4$; $\omega=0.8$.

shock pressure ratios from 4 to 10) and show better agreement at higher pressure ratios (only 10 percent below for a shock pressure ratio of 20).

Agreement between the methods of references 1 and 2 and the present method is better for the turbulent case ($m=7$; fig. 6(b)). The neglect of unsteadiness has a smaller effect upon the results of reference 1, although the effects of compressibility still give significant deviations at shock pressure ratios near 10. The present results and the results of reference 2 are in agreement within less than 15 percent for shock pressure ratios up to 10 and then diverge to a 20-percent variation at a shock pressure ratio of 20.

Figures 5 and 6 show that the cold gas contributes only a small part of the total attenuation for $p_{s_0}/p_\infty<20$. At $p_{s_0}/p_\infty=20$ the relative α contribution is larger than that for $p_{s_0}/p_\infty<20$; however, it is only about 4 percent, 15 percent, and 25 percent of the total for $m=1$, 7, and 13, respectively.

EVALUATION OF NONLINEAR ATTENUATION EXPRESSIONS

The expressions derived previously are based on a linearized or small perturbation analysis. However, for many conditions encountered in the shock tube, the attenuation is no longer small. In order to maximize the total available experimental testing time, most experimental work is done at values of l nearly equal to the total length of the low-pressure side of the shock tube. At these large values of l the shock strength often has decayed markedly from its value for small l. Consequently, relations for the attenuation under these conditions would be very desirable.

An approximate method to obtain the attenuation for the cases where the small perturbation analysis is invalid will be described. First, consider parameters $\hat{P}$ and $\hat{Q}$ which are related to P and Q by

$$\left.\begin{aligned}\hat{P}&=P-\frac{a}{\gamma}\frac{S}{R}\\ \hat{Q}&=Q-\frac{a}{\gamma}\frac{S}{R}\end{aligned}\right\} \tag{43}$$

(The parameters $\hat{P}$ and $\hat{Q}$ of this report are identical to the parameters P' and Q' of ref. 1.) When equation (43) is substituted into equation (60) of reference 1, the following equations result:

$$\begin{pmatrix}\frac{1}{a_\epsilon}\frac{\delta\hat{P}}{\delta t}\\ \frac{1}{a_\epsilon}\frac{\delta\hat{Q}}{\delta t}\end{pmatrix}=\frac{1}{\gamma}\frac{a}{a_\epsilon}\frac{1}{p}\frac{\delta p}{\delta t}\pm\frac{1}{a_\epsilon}\frac{\delta U}{\delta t} \tag{44a}$$

$$\begin{pmatrix}\frac{1}{a_\epsilon}\frac{\delta\hat{P}}{\delta t}\\ \frac{1}{a_\epsilon}\frac{\delta\hat{Q}}{\delta t}\end{pmatrix}=\frac{2}{D}\frac{a}{a_\epsilon}Uc_f\left\{[(\gamma-1)M\mp1]M+N_{Pr}^{-2/3}\frac{T_w-T_{aw}}{T}\right\} \tag{44b}$$

$$\begin{pmatrix}\frac{1}{a_\epsilon}\frac{\delta\hat{P}}{\delta t}\\ \frac{1}{a_\epsilon}\frac{\delta\hat{Q}}{\delta t}\end{pmatrix}=\frac{1}{D}Uc_f\begin{pmatrix}\phi_{\hat{P}}\\ \phi_{\hat{Q}}\end{pmatrix} \tag{44c}$$

As discussed in reference 1, the changes in $\hat{P}$ and $\hat{Q}$ are evident in changes by wave motion of velocity and pressure but do not indicate the various changes in entropy. For example, if equation (44a) is solved for $\delta p/p$,

$$\frac{\delta p}{p}=\frac{\gamma}{2}\frac{a_\epsilon}{a}\left(\frac{\delta\hat{P}}{a_\epsilon}+\frac{\delta\hat{Q}}{a_\epsilon}\right) \tag{45}$$

The value of $\hat{P}$ is associated with waves moving with the flow at a velocity of $u+a$ whereas $\hat{Q}$ is associated with waves of the opposite family moving at a velocity $u-a$. Now, for the linear attenuation theory it is assumed that reflections at the shock wave and the deviation in entropy rise across the shock wave may be ignored; that is, $\hat{Q}_{vs}=Q_{vs}=Q_{s_0}$ or $\delta\hat{Q}_{vs}=\delta Q_{vs}=0$. Consequently, an alternate form for the attenuation expression is

$$\frac{\delta p}{p}=\frac{p_{vs}-p_{s_0}}{p_{s_0}}=\frac{\gamma}{2}\frac{a_\epsilon}{a}\left[\left(\frac{\delta\hat{P}}{a_\epsilon}\right)_\alpha+\left(\frac{\delta\hat{P}}{a_\epsilon}\right)_{reflection}+\left(\frac{\delta\hat{P}}{a_\epsilon}\right)_\beta\right] \tag{46}$$

where the three terms on the right-hand side of the equation represent, respectively, the contributions of region α, of the $\hat{Q}$ wave generated in region β and reflected at the entropy discontinuity, and of the $\hat{P}$ wave generated in region β.

Consider now the last term only. The incremental change $\delta\hat{P}$ along the characteristic is then

$$\left(\frac{\delta\hat{P}}{a_\epsilon}\right)_\beta \equiv \int_{t_f}^{t_r} \frac{1}{a_\epsilon}\frac{\delta\hat{P}}{\delta t}\,\delta t = \frac{1}{D}\int_{t_f}^{t_r} U c_f \phi_{\hat{P},\beta}\,\delta t \qquad (47)$$

A change of variable may be made (eq. (21) of ref. 1) to ξ since

$$U\delta t = \frac{\sigma M_s - M_\beta}{\sigma M_s - M_\beta - 1}\,d\xi$$

$$\left(\frac{\delta\hat{P}}{a_\epsilon}\right)_\beta = \frac{1}{D}\int_{\xi(t_f)}^{\xi(t_r)} \frac{\sigma M_s - M_\beta}{\sigma M_s - M_\beta - 1}\, c_f \phi_{\hat{P},\beta}\,d\xi$$

$$\left(\frac{\delta\hat{P}}{a_\epsilon}\right)_\beta = \frac{1}{D}\int_0^{\xi_d} -\frac{\sigma M_s - M_\beta}{\sigma M_s - M_\beta - 1}\,\phi_{\hat{P},\beta} c_{f,\beta}(\xi)\,d\xi \qquad (48a)$$

$$\left(\frac{\delta\hat{P}}{a_\epsilon}\right)_\beta = \frac{1}{D}\int_0^{\xi_d} \left[-\frac{\sigma M_s - M_\beta}{\sigma M_s - M_\beta - 1}\left(\frac{\phi_{\hat{P},\beta}}{\Gamma_\beta}\right)\right]\Gamma_\beta c_{f,\beta}\,d\xi \qquad (48b)$$

Substituting equation (45) into equation (48) yields:

$$\left(\frac{p_{rs}-p_{\beta o}}{p_{\beta o}}\right)_{\beta,\hat{P}} = \left(\frac{\delta p}{p}\right)_{\beta,\hat{P}} = \frac{\gamma}{2}\frac{a_\epsilon}{a}\frac{1}{D}\int_0^{\xi_d} K(\xi)\Gamma_\beta c_{f,\beta}\,d\xi \qquad (49)$$

In equation (49), the left-hand side represents the pressure perturbation at the shock wave due to the wave generation only along the forward running (slope of $u+a$) characteristic. For a complete linearized treatment K and Γ_β may be taken outside the integral and equation (35b) may be employed to obtain:

$$\left(\frac{\delta p}{p}\right)_{\beta,\hat{P}} = \frac{\gamma}{2}\frac{a_\epsilon}{a}\frac{1}{D}K\Gamma_\beta\int_0^{\xi_d} c_{f,\beta}\,d\xi$$

$$= K\left(\frac{p_{rs}-p_{\beta o}}{p_{\beta o}}\right)_\beta \equiv \left(\frac{\delta\hat{p}}{p}\right)_\beta \qquad (50)$$

Thus, K is the ratio of the contribution of the waves generated along the forward running characteristics to the total waves generated in region β. The remaining portion of the attenuation contribution of β results from $\hat{Q}$ waves reflected at the entropy discontinuity and will be designated by $\left(\frac{\delta p}{p}\right)_{\beta,\hat{Q}+s}$ which is equal to

$$\left(\frac{\delta p}{p}\right)_{\beta,\hat{Q}+s} = (1-K)\left(\frac{p_{rs}-p_{\beta o}}{p_{\beta o}}\right)_\beta \qquad (51)$$

The value of K is plotted against shock pressure ratio in figure 7. The fact that K does not depart significantly from 1.0 means physically that the principal contribution to attenuation in region β arises from the $\hat{P}$ waves. Since figures 5 and 6 have shown region β to have a much larger effect on attenuation in general than region α, it is obvious that the theoretical dominating factors for attenuation are the $\hat{P}$ waves of region β. This conclusion has been discussed previously in references 1 and 2.

Since the $\hat{P}$ waves of region β dominate the linearized attenuation solution, it is next assumed

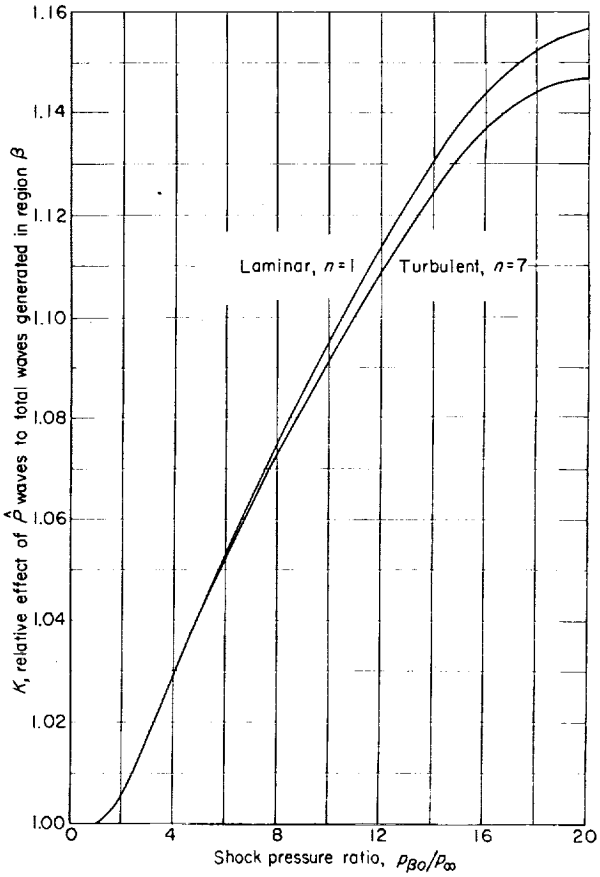

FIGURE 7. Ratio of linear attenuation effects generated along forward running characteristic to total attenuation effects of region β as a function of shock pressure ratio.

that a correction for the linearized solution may be found by operating only on the $\hat{P}$ waves in region β. Thus $\hat{P}$ waves generated in region α and transmitted at the entropy discontinuity as well as the $\hat{Q}$ waves generated in region β and reflected at the entropy discontinuity will retain their original linear or small perturbation values even though the attenuation is no longer small. It is further assumed that region β may be subdivided into a number of smaller regions in each of which the linear attenuation relations for $\hat{P}$ are valid. This treatment is illustrated in figure 8. The arbitrary interval Δl determines the x-wise extent along the shock wave of each of the regions designated Ⓘ, Ⓘ, ... Each of these regions is bounded by the shock wave and two fluid particle paths where each fluid particle velocity is equal, respectively, to that generated by the shock wave at the beginning of each new interval. The inviscid flow inside each of these regions is considered to be constant; and, consequently, there is a small discontinuity in the inviscid flow across the particle-path boundaries assumed in the model. These discontinuities can not, of course, exist in the actual physical flow which requires a continuous variation throughout all the regions as well as reflections from the shock wave. The errors introduced by the assumption of constant quantities in each region are not considered to be large and should be of approximately the same order as those found in the familiar steady-flow graphical characteristic solutions of finite mesh size.

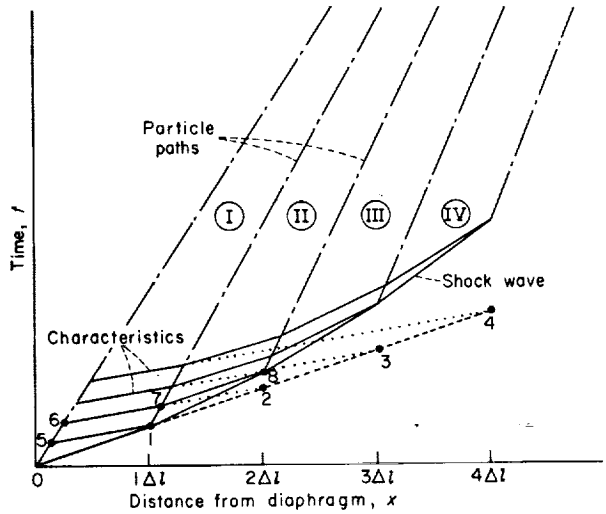

FIGURE 8.—General wave diagram for nonlinear analysis in region β. The short-dashed line is an extrapolation of the shock-wave path and the dotted lines are extrapolations of the characteristics.

In order to simplify the computational procedure, it is assumed that for a given region the slope $\delta x/\delta t$ of the $\hat{P}$ characteristic and of the shock wave are constant both inside and outside of that region. Thus, in figure 8, when the $\hat{P}$ contribution of region Ⓘ to attenuation between Δl and $2\Delta l$ is computed, the assumption is made that the characteristic $\overline{6,7}$ and the shock path $\overline{0,1}$ may be extended to intersect at point 2. (Numbers refer to points in fig. 8.) The corresponding correct regional characteristic line and shock paths are $\overline{6,7,8}$ and $\overline{0,1,8}$ which are shown in this illustration as intersecting also at the same value of x as 2. This intersection at the same value of x is only an idealization and is not the true physical picture in general. However, since the attenuation effect (generation of $\hat{P}$ waves) falls off rapidly with distance behind the shock (similar to the fall off in local skin friction with distance back of a sharp leading edge in steady flow), the contribution to attenuation in the interval from Δl to $2\Delta l$ due to generation along $\overline{6,7}$ is much less than that due to generation along $\overline{7,8}$; thus, small errors in the location of $\overline{6,7}$ will result in very small errors in the attenuation at $2\Delta l$. This assumption for establishing the intersection points of the characteristics and the shock wave downstream from a region Ⓝ without knowledge of the downstream shock-wave attenuation permits the easy computation of the influence of region Ⓝ for all downstream shock locations.

When the regional approach described above is applied, the attenuation for the first interval Δl is identical to the complete linear approach. Thereafter, however, the various second-order effects are felt. The effect of region Ⓘ on attenuation of the shock during the interval from Δl to $2\Delta l$ differs from its effect in the basic linear theory because of the convergence of the particle paths since $U_{\text{II}}<U_{\text{I}}$. This may be shown as follows. From equation (48),

$$\left(\frac{\delta\hat{P}}{a_\epsilon}\right)_{\text{I}}\Big|_6^7=\frac{1}{D}\int_{\xi_6}^{\xi_7}\left(\frac{\sigma M_s-M_\beta}{\sigma M_s-M_\beta-1}\right)_{\text{I}} c_f\phi\hat{P}_{,1}\,d\xi \quad (52)$$

The numbers refer to the points on figure 9(a). In this figure the lines $\overline{5,1}$, $\overline{10,11}$, and $\overline{6,7,2}$ are drawn with slope $(U+a)_{\text{I}}$; the lines $\overline{7,10}$ and $\overline{0,9,1,11,2}$ with slope $U_{s\text{I}}$; the lines $\overline{0,5,10,6}$ and $\overline{9,7}$ with slope U_{I}; and the line $\overline{1,7}$ with slope U_{II}.

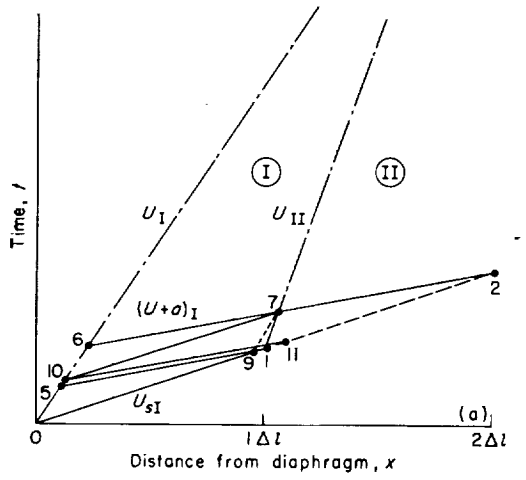

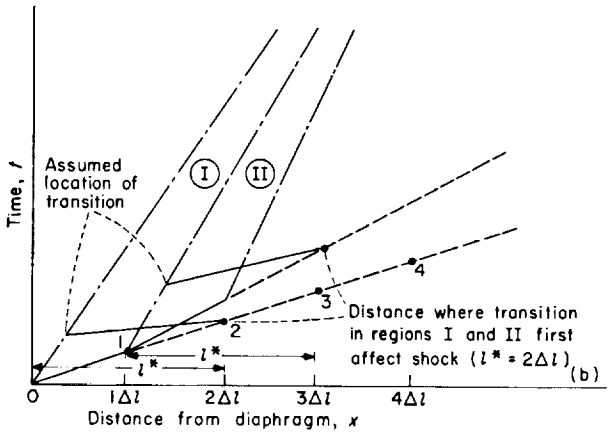

(a) Details for computations of region I.

(b) Details for transitional flow.

FIGURE 9.—Detailed wave diagrams for nonlinear analysis in region β. Short-dashed lines indicate extrapolations.

Therefore, $\xi_7=\overline{9,7}=\overline{0,10}=\xi_{10}$. Thus,

$$\left(\frac{\delta\hat{P}}{a_e}\right)_I\Big|_6^7=\frac{1}{D}\int_{\xi_6}^{\xi_{10}}\left(\frac{\sigma M_s-M_\beta}{\sigma M_s-M_\beta-1}\right)_I c_f\phi\hat{P}_{,I}\,d\xi$$

$$=-\frac{1}{D}\left(\frac{\sigma M_s-M_\beta}{\sigma M_s-M_\beta-1}\right)_I\left(\int_0^{\xi_6} c_f\phi\hat{P}_{,I}\,d\xi - \int_0^{\xi_{10}} c_f\phi\hat{P}_{,I}\,d\xi\right) \quad (53)$$

Thus, the $\hat{P}$ contribution of region (I) to attenuation between 1 and 2 is (from eqs. (45) and (53))

$$\left(\frac{\delta\hat{p}}{p_\beta}\right)_{I,\,l_1\text{ to }l_2}=\frac{\gamma}{2}\frac{a_e}{D}\left(\int_0^{\xi_6} K\Gamma_\beta c_{f,\beta}\,d\xi-\int_0^{\xi_{10}} K\Gamma_\beta c_{f,\beta}\,d\xi\right)$$

$$=\left(\frac{\delta\hat{p}}{p_\beta}\right)_{I,\,0\text{ to }l_2}-\left(\frac{\delta\hat{p}}{p_\beta}\right)_{I,\,0\text{ to }l_{11}} \quad (54)$$

The substitution of equation (40), with g_n replaced by $\hat{g}_n$, into equation (54) yields

$$\left(\frac{\delta\hat{p}}{p_\infty}\right)_{I,\,l_1\text{ to }l_2}=(\hat{g}_n\Omega_n)_I\left(\frac{a_\infty D}{\nu_\infty}\right)^{-\frac{2}{n+3}}\left[\left(\frac{l_2}{D}\right)^{\frac{n+1}{n+3}}-\left(\frac{l_{11}}{D}\right)^{\frac{n+1}{n+3}}\right]$$

$$=(\hat{g}_n\Omega_n)_I\left(\frac{a_\infty D}{\nu_\infty}\right)^{-\frac{2}{n+3}}\left(\frac{l_1}{D}\right)^{\frac{n+1}{n+3}}$$

$$\left[\left(\frac{l_2}{l_1}\right)^{\frac{n+1}{n+3}}-\left(\frac{l_{11}}{l_1}\right)^{\frac{n+1}{n+3}}\right]$$

$$=\left(\frac{\delta\hat{p}}{p_\infty}\right)_{I,\Delta l}\left[\left(\frac{l_2}{l_1}\right)^{\frac{n+1}{n+3}}-\left(\frac{l_{11}}{l_1}\right)^{\frac{n+1}{n+3}}\right] \quad (55)$$

where $\left(\frac{\delta\hat{p}}{p_\infty}\right)_{I,\Delta l}$ is the linear attenuation of a shock due to $\hat{P}$ effects over the initial interval Δl in region (I).

The relationship between l_{11} and l_1 is derived in appendix B and is

$$\frac{l_{11}}{l_1}=Z_I\left(\frac{l_2}{l_1}-1\right) \quad (56)$$

Consequently,

$$\left.\begin{aligned}\left(\frac{\delta\hat{p}}{p_\infty}\right)_{I,\,l_1\text{ to }l_2}&=\left(\frac{\delta\hat{p}}{p_\infty}\right)_{I,\Delta l}\left[\left(\frac{l_2}{l_1}\right)^{\frac{n+1}{n+3}}-(Z_I)^{\frac{n+1}{n+3}}\left(\frac{l_2}{l_1}-1\right)^{\frac{n+1}{n+3}}\right]\\ \left(\frac{\delta\hat{p}}{p_\infty}\right)_{I,\,l_2\text{ to }l_3}&=\left(\frac{\delta\hat{p}}{p_\infty}\right)_{I,\Delta l}\left[\left(\frac{l_3}{l_1}\right)^{\frac{n+1}{n+3}}-(Z_I)^{\frac{n+1}{n+3}}\left(\frac{l_3}{l_1}-1\right)^{\frac{n+1}{n+3}}\right]\\ &\cdots\end{aligned}\right\} \quad (57a)$$

which for equal intervals Δl becomes

$$\left.\begin{aligned}\left(\frac{\delta\hat{p}}{p_\infty}\right)_{\mathrm{I},\,l_1\text{ to }l_2}&=\left(\frac{\delta\hat{p}}{p_\infty}\right)_{\mathrm{I},\Delta l}\left[2^{\frac{n+1}{n+3}}-(Z_1)^{\frac{n+1}{n+3}}\right]\\ \left(\frac{\delta\hat{p}}{p_\infty}\right)_{\mathrm{I},\,l_2\text{ to }l_3}&=\left(\frac{\delta\hat{p}}{p_\infty}\right)_{\mathrm{I},\Delta l}\left[3^{\frac{n+1}{n+3}}-(2Z_1)^{\frac{n+1}{n+3}}\right]\end{aligned}\right\} \tag{57b}$$

In this form the nonlinear attenuations can easily be computed.

In this manner the influence of region Ⓘ on attenuation at any desired value of l may be computed once the attenuation at l_1 has been found. The influence of region Ⓘⓘ is found in a similar manner by shifting the effective origin of the coordinate system to l_1 and finding $\left(\frac{\delta\hat{p}}{p_\infty}\right)_{\mathrm{II}}$ for the attenuated shock strength at l_1; that is,

$$\left(\frac{\delta\hat{p}}{p_\infty}\right)_{\mathrm{II},\,l_1\text{ to }l_2}=\left(\frac{\delta\hat{p}}{p_\infty}\right)_{\mathrm{II},\Delta l}=(\hat{\eta}_n\Omega_n)_{\mathrm{II}}\left(\frac{a_\infty D}{\nu_\infty}\right)^{-\frac{2}{n+3}}\left(\frac{l_2-l_1}{D}\right)^{\frac{n+1}{n+3}} \tag{58a}$$

$$\left(\frac{\delta\hat{p}}{p_\infty}\right)_{\mathrm{II},\,l_2\text{ to }l_3}=\left(\frac{\delta\hat{p}}{p_\infty}\right)_{\mathrm{II},\Delta l}\left[\left(\frac{l_3-l_1}{l_2-l_1}\right)^{\frac{n+1}{n+3}}-(Z_{\mathrm{II}})^{\frac{n+1}{n+3}}\left(\frac{l_3-l_1}{l_2-l_1}-1\right)^{\frac{n+1}{n+3}}\right] \tag{58b}$$

. . . . .

or for equal intervals of Δl,

$$\left.\begin{aligned}\left(\frac{\delta\hat{p}}{p_\infty}\right)_{\mathrm{II},\,l_2\text{ to }l_3}&=\left(\frac{\delta\hat{p}}{p_\infty}\right)_{\mathrm{II},\Delta l}\left[2^{\frac{n+1}{n+3}}-(Z_{\mathrm{II}})^{\frac{n+1}{n+3}}\right]\\ \left(\frac{\delta\hat{p}}{p_\infty}\right)_{\mathrm{II},\,l_3\text{ to }l_4}&=\left(\frac{\delta\hat{p}}{p_\infty}\right)_{\mathrm{II},\Delta l}\left[3^{\frac{n+1}{n+3}}-(2Z_{\mathrm{II}})^{\frac{n+1}{n+3}}\right]\\ .\quad .\quad .\quad .\quad .\end{aligned}\right\} \tag{58c}$$

The total nonlinear attenuation at a distance l from the diaphragm station which has been subdivided into several intervals Δl is then expressed as the sum of the linear contributions of region α and the reflections from region β added to the nonlinear contributions of region β. The following expression is obtained for the nonlinear attenuation:

$$\begin{aligned}\frac{\delta p}{p_\infty}=&(\Omega g)_{\alpha,m}\left(\frac{a_\infty D}{\nu_\infty}\right)^{-\frac{2}{m+3}}\left(\frac{l}{D}\right)^{\frac{m+1}{m+3}}+\frac{1-K}{K}\left(\frac{\delta\hat{p}}{p_\infty}\right)_{\mathrm{I},\Delta l}\left(\frac{l}{\Delta l}\right)^{\frac{m+1}{m+3}}+\left(\frac{\delta\hat{p}}{p_\infty}\right)_{\mathrm{I},\Delta l}\\ &\left\{1+\left[2^{\frac{m+1}{m+3}}-(Z_{\mathrm{I}})^{\frac{m+1}{m+3}}\right]+\left[3^{\frac{m+1}{m+3}}-(2Z_{\mathrm{I}})^{\frac{m+1}{m+3}}\right]+\cdots+\left[\left(\frac{l}{\Delta l}\right)^{\frac{m+1}{m+3}}-\left(\frac{l-\Delta l}{\Delta l}Z_{\mathrm{I}}\right)^{\frac{m+1}{m+3}}\right]\right\}+\left(\frac{\delta\hat{p}}{p_\infty}\right)_{\mathrm{II},\Delta l}\\ &\left\{1+\left[2^{\frac{m+1}{m+3}}-(Z_{\mathrm{II}})^{\frac{m+1}{m+3}}\right]+\cdots+\left[\left(\frac{l-\Delta l}{\Delta l}\right)^{\frac{m+1}{m+3}}-\left(\frac{l-2\Delta l}{\Delta l}Z_{\mathrm{II}}\right)^{\frac{m+1}{m+3}}\right]\right\}+\cdots\left(\frac{\delta\hat{p}}{p_\infty}\right)_{N=l/\Delta l,\Delta l}\end{aligned} \tag{59a}$$

$$\frac{\delta p}{p_\infty}=\left(\frac{\delta p}{p_\infty}\right)_{\alpha,m}+\frac{1-K}{K}\left(\frac{\delta\hat{p}}{p_\infty}\right)_{\mathrm{I},\Delta l}\left(\frac{l}{\Delta l}\right)^{\frac{m+1}{m+3}}+\sum_{N=1}^{N=\frac{l}{\Delta l}}\left(\frac{\delta\hat{p}}{p_\infty}\right)_{N,\Delta l}\sum_{i=1}^{i=1-n+\frac{\Delta l}{i}}\left\{(i)^{\frac{m+1}{m+3}}-\left[(i-1)Z_N\right]^{\frac{m+1}{m+3}}\right\} \tag{59b}$$

where i is the index.

Second-order attenuation in the presence of transition may also be treated by this regional system. The contributions of α and of Q and S in β are still treated as entirely linear but including transition. Equation (39a) applies in its entirety to the α contribution; and, when the first term on the right-hand side is multiplied by $1-K_m$ and the second term by $1-K_n$, the resulting equation gives the Q and S contribution of region β.

The transitional $\hat{P}$ contribution is treated as follows: Let l^* be the position of the shock at which the transition in the flow behind the shock first affects the shock. The wave diagram for transition is shown in figure 9(b) where for illustrative purposes it is assumed that $l^*=2\Delta l$. Now, in order to retain the facility of computation afforded by the regional system with equal Δl and a constant l^*, the value of R^* will, as a result, vary slightly from region to region. Since $\left(\frac{R^*}{l^*}\right)_N=\left(\frac{U}{\nu}\frac{\xi^*}{l^*}\right)_N$ the magnitude of this variation may be found by examination of figure 10 which shows the parameter

$$\left(\frac{U}{\nu}\frac{\xi^*}{l^*}\right)_N\frac{p_{\infty,std}}{p_\infty}$$

plotted against shock pressure ratio. From this figure it is evident that, if the shock pressure ratio should attenuate, for example, from 20 to 15, or from 5 to $4\frac{1}{2}$, there would be about a 10-percent decrease in R^* for a given l^* and $p_{\infty,std}/p_\infty$. The errors introduced by such a variation in R^* are not deemed to be important enough to force the abandonment of the equal Δl computing scheme. For the remainder of this paper, R^* will be taken as the value of the transitional Reynolds number in region ①. The $\delta\hat{p}$ contributions for the transitional case are expressed by the following equations which are modifications of equations (57), (58), and (59) (the subscripts m and n refer to conditions before and after transition, respectively):

$$\left(\frac{\delta\hat{p}}{p_\infty}\right)_{N,m,\Delta l}=(\hat{g}_m\Omega_m)_N\left(\frac{a_\infty D}{\nu_\infty}\right)^{-\frac{2}{m+3}}\left(\frac{\Delta l}{D}\right)^{\frac{m+1}{m+3}} \tag{60a}$$

$$\left(\frac{\delta\hat{p}}{p_\infty}\right)_{N,n,\Delta l}=(\hat{g}_n\Omega_n)_N\left(\frac{a_\infty D}{\nu_\infty}\right)^{-\frac{2}{n+3}}\left(\frac{\Delta l}{D}\right)^{\frac{n+1}{n+3}} \tag{60b}$$

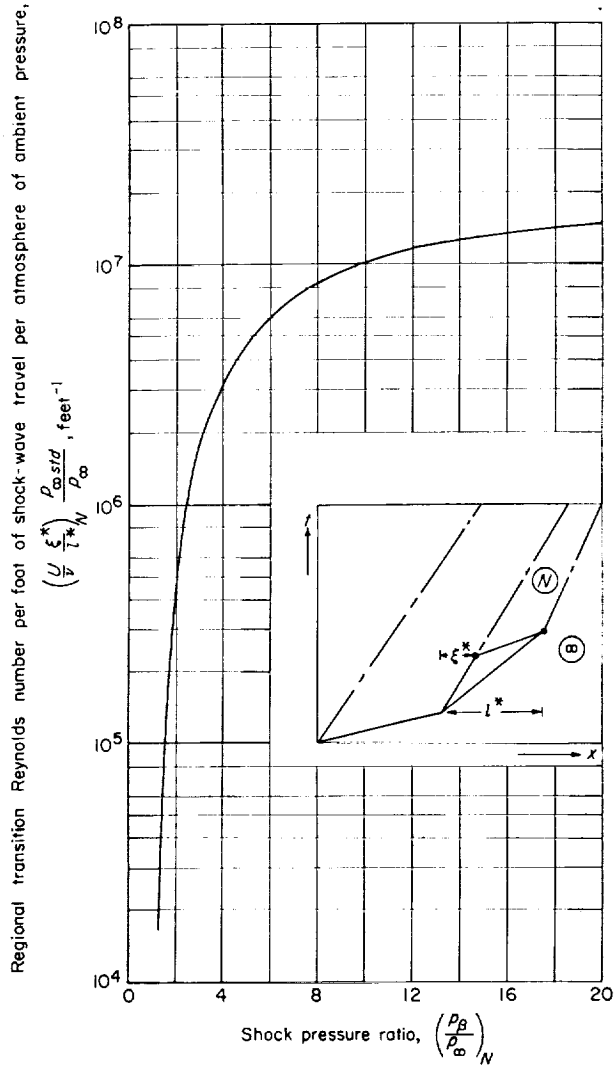

FIGURE 10.—Regional transition Reynolds number per foot of shock-wave travel per atmosphere of ambient pressure plotted against shock pressure ratio. Circled symbols denote regions.

$$\left(\frac{\delta\hat{p}}{p_\infty}\right)_{N,m,(l-\Delta l)\text{ to }l}=\left(\frac{\delta\hat{p}}{p_\infty}\right)_{N,m,\Delta l}\left[\left(\frac{l}{\Delta l}-N+1\right)^{\frac{m+1}{m+3}}-\left(\frac{l}{\Delta l}-N\right)^{\frac{m+1}{m+3}}(Z_N)^{\frac{m+1}{m+3}}\right] \tag{61a}$$

for

$$\frac{l}{\Delta l}\leqq N-1+\frac{l^*}{\Delta l}$$

$$\left(\frac{\delta\hat{p}}{p_\infty}\right)_{N,n,(l-\Delta l)\text{ to }l}=\left(\frac{\delta\hat{p}}{p_\infty}\right)_{N,n,\Delta l}\left[\left(\frac{l}{\Delta l}-N+1\right)^{\frac{n+1}{n+3}}-\left(\frac{l}{\Delta l}-N\right)^{\frac{n+1}{n+3}}(Z_N)^{\frac{n+1}{n+3}}\right] \tag{61b}$$

for

$$\frac{l}{\Delta l}>N-1+\frac{l^*}{\Delta l}$$

NUMERICAL EVALUATION OF NONLINEAR THEORY

Several computations to determine the nonlinear correction factors for attenuation were performed for values of the interval $\Delta l/D$ of 3.5 and 14. These particular values were chosen because they represent increments of Δl of 0.5 foot and 2 feet for the shock tube employed in the experiments to be described in a later section. Typical curves resulting from such computations are shown in figure 11. The ratio of the nonlinear attenuation to the linear attenuation is plotted against l/D for an initial shock pressure ratio of 4 and a value of $\frac{a_\infty D}{\nu_\infty}$ of 0.01×10^6. For values of $l/D>50$ the curves for $\frac{\Delta l}{D}=3.5$ and 14 agree within about 1 percent for the laminar case and within about 3 percent for the turbulent case. The low value of $a_\infty D/\nu_\infty$ accentuates any variations between the two computations; thus the case illustrated gives a discrepancy near a maximum rather than near a minimum. Examination of several such pairs of curves resulted in the conclusion that the slight increase in accuracy obtained by using $\frac{\Delta l}{D}=3.5$ did not justify the fourfold increase in labor. Consequently, the computations with $\frac{\Delta l}{D}=14$ are used to predict the nonlinear attenuation for $l/D\gtrless50$.

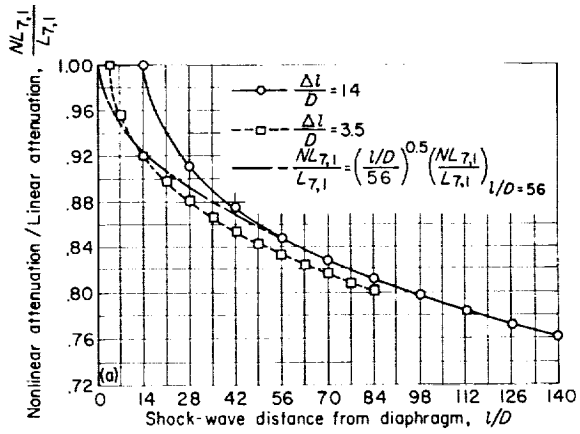

(a) Turbulent flow in α; laminar flow in β.

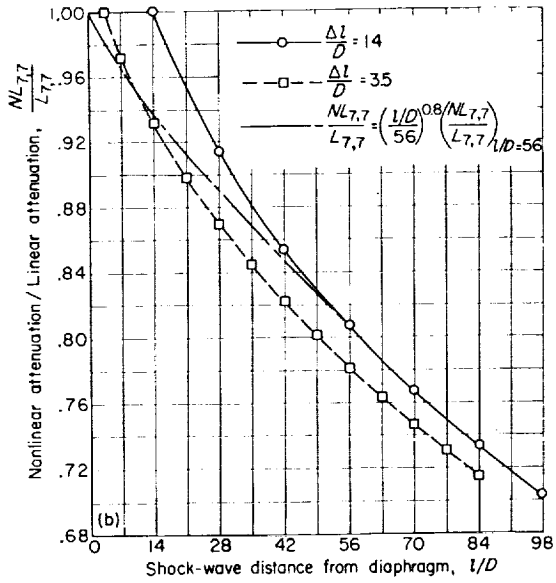

(b) Turbulent flow in both α and β.

FIGURE 11.—Ratio of nonlinear to linear attenuation plotted against shock-wave position for $\frac{p_{s_0}}{p_\infty}=4.0$ and $\frac{a_\infty D}{\nu_\infty}=0.01\times10^6$.

FIGURE 11.—Concluded

It is obvious that the finite size of Δl will introduce errors in the ratios $NL_{m,n}/L_{m,n}$ which are largest near $l\to0$ since the nonlinear and linear attenuations are identical for the first interval. (See fig. 11.) However, the errors introduced in the attenuations $NL_{m,n}$ themselves are small since $L_{m,n}\to0$ as $l\to0$. To represent the physical flow in this region accurately would require that Δl approach 0. Interpolation formulas giving acceptable accuracy near $l\to0$ are assumed to have the form

$$\left.\begin{aligned}\frac{\text{Nonlinear attenuation}}{\text{Linear attenuation}}&=(\text{Constant})\left(\frac{l}{D}\right)^{0.5}\\ \frac{\text{Nonlinear attenuation}}{\text{Linear attenuation}}&=(\text{Constant})\left(\frac{l}{D}\right)^{0.8}\end{aligned}\right\}\quad(62)$$

for $\left(0<\frac{l}{D}\leqq56\right)$ for laminar and turbulent flows, respectively, since the linear attenuation is proportional to $(l/D)^{0.5}$ and $(l/D)^{0.8}$ for the laminar and turbulent flows.

The constants are chosen to match the computed

curves for $\frac{\Delta l}{D}=14$ at $\frac{l}{D}=56$. From figure 11 it is evident that the errors resulting from the application of this interpolation formula are less than the aforementioned errors at $\frac{l}{D}=50$ and are thus acceptable.

In order to obtain curves of the transitional nonlinear to linear attenuation ratio $NL_{\tau,T}/L_{\tau,T}$ for a constant value of R^* and several shock pressure ratios, a cross-plotting technique was used. At a given shock pressure ratio the values of $NL_{\tau,T}/L_{\tau,T}$ were computed for several values of the ratio l^*/D to $\Delta l/D$. Since each l^* represented an R^*, the resulting ratios for each l/D could be plotted against R^* for a given shock pressure ratio. The values for a particular R^* could then be read from these plots to produce a master plot with a common value of R^*.

Plots of the ratio of nonlinear attenuation to linear attenuation are shown in figures 12 to 15. In these curves region α is always considered as having turbulent flow whereas four cases are considered for region β: namely, (a) laminar flow, (b) turbulent flow, (c) transition with $R^*=1.25\times10^6$, and (d) transition with $R^*=2.5\times10^6$. The cross-plotting parameters are shock-tube Reynolds number $a_\infty D/\nu_\infty$ and length of shock-wave travel expressed in hydraulic diameters l/D. At the lower pressure ratios $p_{\beta o}/p_\infty$, curves for more values of $a_\infty D/\nu_\infty$ are shown than at the higher pressure ratios. This limitation resulted from the considerations of the restriction of the validity of the theory to an ideal gas, the region of experimental data of this report, the most likely general region of experiments for other facilities, and priority for computing effort. Since figures 12 to 15 are the result of cross plotting, the accuracy is assumed to be about 2 percent.

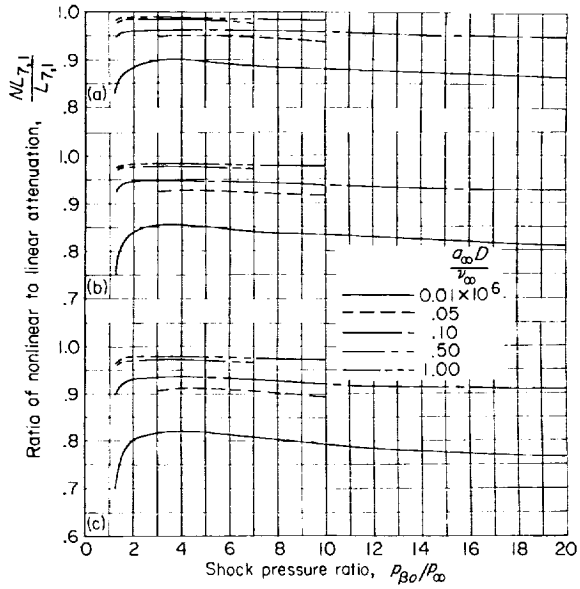

(a) $\frac{l}{D}=25$.

(b) $\frac{l}{D}=50$.

(c) $\frac{l}{D}=75$.

FIGURE 12.—Ratio of nonlinear attenuation to linear attenuation for region α turbulent and region β laminar plotted against shock pressure ratio. The shock wave is located at a distance l/D from the diaphragm station.

569768—61——4

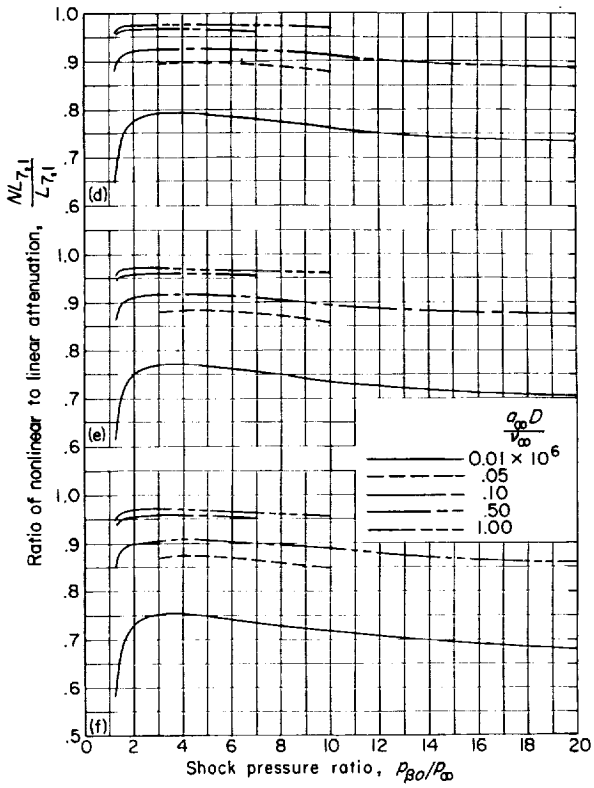

(d) $\frac{l}{D}=100$.

(e) $\frac{l}{D}=125$.

(f) $\frac{l}{D}=150$.

FIGURE 12.—Concluded.

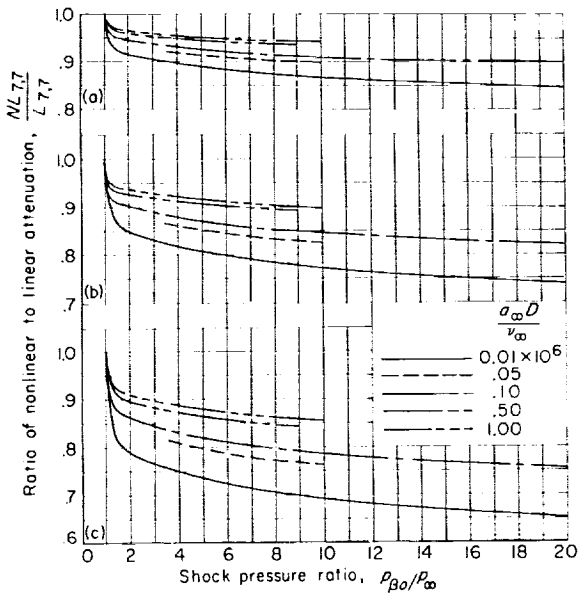

(a) $\frac{l}{D}=25.$

(b) $\frac{l}{D}=50.$

(c) $\frac{l}{D}=75.$

FIGURE 13. Ratio of nonlinear attenuation to linear attenuation for both regions α and β turbulent plotted against shock pressure ratio. The shock wave is located at a distance l/D from the diaphragm station.

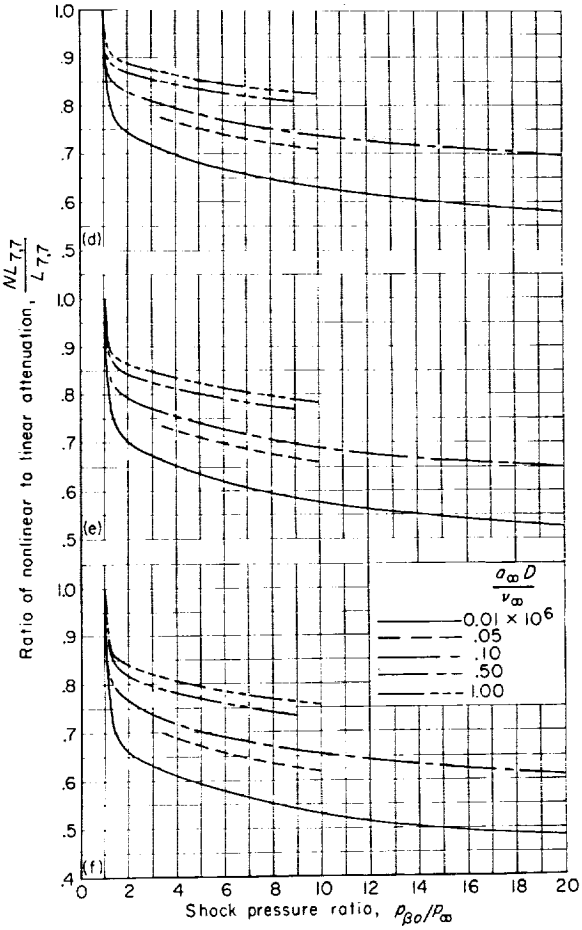

(d) $\frac{l}{D}=100.$

(e) $\frac{l}{D}=125.$

(f) $\frac{l}{D}=150.$

FIGURE 13. Concluded.

An analytic closed-form investigation has been made of the fact that the limit of $NL_{7,1}/L_{7,1}$ approaches 0 when $p_{\beta o}/p_\infty$ approaches 1 whereas the limit of $NL_{7,7}/L_{7,7}$ approaches 1.0 when $p_{\beta o}/p_\infty$ approaches 1.0. This second-order analytic solution for weak shocks indicates that a value of $n=3$ in β is a critical value; all solutions with $n>3$ approach a limit of 1 and those with $n<3$ approach a limit of 0. Of course, in all cases the absolute value of both the linear and nonlinear attenuation must approach zero as $p_{\beta o}/p_\infty$ approaches 1. Since α has only a secondary effect on attenuation and since the expansion fan has been replaced by a "negative shock," the refinement of transition in region α was not deemed necessary.

RESULTS AND DISCUSSION

EXPERIMENTAL APPARATUS AND PROCEDURE

Extensive shock-attenuation data were obtained in a high-pressure shock tube 2 inches high by 1½ inches wide in the Langley gas dynamics laboratory. This shock tube is the same as that described in reference 1 with added velocity-measuring equipment. Light screens placed at eight stations in the low-pressure section made possible measurements of the complete distance-time history of the motion of the shock wave for a wide range of shock pressure ratios and flow Reynolds numbers. Figure 16 shows schematically the arrangement of the shock tube and associated equipment, and the low-pressure section with associated optical systems is illustrated in figure 17.

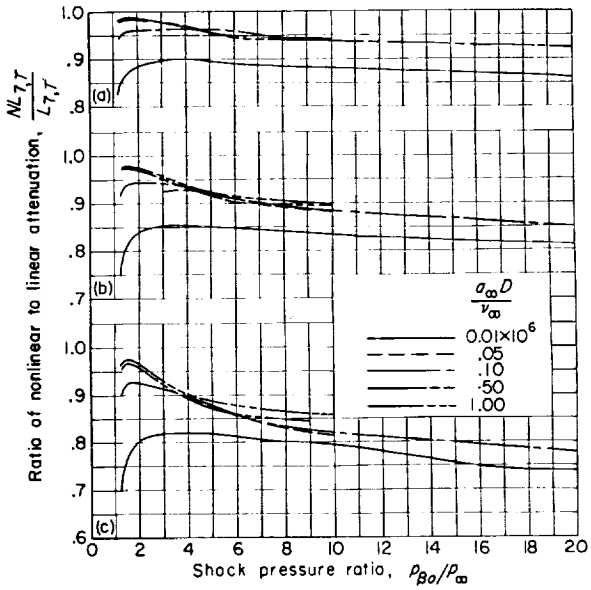

(a) $\frac{l}{D}=25$.

(b) $\frac{l}{D}=50$.

(c) $\frac{l}{D}=75$.

FIGURE 14.—Ratio of nonlinear attenuation to linear attenuation for region α turbulent and region β transitional plotted against shock pressure ratio. $R^*=1.25\times10^6$. The shock wave is located at a distance l/D from the diaphragm station.

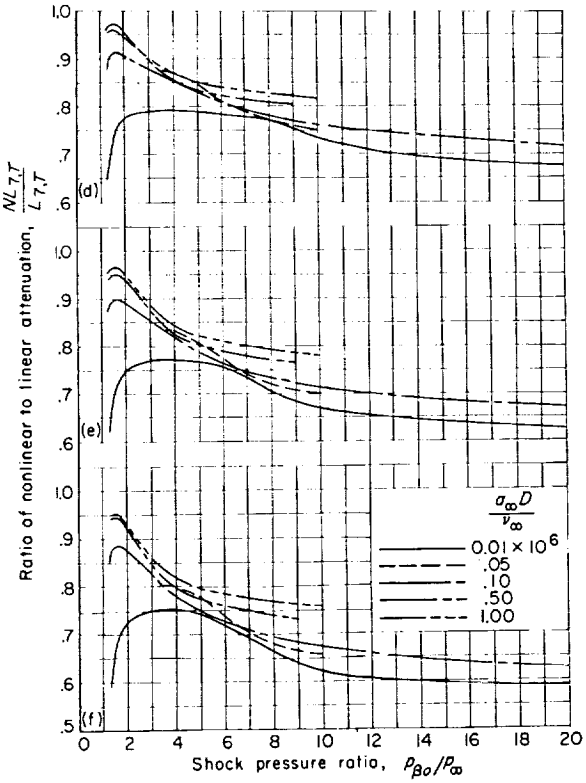

(d) $\frac{l}{D}=100$.

(e) $\frac{l}{D}=125$.

(f) $\frac{l}{D}=150$.

FIGURE 14.– Concluded.

Air at room temperature was used in both high- and low-pressure sections. The normal arrangement for high-pressure section air supply and low-pressure section vacuum systems is shown in figure 16. In a limited number of low-density runs, evacuating the high-pressure section was necessary; for these cases, an auxiliary vacuum system, identical with the normal low-pressure system, was substituted for the pressure system shown. Conversely, certain high-density runs required pressurization of the low-pressure section; in this case a simple pressure system replaced the normal vacuum system. The pressures in both high- and low-pressure sections were adjusted for each run. All data were obtained from tests where the diaphragm was punctured by a hand-operated plunger. In this way diaphragm pressure ratio and consequently, theoretical shock-pressure ratio $p_{\beta o}/p_\infty$ were closely controlled. Bourdon-tube gages were employed for pressure measurements, and the vacuum systems utilized a modified barometer for pressures in the range from 4 inches mercury absolute to atmospheric pressure, and a 0 to 100 millimeters mercury absolute pressure gage was used for the low pressures.

Static pressures were structurally limited to 1,000 pounds per square inch gage in the high-pressure sections and 250 pounds per square inch gage in the low-pressure sections. A vacuum limitation of about 0.01 atmosphere absolute pressure resulted for the low-pressure section because the light screen systems became unresponsive for the low pressures. In the high-pressure section, low pressures were limited by failure of diaphragms to burst properly.

Diaphragms made of thin metal foil were used for the low-pressure runs. The most useful materials were soft aluminum foil, 0.001 inch thick, and soft brass foil with a nominal thickness of

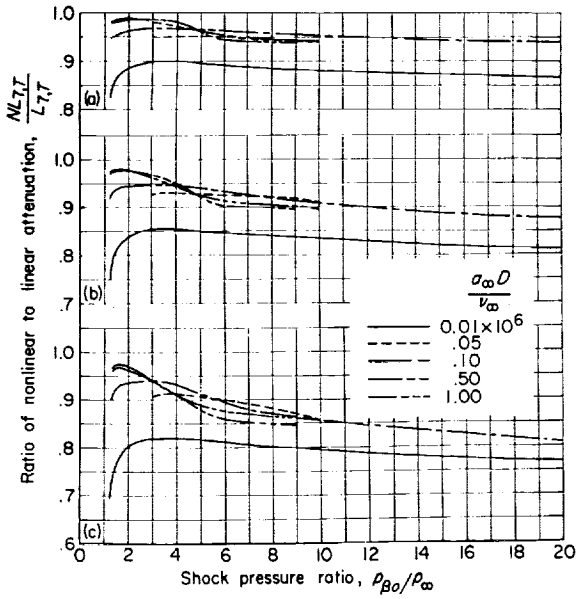

(a) $\frac{l}{D}=25$.

(b) $\frac{l}{D}=50$.

(c) $\frac{l}{D}=75$.

FIGURE 15. Ratio of nonlinear attenuation to linear attenuation for region α turbulent and region β transitional plotted against shock pressure ratio. $R^*=2.50\times10^6$. The shock wave is located at a distance l/D from the diaphragm station.

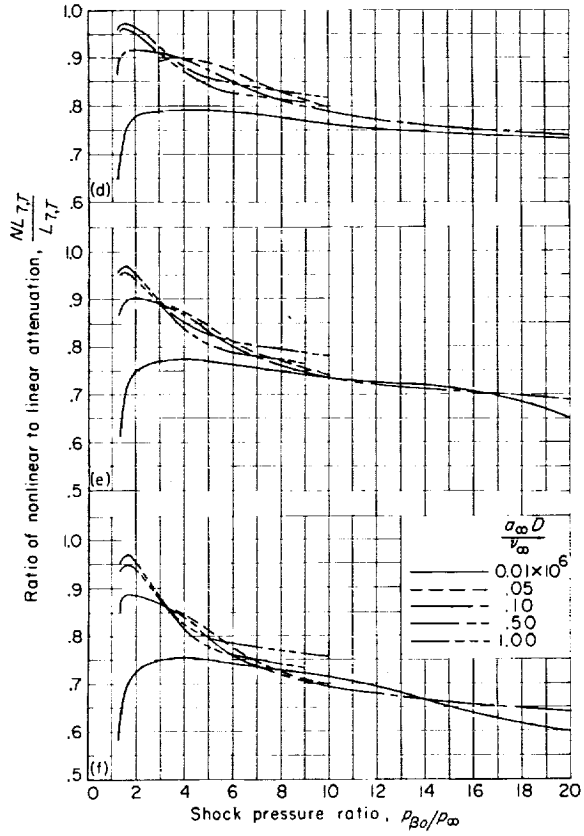

(d) $\frac{l}{D}=100$.

(e) $\frac{l}{D}=125$.

(f) $\frac{l}{D}=150$.

FIGURE 15.—Concluded.

either 0.00125 or 0.0015 inch. With these materials, it was possible to obtain good bursts for pressure differences across the diaphragm ranging from 10 pounds per square inch to 100 pounds per square inch. Good bursts for the range of pressure difference from 100 to 1,000 pounds per square inch were obtained by using spring-tempered brass shim stock with thicknesses ranging from 0.008 to 0.021 inch and scribed to various depths in an x-shaped pattern along the diagonals of a rectangle representing the shock-tube cross section. When punctured under pressure, the diaphragm split along the scribe marks, and the four triangular pieces of material folded back against the wall and presented minimum resistance to the flow. All other conditions being equal, runs where this type of burst took place resulted in minimum shock attenuation compared with attenuations resulting from bursts where metal or acetate-type diaphragms were shattered. Material thicknesses and scribe depths were determined so that puncturing pressure was just below the pressure at which the diaphragm would have failed. The unscribed foil diaphragms used for small pressure differences split along the diagonals in this same way when punctured at the center, and optimum results were also generally obtained with these diaphragms.

Shock velocity measurements were made with miniature schlieren systems located at eight positions in the low-pressure section. Figure 16 shows schematically the position of these systems. The optical and electronic systems were essentially the same as those used in reference 1, in which the signal generated in a photomultiplier tube by deflection of a beam of light upon the tube was

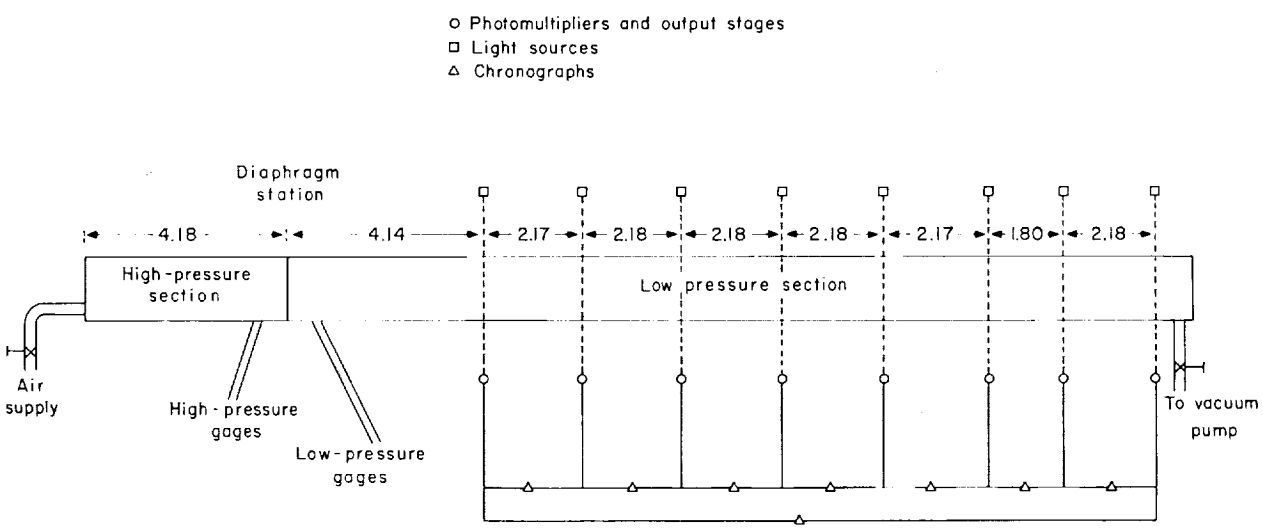

FIGURE 16. Schematic diagram of experimental setup for obtaining attenuation data. Distances are in feet.

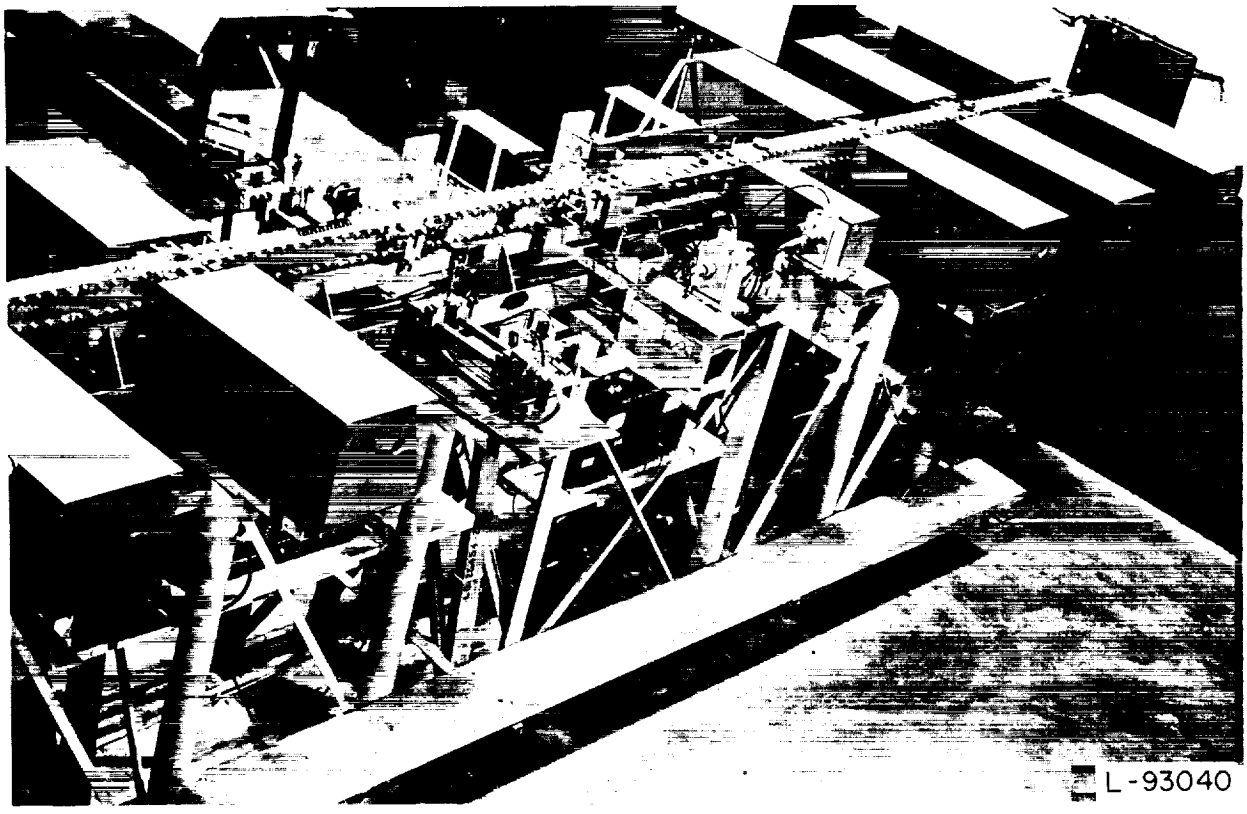

FIGURE 17.—Photograph of experimental setup showing shock-tube low-pressure section with velocity-measuring stations.

amplified and used to trigger a thyratron. The thyratron output pulse, in turn, started or stopped a counter chronograph. Figure 18 illustrates one complete optical system, including the chassis containing the photomultiplier-amplifier-thyratron circuit, which is shown in figure 19. Wooden shields were employed to keep stray room light from falling upon the photomultiplier tube.

For the multiple systems employed herein, each thyratron output pulse was channeled to two

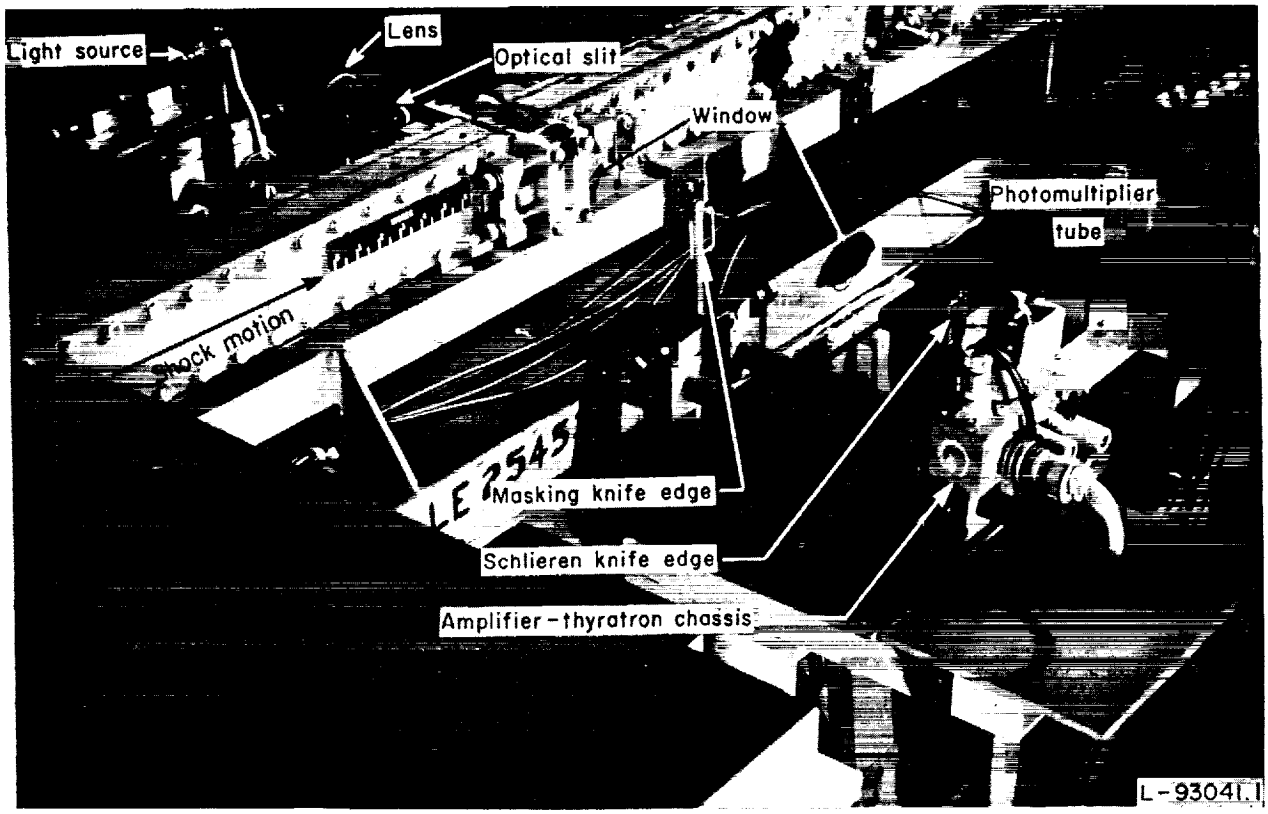

FIGURE 18.—Photograph showing details of velocity-measuring optical system.

chronographs. These chronographs indicated shock traversal time between any two adjacent stations, and any one of three types of chronographs, 8 megacycles, 1.6 megacycles, and 1 megacycle, was employed for each position. The overall time interval between the first and last stations was measured with a 100-kilocycle chronograph for a check upon the sum of the individual measurements.

REDUCTION OF EXPERIMENTAL DATA

The experimental shock-wave pressure ratio was computed from the measured time interval Δt for the shock to pass between two measuring stations a distance Δl apart from the relation

$$\frac{p_{vs}}{p_\infty}=\frac{2\gamma}{\gamma+1}\left(\frac{\Delta l/\Delta t}{a_\infty}\right)^2-\frac{\gamma-1}{\gamma+1} \tag{63}$$

This value was assumed to represent the shock strength at a position midway between the two stations, and the maximum error was estimated to be less than 1 percent. The theoretical shock pressure ratio p_{β_0}/p_∞ was computed from the diaphragm pressure ratio just prior to burst. For an ideal gas the maximum error in p_{β_0} was estimated at $0.1p_\infty$ (for a shock pressure ratio of 10 at $p_\infty=0.005p_{\infty,std}$); and the maximum deviation in the ratio of computed $(p_\beta/p_\infty)_0$ to true $(p_\beta/p_\infty)_0$ was estimated to be approximately 1 percent.

COMPARISON OF THEORY AND EXPERIMENT

The general method of comparison between theory and experiment will be to compare the measured and predicted attenuation for particular values of p_{β_0}/p_∞ and $a_\infty D/\nu_\infty$ on individual curves. However, it is of interest to first consider a few typical curves where the data for a constant value of p_{β_0}/p_∞ but with varying values of $a_\infty D/\nu_\infty$ are shown on a single plot. Such plots are shown in figure 20 for values of p_{β_0}/p_∞ of 4.0 and 10.0. The experimental data are averages of several runs on a given day and the number of runs for each data point is indicated on the figure. On some runs in which the density change across the shock wave was small, all the velocity-measuring stations did not register because of variations in their sensitivity; and, as a result, there are gaps in the

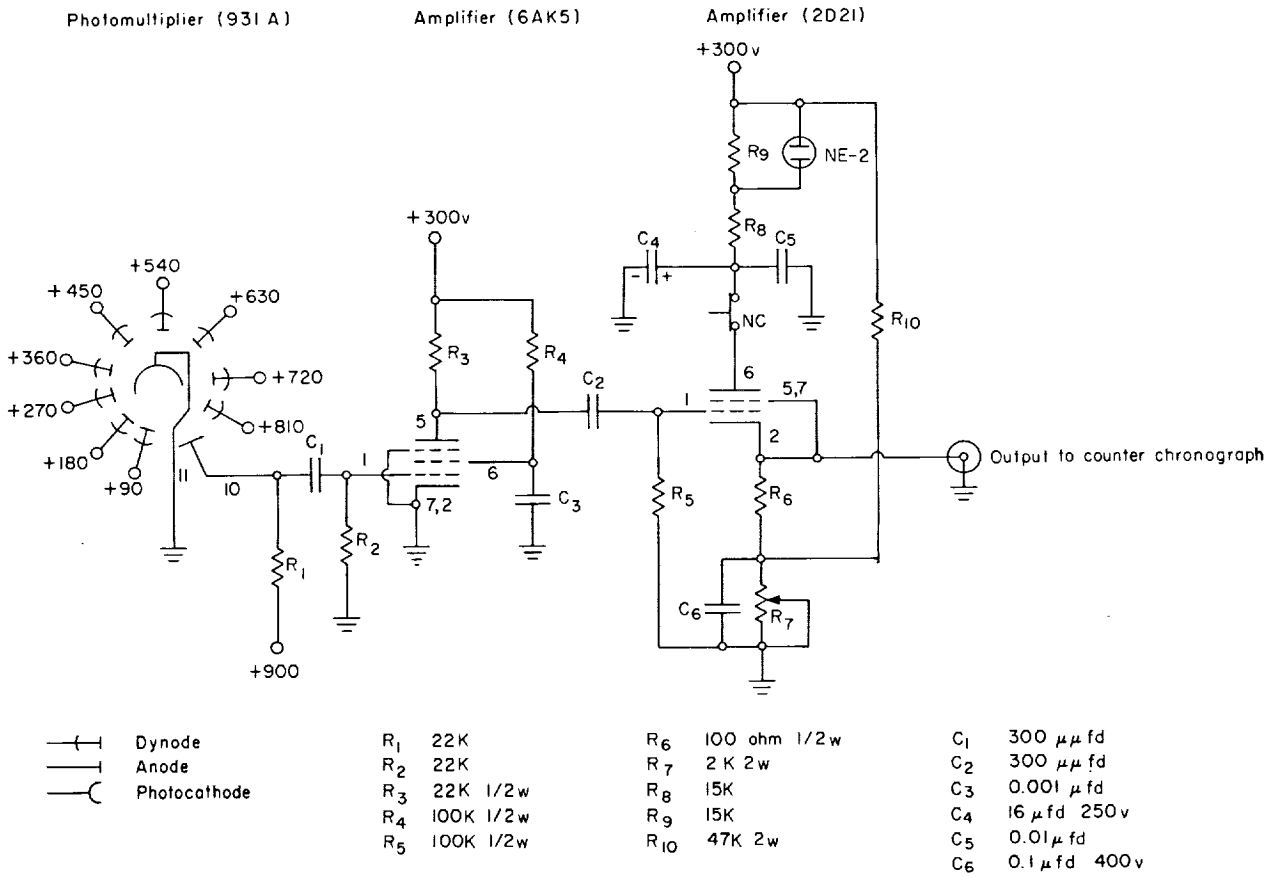

FIGURE 19.—Schematic diagram of photomultiplier and output stages for shock velocity-measuring system.

experimental data. (For example, see fig. 20(b) at $\frac{a_\infty D}{\nu_\infty}=0.005$.)

One fact immediately evident is the nonrepeatability of some of the data, even when compared on a daily average basis. An allowance for an error in p_β/p_∞ of ± 1 percent in the experimental and data-reduction technique will bracket most of the observed discrepancy in the averages; but certain runs at very low values of $a_\infty D/\nu_\infty$ still fall outside this range.

If an attempt were made to extrapolate a curve from the data points to $l=0$, an inflection would often be required in the curve between $l=0$ and $l=6$ to make it pass through the theoretical value of p_{β_0}/p_∞ at $l=0$. In order to illustrate this point, connecting lines have been drawn in figure 20 for some of the values of $a_\infty D/\nu_\infty$. Similar behavior is found in the experimental data reported in figures 11 to 14 of reference 8. Now all the attenuation theories based on wall effects which are known to the authors predict $\frac{d^2 p_{rs}/p_\infty}{dl^2}>0$ in regions of laminar or turbulent flow. At the transition point the theory of the present paper usually predicts $\left(\frac{dp_{rs}/p_\infty}{dl}\right)_{laminar}>\left(\frac{dp_{rs}/p_\infty}{dl}\right)_{transition}<0$. Consequently, if this inflection is to arise from wall effects, it must be caused by transition. The interferometric studies of reference 16 have found values of R^* of about 1.4×10^6 and 2.0×10^6 for $p_{\beta_0}/p_\infty=2$ and 24, respectively. Since values of R^* of the order of 0.5×10^6 are required to cause an inflection at $l=6$ for $p_{\beta_0}/p_\infty=4$ and 10, it does not appear likely that transition is the cause of this inflection. This inflection will be discussed more fully later in this paper.

The unexpected inversion of Reynolds number effects for the lower values of l should be noted. For example, at $l=5.2$ and $p_{\beta_0}/p_\infty=10$ the attenuation for $\frac{a_\infty D}{\nu_\infty}=0.005\times10^6$ is about one-fourth that

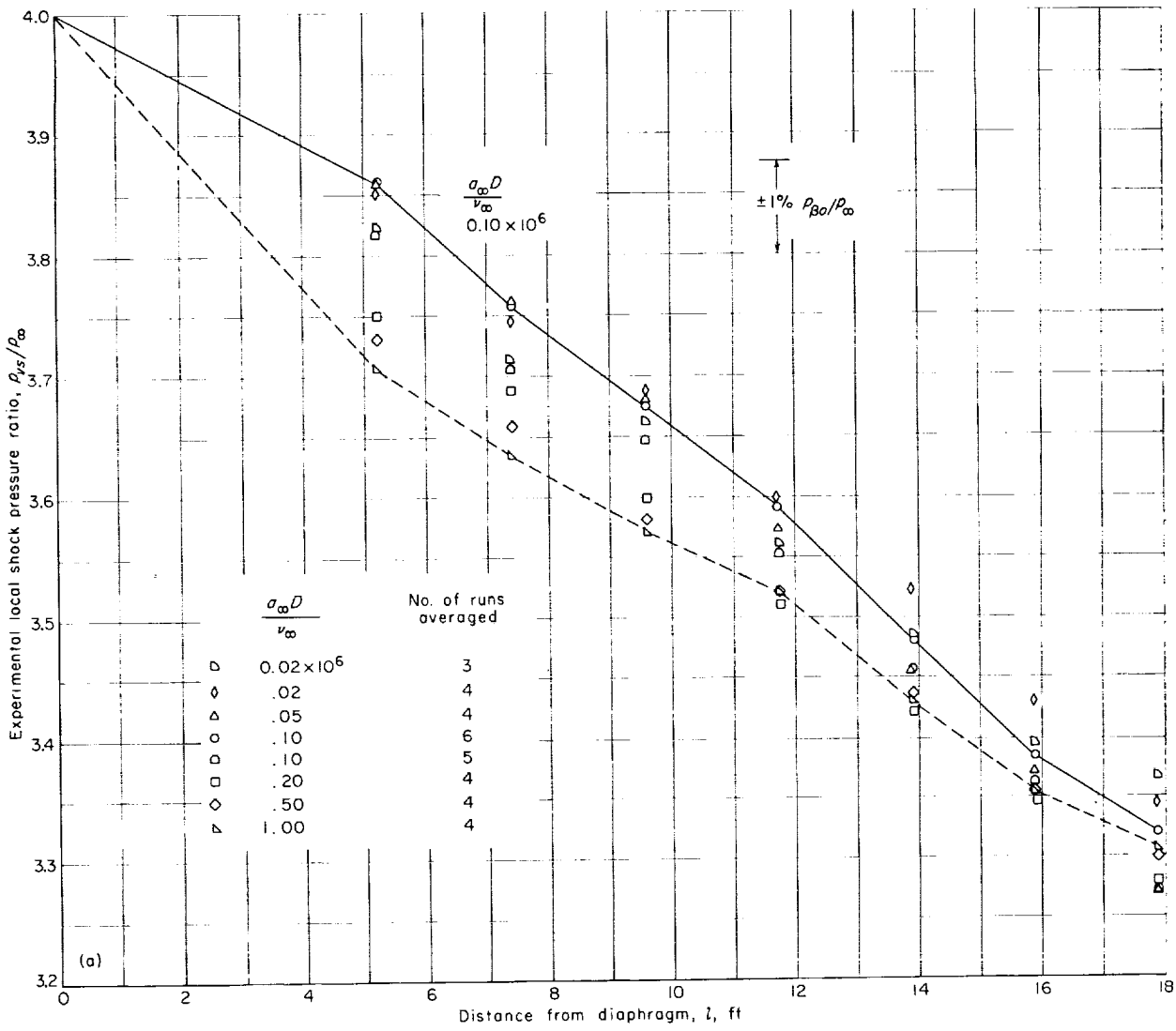

(a) $\frac{p_{\beta o}}{p_\infty}=4.0$.

FIGURE 20.—Plot of experimental averaged local shock pressure ratio plotted against shock distance from diaphragm.

for $\frac{a_\infty D}{\nu_\infty}=0.1\times10^6$. For the same value of l and $\frac{p_{\beta o}}{p_\infty}=4.0$, the attenuation for $\frac{a_\infty D}{\nu_\infty}=0.1\times10^6$ is about one half that for $\frac{a_\infty D}{\nu_\infty}=1\times10^6$.

The spread with Reynolds number of the experimental data at the larger values of l is also much smaller than would be expected on the basis of the linear theories (refs. 1 and 2) which predict attenuations at a given l/D proportional to $\left(\frac{a_\infty D}{\nu_\infty}\right)^{-\frac{1}{2}}$ and $\left(\frac{a_\infty D}{\nu_\infty}\right)^{-\frac{1}{3}}$ for laminar and turbulent flow, respectively. This behavior has been noted by other investigators (ref. 10).

Theoretical variation of p_{vs}/p_∞ with l for values of $\frac{a_\infty D}{\nu_\infty}=0.01\times10^6$, 0.1×10^6, and 1×10^6 for $p_{\beta o}/p_\infty=4.0$ and 10.0 are presented in figures 21 and 22. These values are based on the theory of the present paper. Laminar and turbulent linear and nonlinear pressure-distance predictions are shown in figure 21(a) for $p_{\beta o}/p_\infty=4.0$, and in figure 21(b) for $p_{\beta o}/p_\infty=10.0$. The effect at larger values of l of the nonlinear correction is twofold; not only is there a marked reduction in

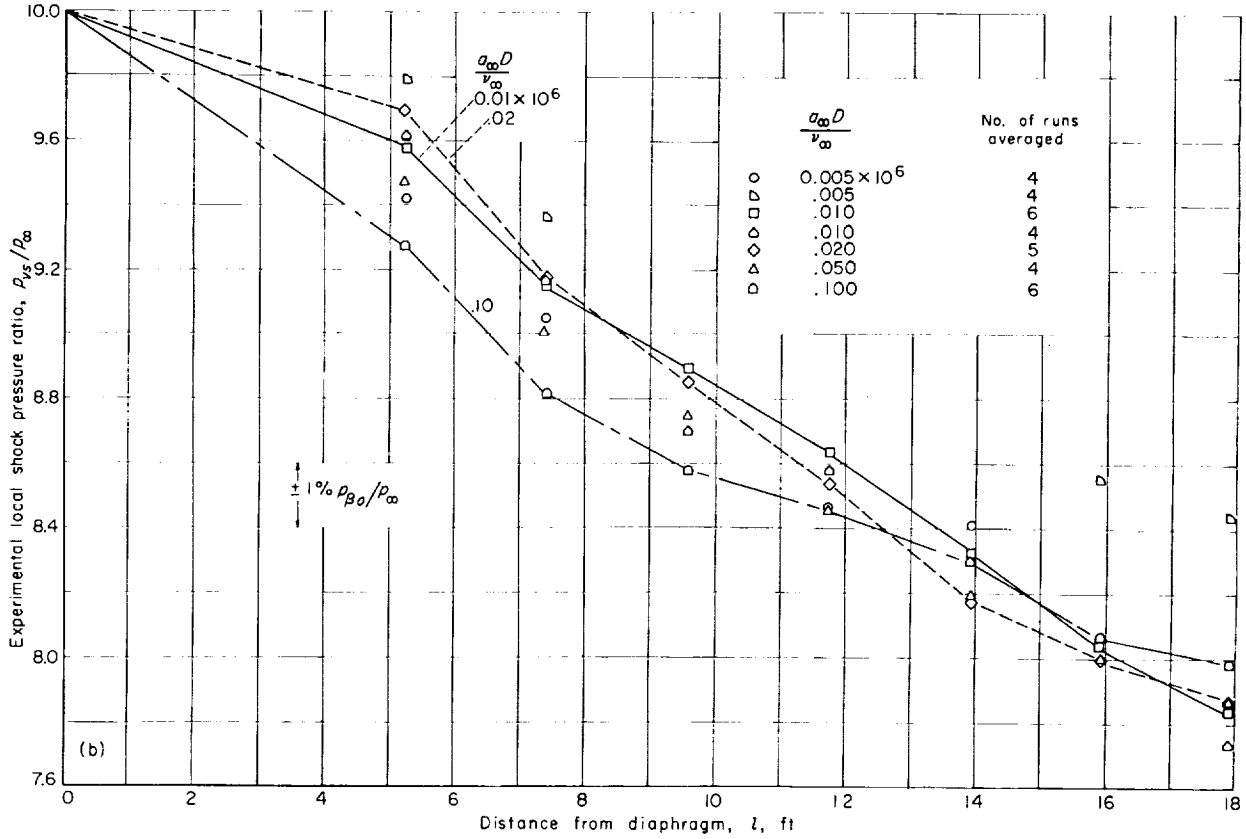

(b) $\frac{p_{\beta o}}{p_\infty}=10.0$.

FIGURE 20.—Concluded.

the predicted attenuation when the attenuation is large but there is also a marked decrease in the predicted Reynolds number effect on attenuation. The following table based on figures 21 and 22 for $l=22$ feet illustrates these facts:

Curve	Figure	Values of $\left(\frac{p_{\beta o}}{p_\infty}\right)-\left(\frac{p_{ss}}{p_\infty}\right)_{l=22}$ for $\frac{p_{\beta o}}{p_\infty}=4$ for values of $\frac{a_\infty D}{\nu_\infty}$ of –			Values of $\left(\frac{p_{\beta o}}{p_\infty}\right)-\left(\frac{p_{ss}}{p_\infty}\right)_{l=22}$ for $\frac{p_{\beta o}}{p_\infty}=10$ for values of $\frac{a_\infty D}{\nu_\infty}$ of –			R^*
		0.01×10⁶	0.1×10⁶	1×10⁶	0.01×10⁶	0.1×10⁶	1×10⁶	
$L_{7,1}$	21	1.45	0.48	0.17	2.62	0.66	0.10	∞
$L_{7,7}$	21	2.30	1.45	.91	6.10	3.85	2.43	0
$NL_{7,1}$	21	1.09	.44	.16	1.87	.58	.10	∞
$NL_{7,7}$	21	1.39	1.04	.74	3.22	2.50	1.83	0
$NL_{7,T}$	22	1.09	.99	.73	2.65	2.46	1.8	1.25×10⁶
$NL_{7,T}$	22	1.09	.92	.72	1.87	2.38	1.8	2.5×10⁶

The nonlinear attenuation predictions for values of $R^*=1.25\times10^6$ and 2.5×10^6 are shown in figures 22(a) and 22(b). Since, for these values of R^*, $l^*=0.122$ and 0.244 foot for $\frac{a_\infty D}{\nu_\infty}=10^6$ at $\frac{p_{\beta o}}{p_\infty}=10$, the nonlinear curve for turbulent flow is nearly identical to that for transition and the turbulent curve is used in the figure. These curves and the table indicate that transition at a constant value of R^* appears to decrease further the spread of attenuation with $a_\infty D/\nu_\infty$. The discon-

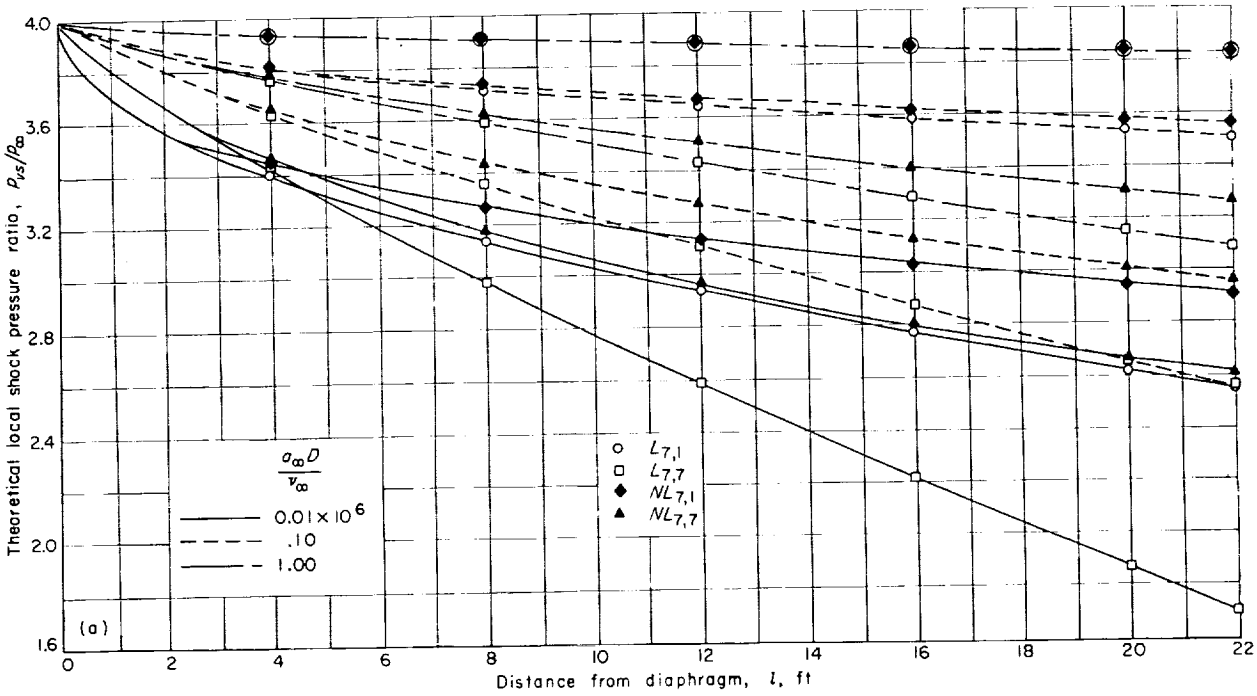

(a) $\frac{p_{\beta o}}{p_\infty}=4.0$.

FIGURE 21.—Theoretically predicted local shock pressure ratios plotted against shock distance from diaphragm.

tinuous change in $d\frac{p_{vs}/p_\infty}{dl}$ at l^* is obvious. Another point of interest is the predicted variation of $NL_{7,7}$ at $l=22$, $p_{\beta o}/p_\infty=10$, and $R^*=2.5\times10^6$; the attenuation is less for $a_\infty D/\nu_\infty$ of 0.01×10^6 and 1×10^6 than it is for $a_\infty D/\nu_\infty$ of 0.1×10^6. The completely laminar flow of $\frac{a_\infty D}{\nu_\infty}=0.01\times10^6$ and the nearly completely turbulent flow of $\frac{a_\infty D}{\nu_\infty}=1\times10^6$ result in almost identical attenuations. The flow of $\frac{a_\infty D}{\nu_\infty}=0.1\times10^6$ is mainly turbulent ($l^*=2.44$) and, as expected, the attenuation is greater than for $\frac{a_\infty D}{\nu_\infty}=1\times10^6$. Thus, in this case, transition has resulted in an inversion of attenuation with Reynolds number under a certain set of conditions. However, for $R^*=1.25\times10^6$, $\frac{p_{\beta o}}{p_\infty}=10$, and $l=22$ feet, the pattern of increasing attenuation with decreasing $a_\infty D/\nu_\infty$ is once again evident.

In figures 23 to 36 the variation of the average experimental shock pressure ratio with distance is compared with the various attenuation predictions of the theory presented earlier in this paper. The nominal values of $p_{\beta o}/p_\infty$ range from 1.5 to 10 and $a_\infty D/\nu_\infty$ covers the range of 0.005×10^6 to 15×10^6. The hydraulic diameter of the shock tube is $\frac{1}{7}$ foot and the maximum value of l at which p_{vs}/p_∞ could be determined was 17$\frac{9}{10}$ feet; thus a maximum experimental value of $\frac{l}{D}\approx125$ resulted.

The marked improvement obtained from use of the nonlinear theory when the predicted attenuation is large becomes evident upon inspection of figures 23 to 36. The unusual behavior near $l\to0$ which was mentioned earlier can now be examined more closely. For the higher values of shock pressure ratio (8, 9, and 10) and low values of $\frac{a_\infty D}{\nu_\infty}\leqq0.01\times10^6$, the measured attenuations at the first station are much smaller than any of the theoretical predictions of this report or of reference 2. In fact, for $\frac{p_{\beta o}}{p_\infty}=9.0$ and $\frac{a_\infty D}{\nu_\infty}=0.005\times10^6$, one set of averages gives a negative attenuation $\left(\frac{p_{vs}}{p_\infty}>\frac{p_{\beta o}}{p_\infty}\right)$ of such size that even the estimated 1-percent-error margin is not sufficient to make

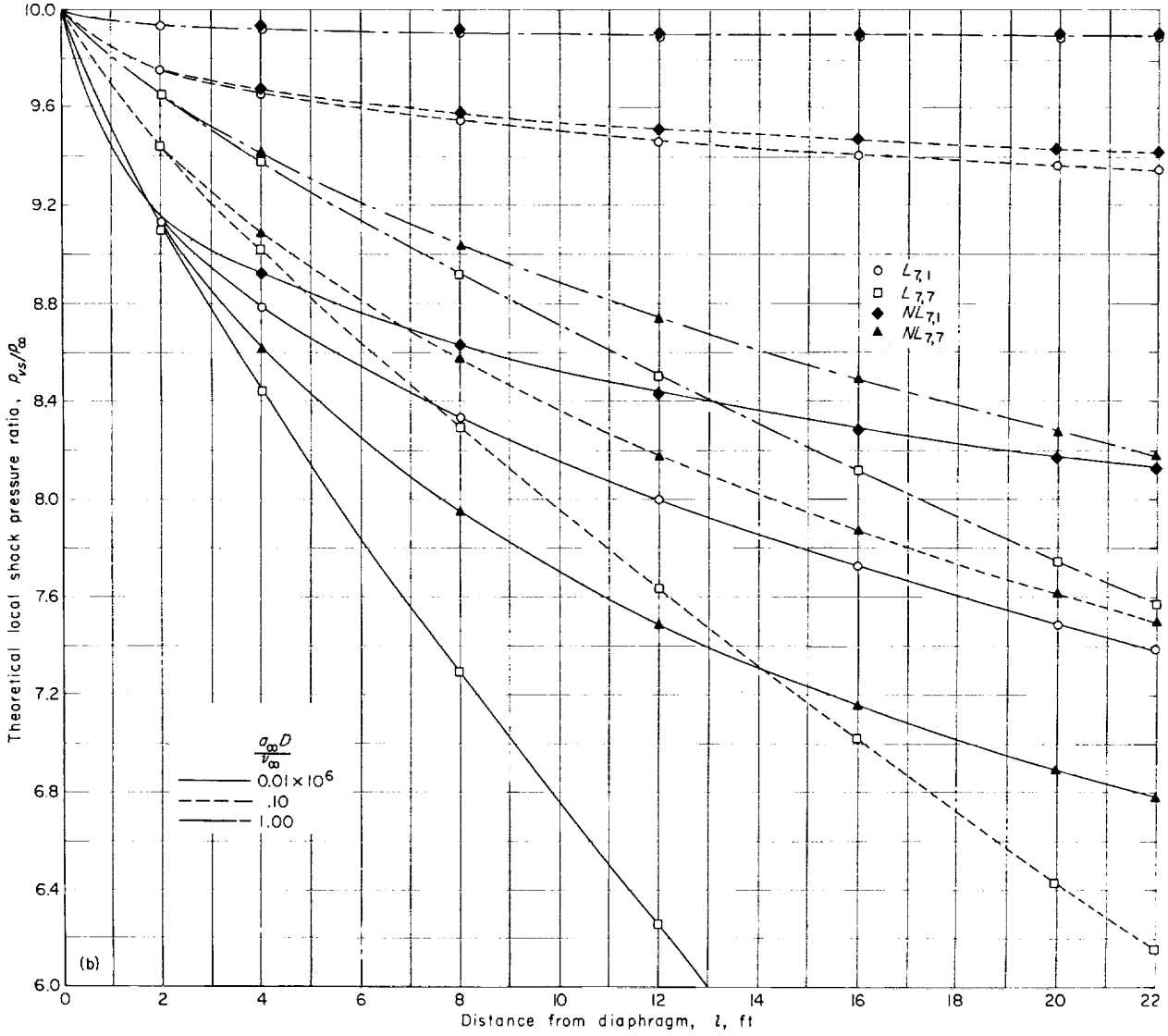

(b) $\frac{p_{\beta o}}{p_\infty}=10.0$.

FIGURE 21.—Concluded.

$\frac{p_{vs}}{p_\infty}<\frac{p_{\beta o}}{p_\infty}$ at the first station $\left(\frac{l}{D}=36.6\right)$. In reference 9 it was also found that for high values of $p_{\beta o}/p_\infty$ the maximum shock velocities were greater than the velocity theoretically computed for an inviscid fluid both with and without consideration of variable specific heat and gaseous imperfections. Hydrogen and helium were used as the driver gas and air as the low-pressure fluid. The maximum shock velocity occurred at about 40 to 50 diameters from the diaphragm.

On the other hand, references 4 and 8 did not find any values of $\frac{p_{vs}}{p_\infty}>\frac{p_{\beta o}}{p_\infty}$ for values of $p_{\beta o}/p_\infty$ in the same range as the present experiments. These works proposed a "formation decrement" defined as "the difference between the Rankine-Hugoniot shock strength and the maximum shock strength obtained after the formation distance." (See ref. 8, page 17.) This decrement was then attributed to the imperfect diaphragm burst producing a series of compression waves which eventually coalesce to form a shock weaker than that for the case of a theoretically perfect burst.

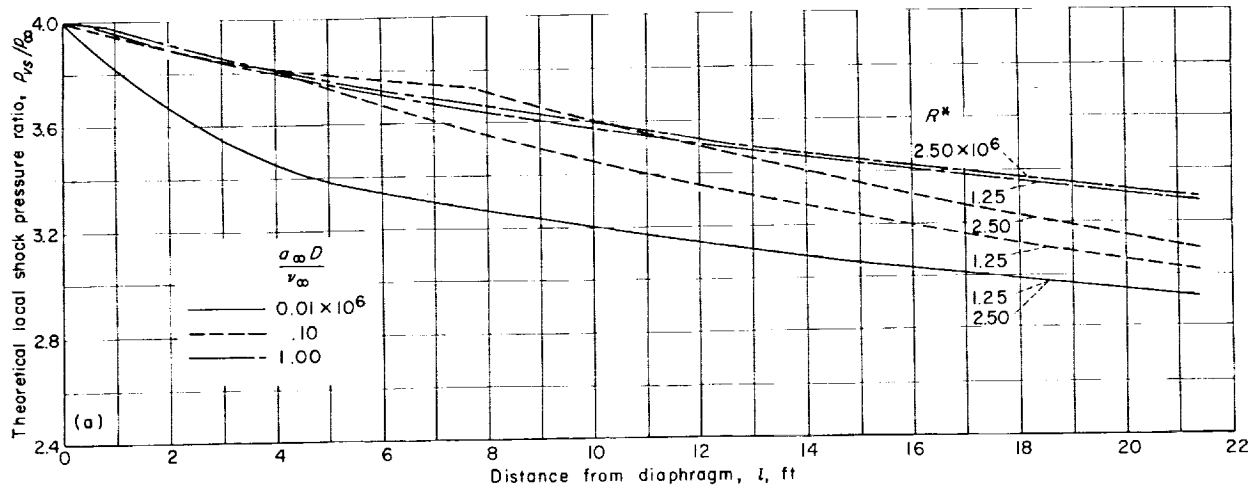

(a) $\frac{p_{\beta o}}{p_\infty}=4.0$.

FIGURE 22.—Nonlinear theoretically predicted shock pressure ratios with transition plotted against shock distance from diaphragm.

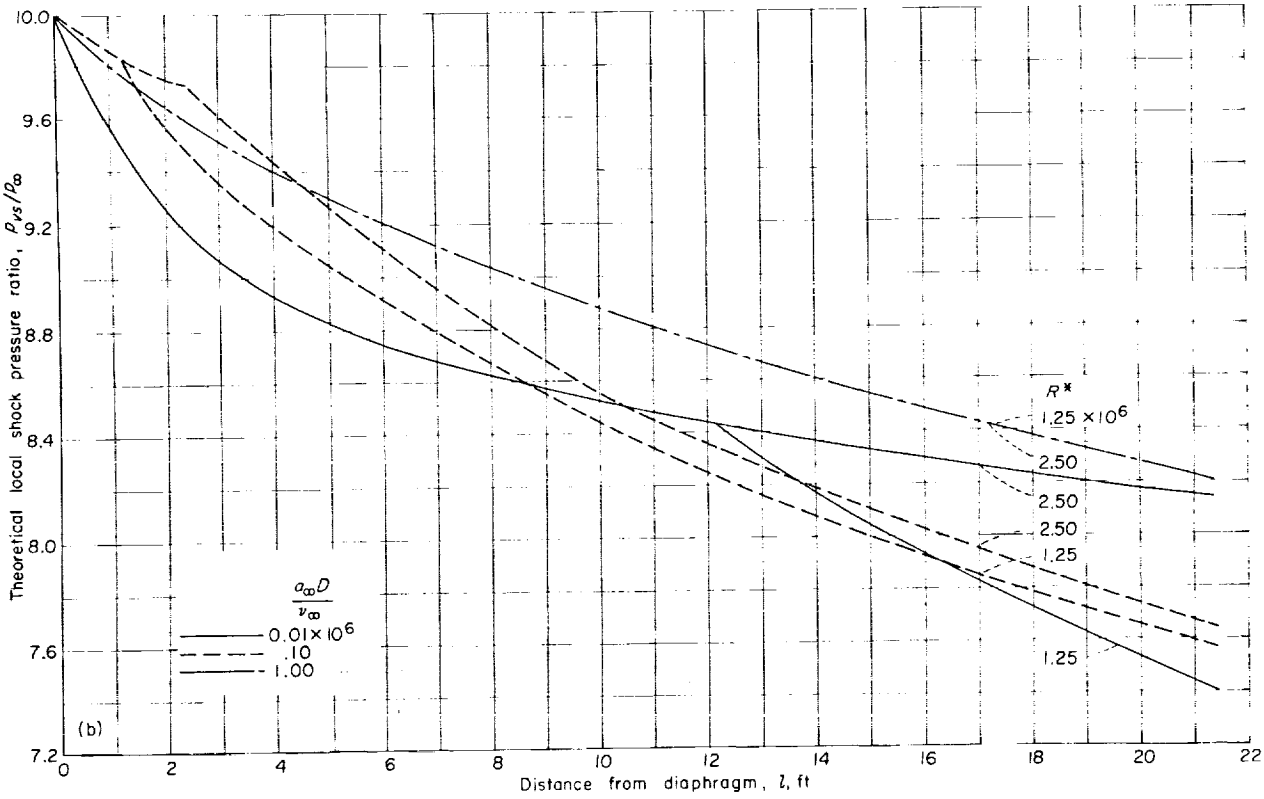

(b) $\frac{p_{\beta o}}{p_\infty}=10.0$.

FIGURE 22.—Concluded.

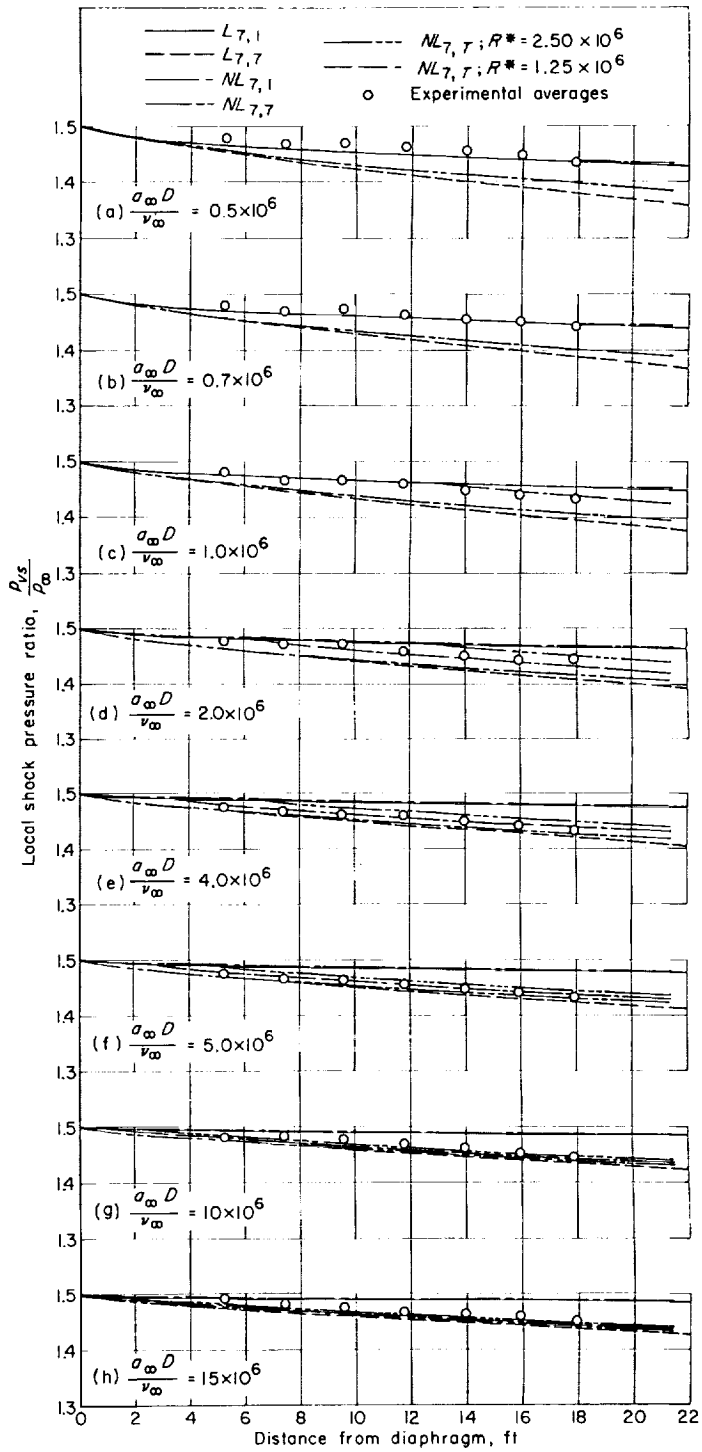

FIGURE 23.—Comparison of averaged experimental local shock pressure ratios with various theoretical predictions. $\frac{p_{\beta_0}}{p_\infty} = 1.5$.

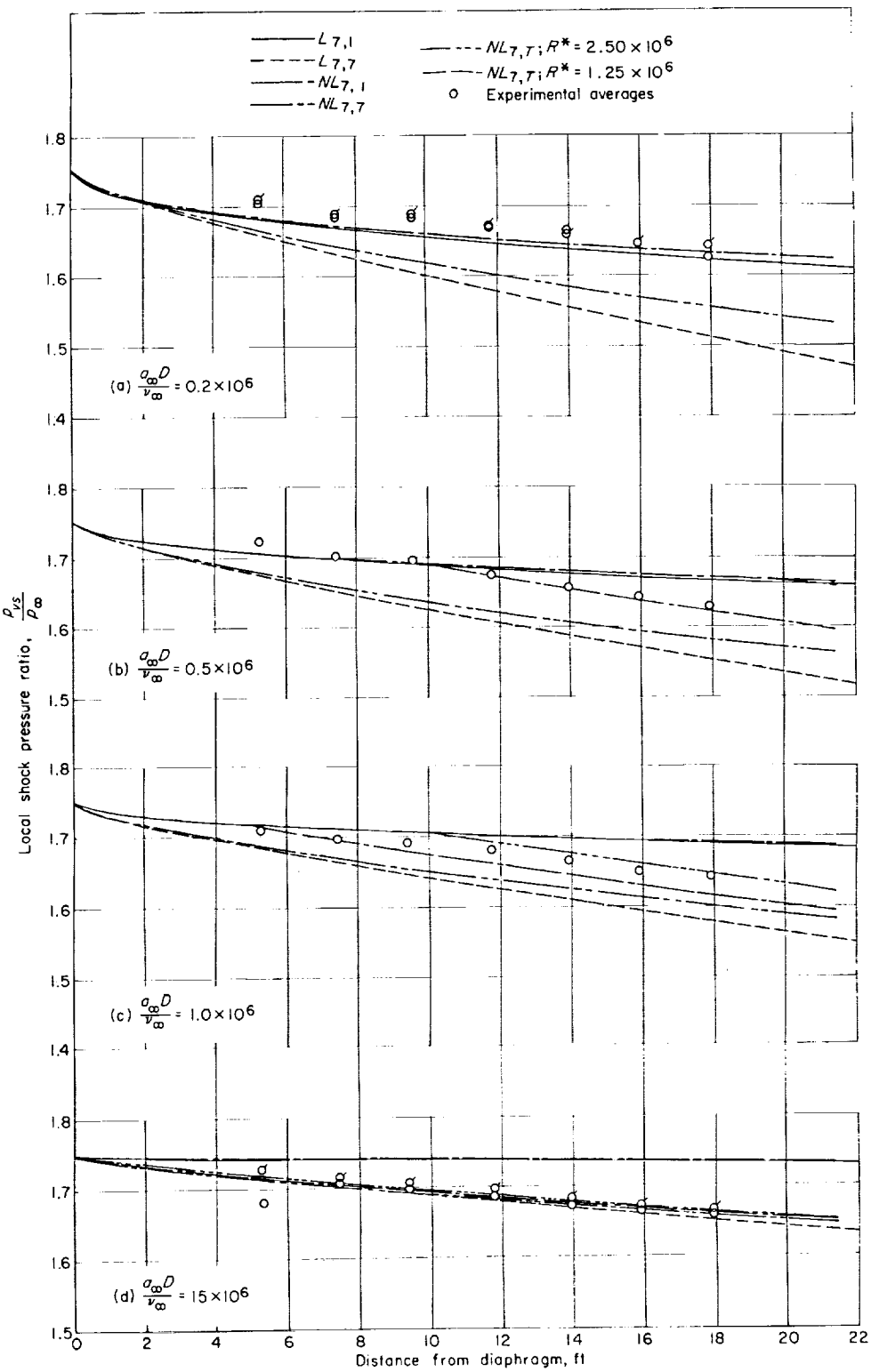

FIGURE 24.—Comparison of averaged experimental local shock pressure ratios with various theoretical predictions. $\frac{p_{s_0}}{p_\infty}=1.75$. Flagged and unflagged symbols are used to distinguish between averages from different days.

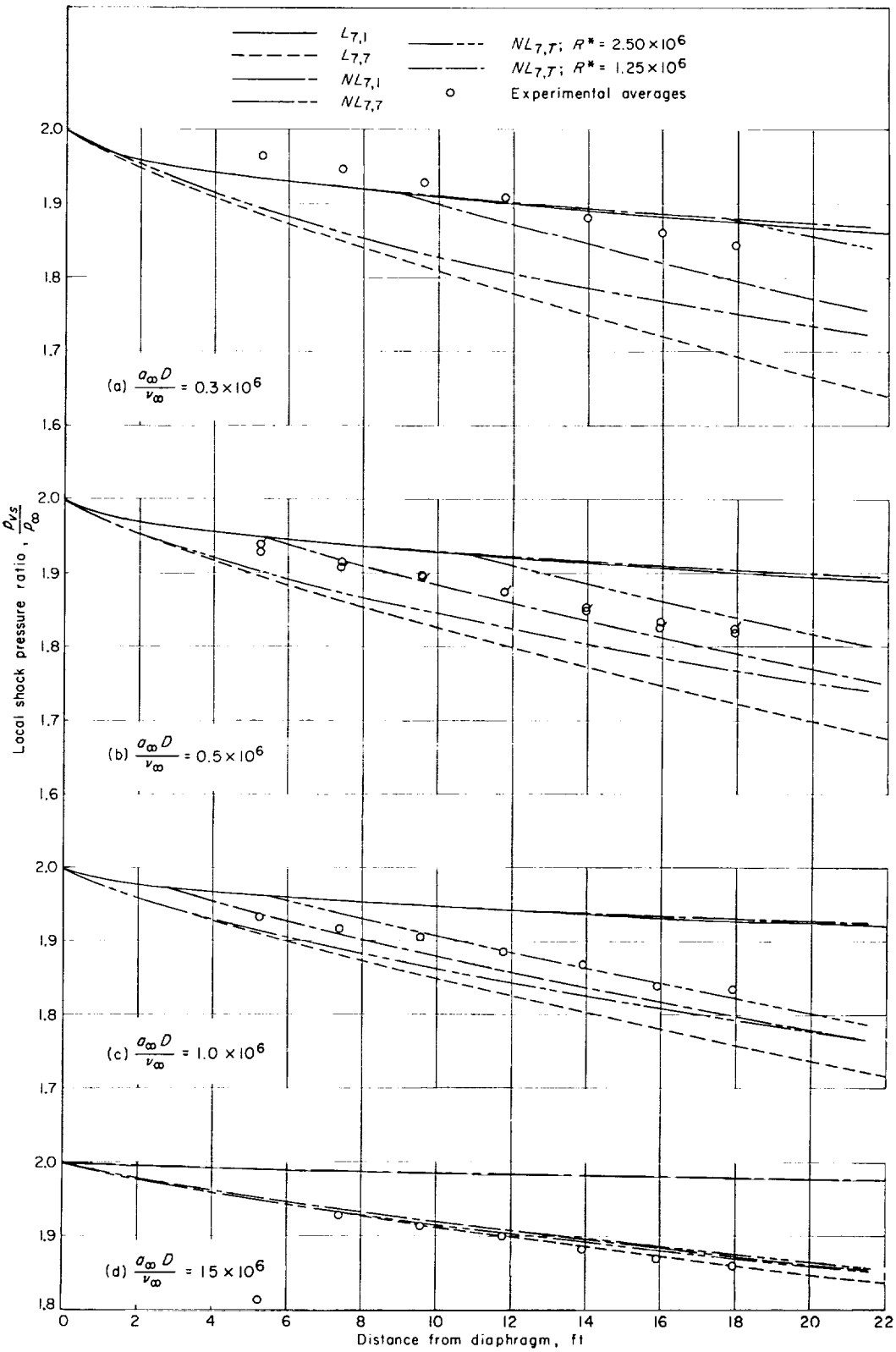

FIGURE 25.—Comparison of averaged experimental local shock pressure ratios with various theoretical predictions. $\frac{p_{s_0}}{p_\infty} = 2.0$. Flagged and unflagged symbols are used to distinguish between averages from different days.

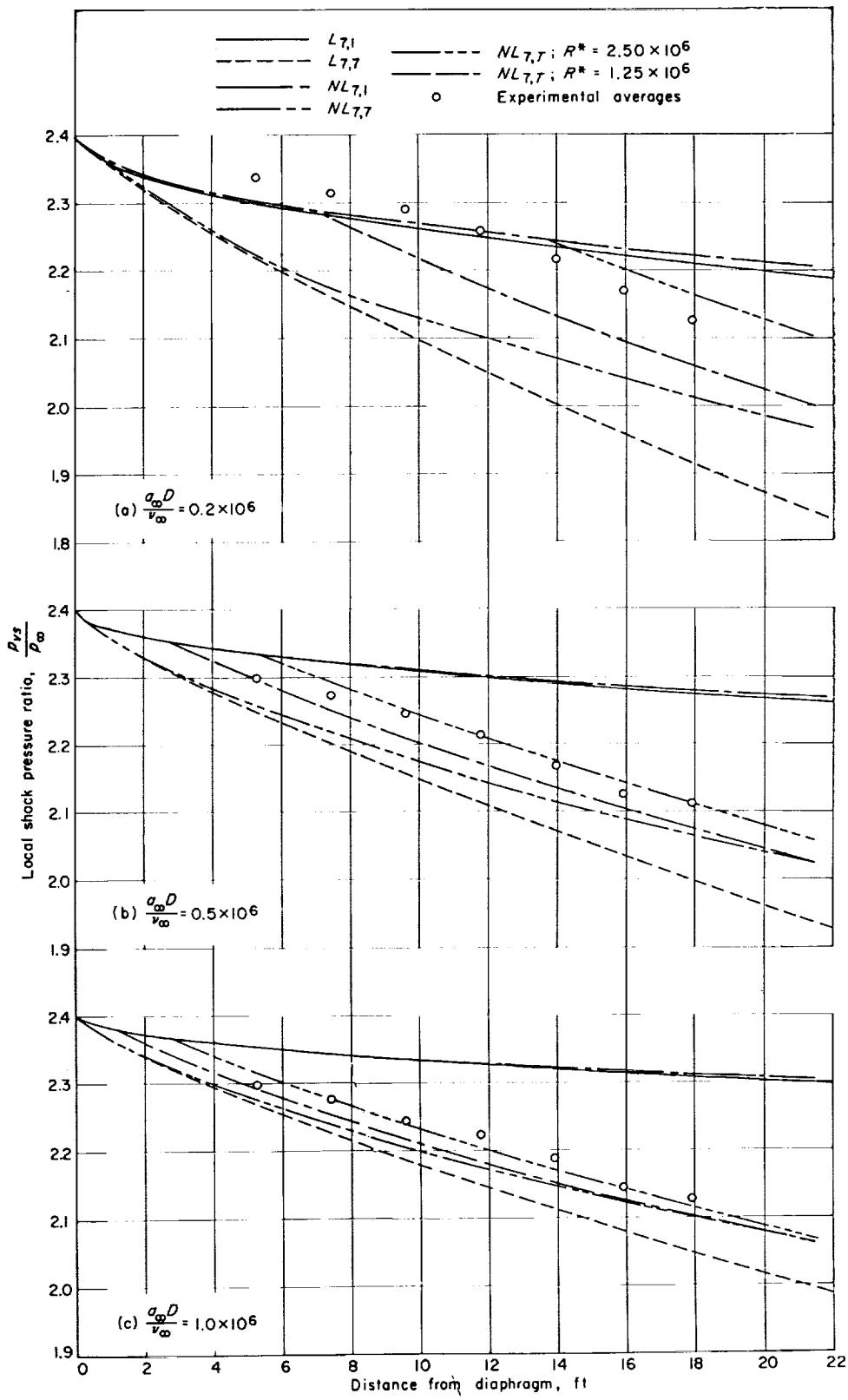

FIGURE 26.—Comparison of averaged experimental local shock pressure ratios with various theoretical predictions. $\frac{p_{Bo}}{p_\infty} = 2.4$.

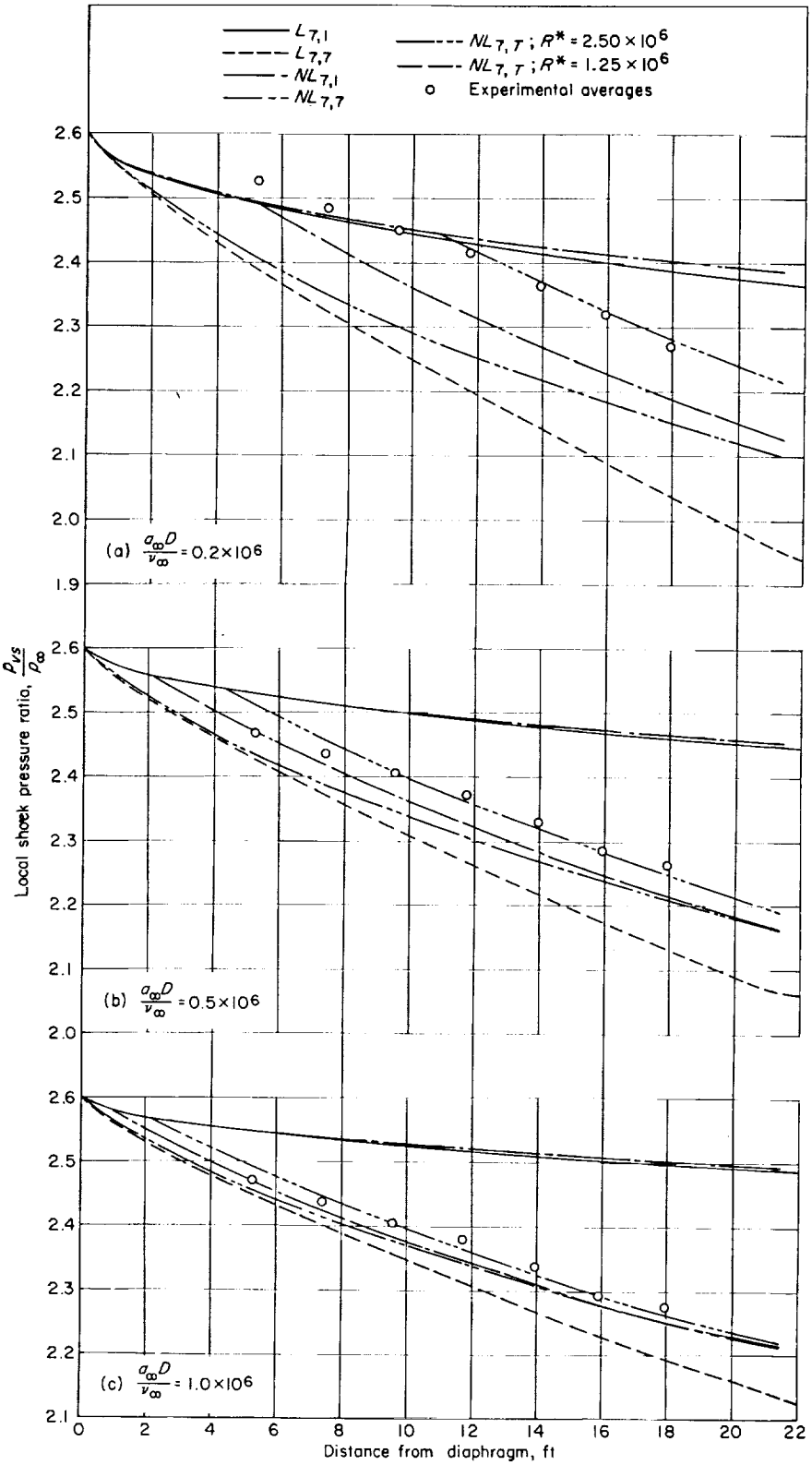

FIGURE 27.—Comparison of averaged experimental local shock pressure ratios with various theoretical predictions. $\frac{p_{\beta_0}}{p_\infty} = 2.6$.

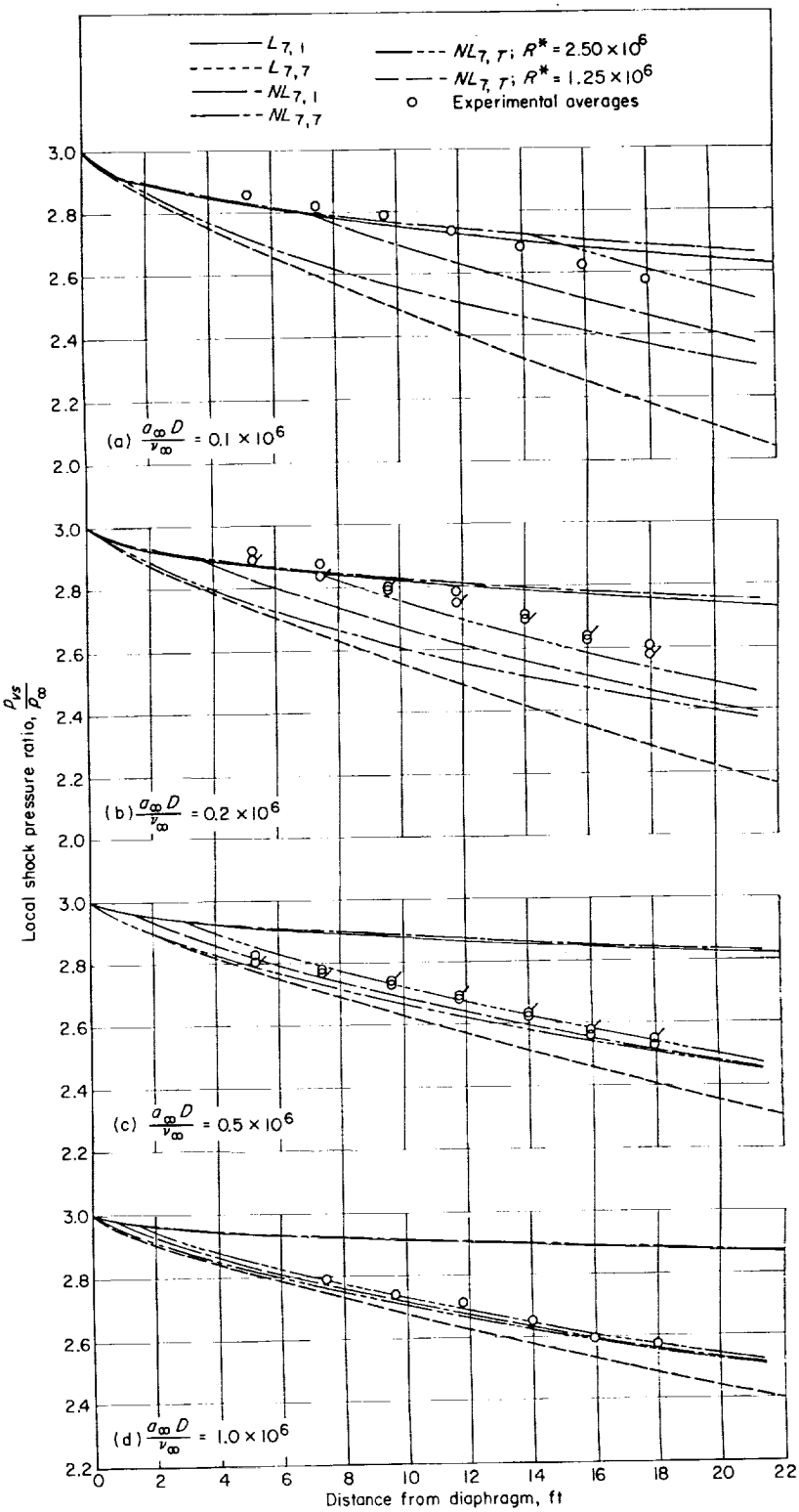

FIGURE 28. Comparison of averaged experimental local shock pressure ratios with various theoretical predictions. $\frac{p_{\beta_0}}{p_\infty}=3.0$. Flagged and unflagged symbols are used to distinguish between averages from different days.

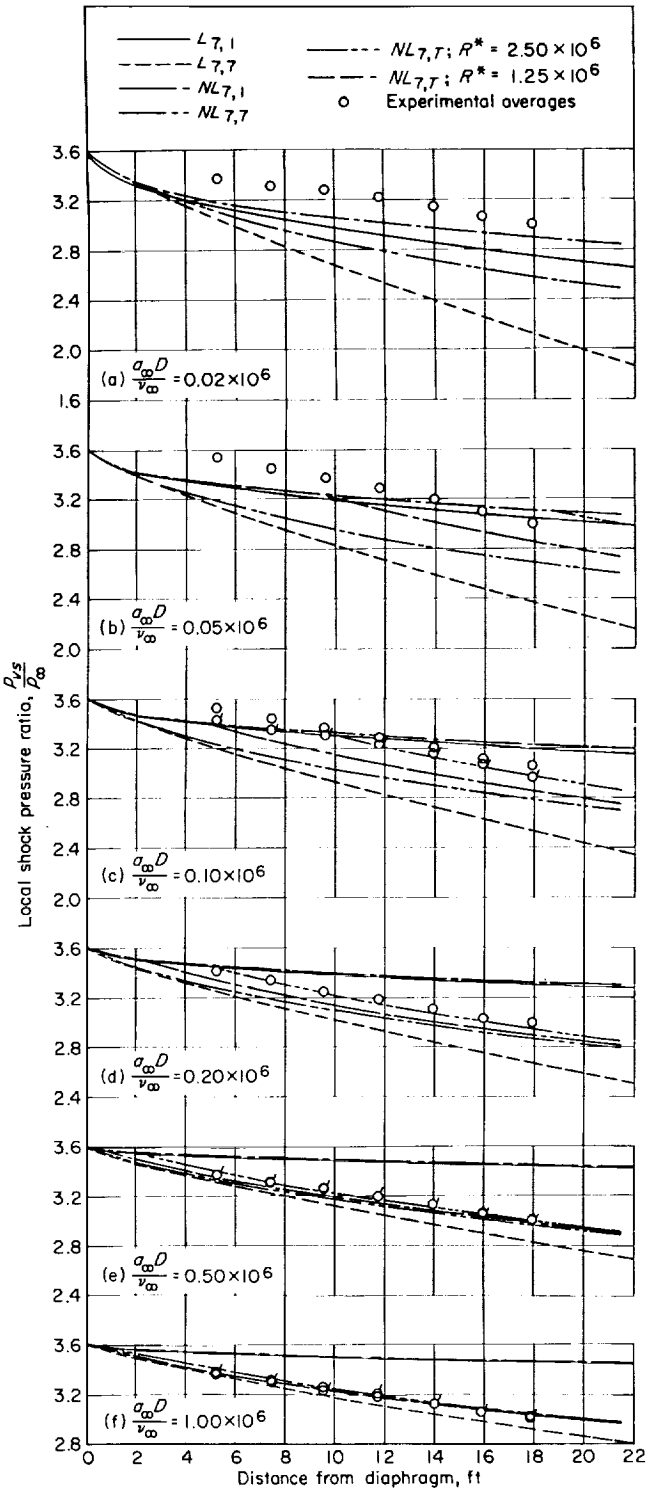

FIGURE 29.—Comparison of averaged experimental local shock pressure ratios with various theoretical predictions. $\frac{p_{\beta_0}}{p_\infty}=3.6$. Flagged and unflagged symbols are used to distinguish between averages from different days.

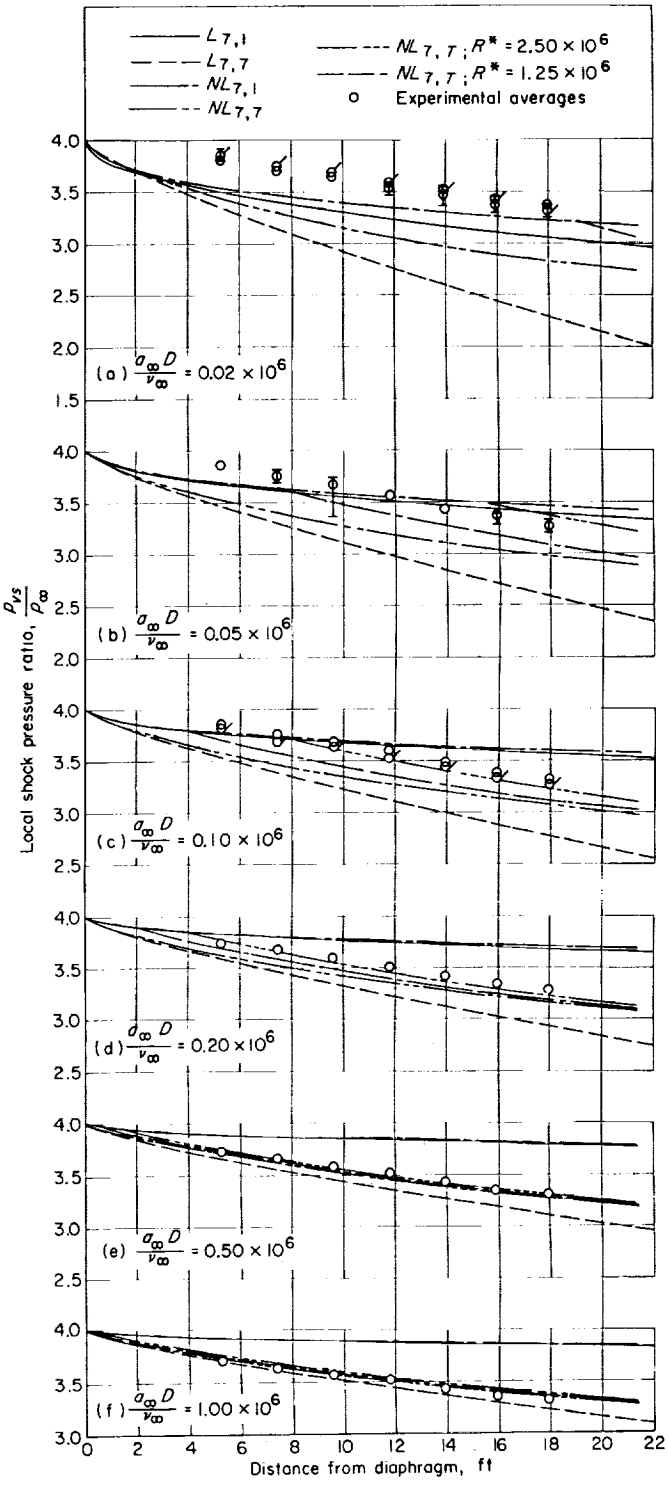

FIGURE 30.—Comparison of averaged experimental local shock pressure ratios with various theoretical predictions. $\frac{p_{\beta 0}}{p_\infty}=4.0$. The vertical lines in (a) and (b) indicate the range of scatter in an averaged group when the scatter exceeds the symbol size. Flagged and unflagged symbols are used to distinguish between averages from different days.

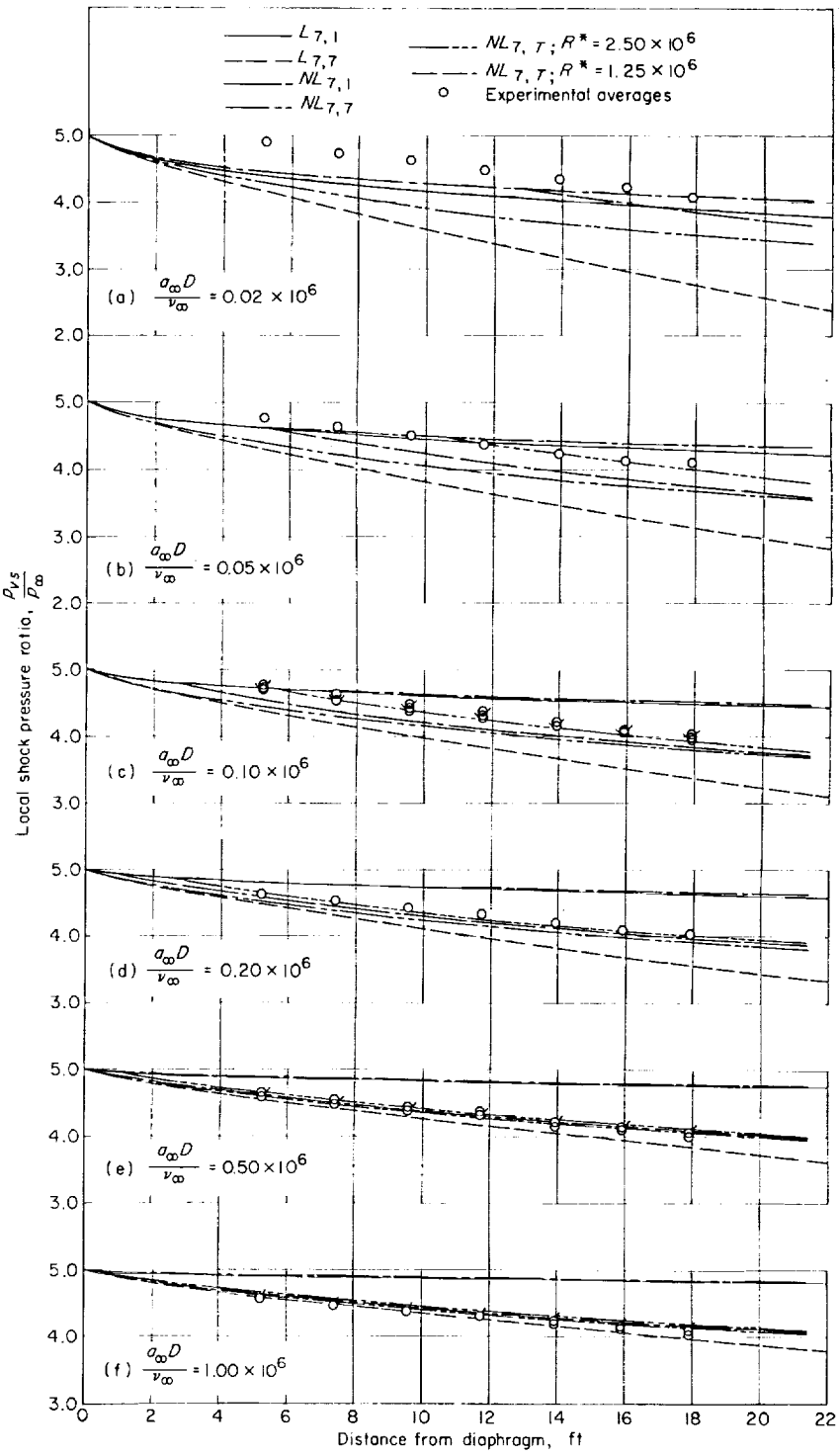

FIGURE 31. Comparison of averaged experimental local shock pressure ratios with various theoretical predictions, $\frac{p_{\beta_0}}{p_\infty}=5.0$. Flagged and unflagged symbols are used to distinguish between averages from different days.

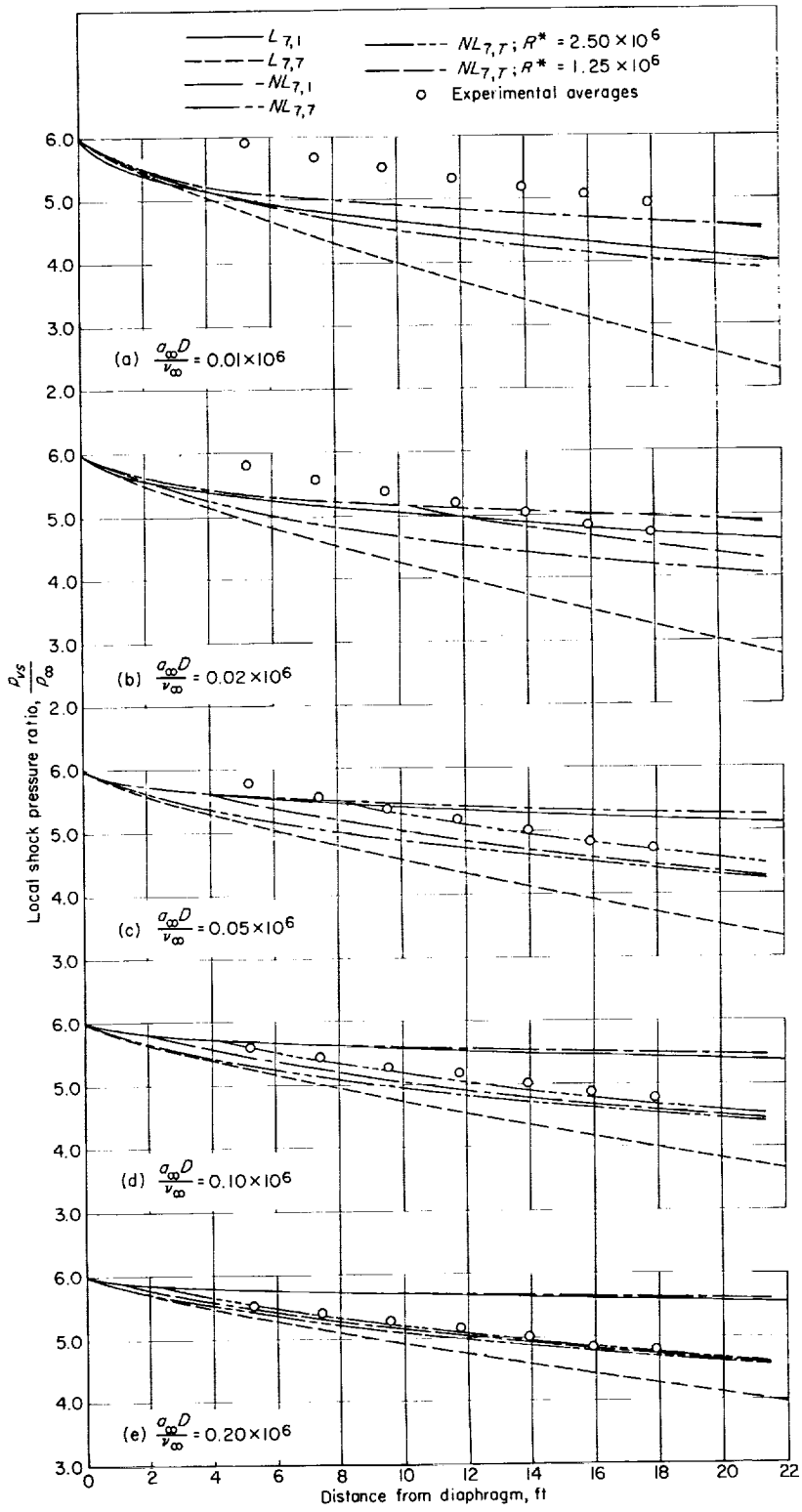

FIGURE 32.—Comparison of averaged experimental local shock pressure ratios with various theoretical predictions. $\frac{p_{s_0}}{p_\infty} = 6.0$.

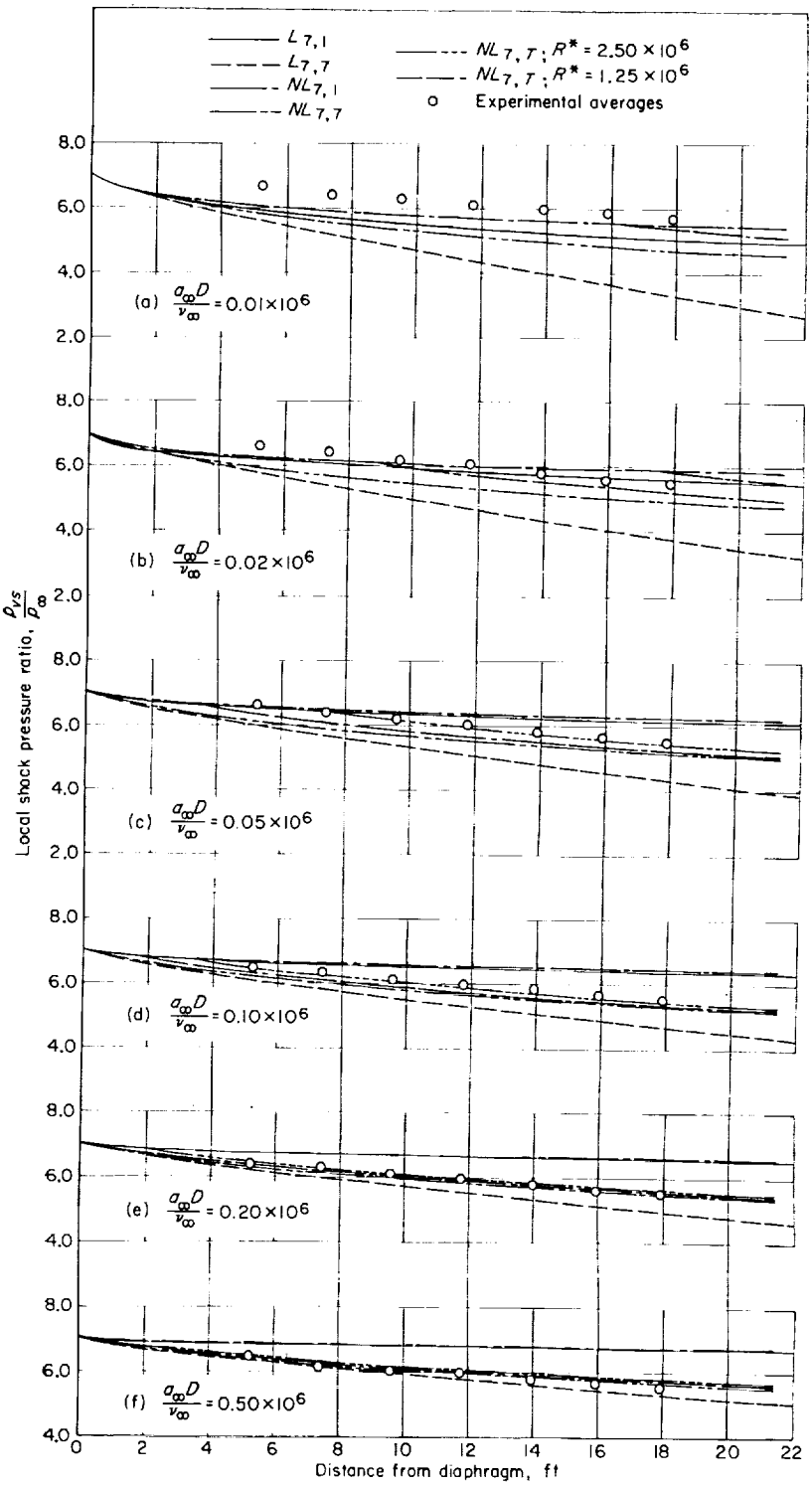

FIGURE 33.—Comparison of averaged experimental local shock pressure ratios with various theoretical predictions. $\frac{p_{\beta_0}}{p_\infty} = 7.0$.

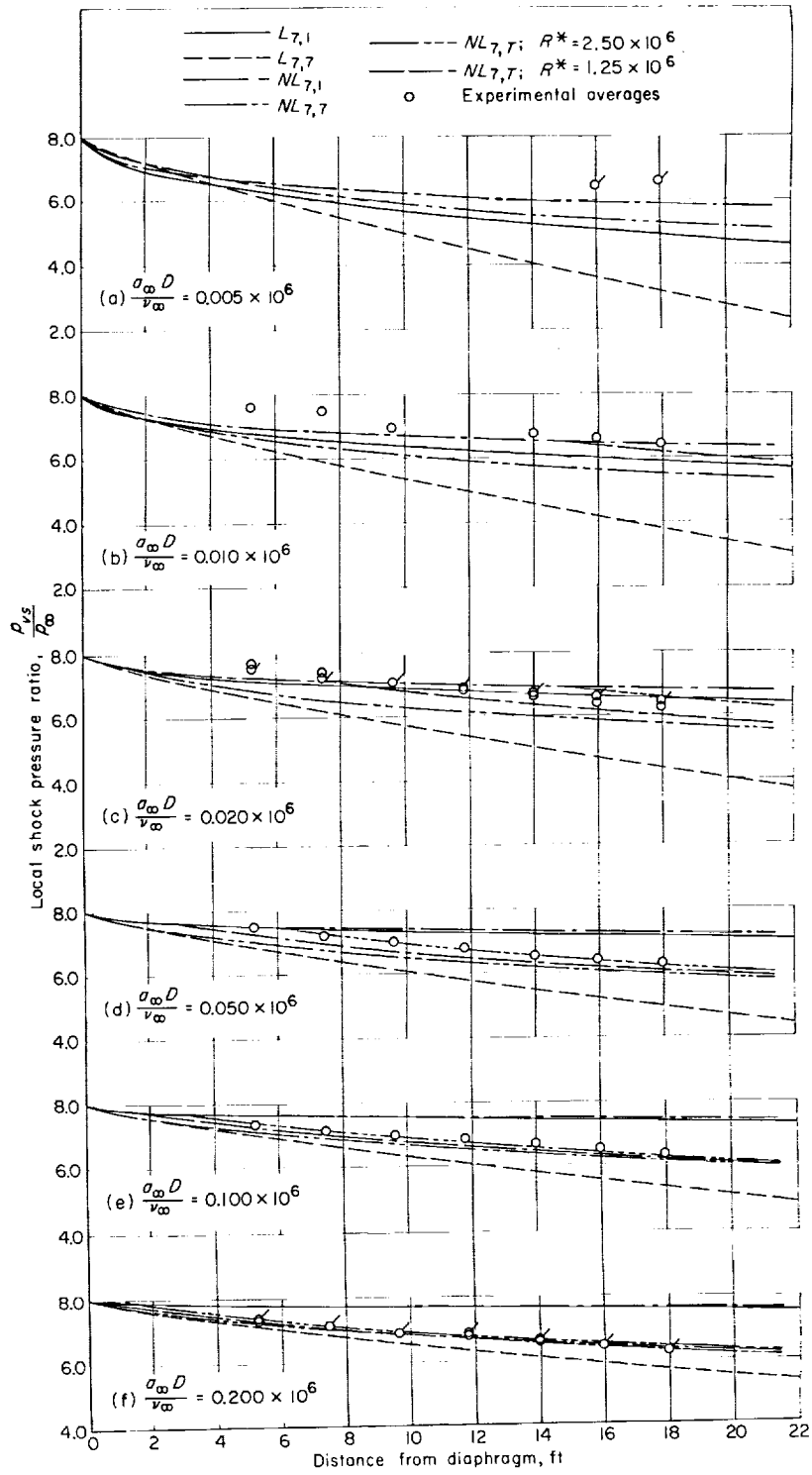

FIGURE 34.—Comparison of averaged experimental local shock pressure ratios with various theoretical predictions. $\frac{p_{s_0}}{p_\infty}=8.0$. Flagged and unflagged symbols are used to distinguish between averages from different days.

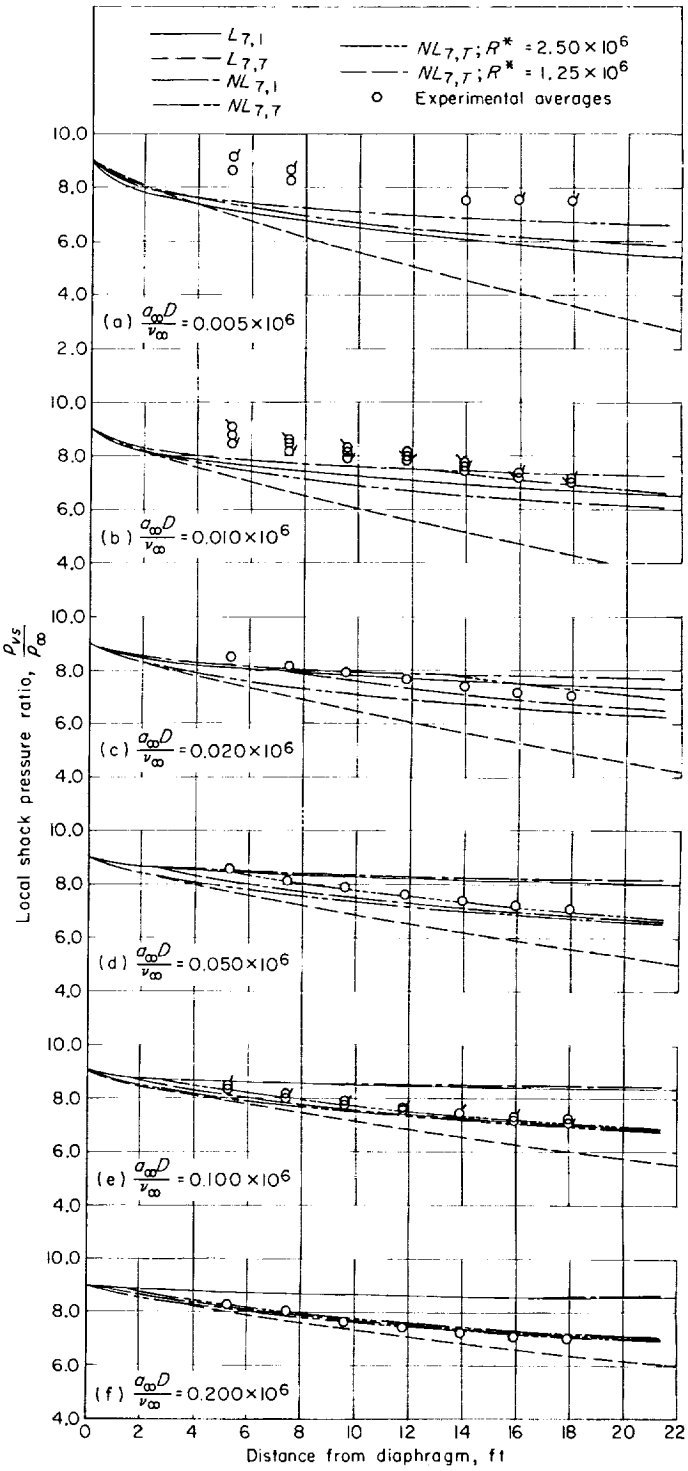

FIGURE 35.—Comparison of averaged experimental local shock pressure ratios with various theoretical predictions. $\frac{p_{s_0}}{p_\infty} = 9.0$. Flagged and unflagged symbols are used to distinguish between averages from different days.

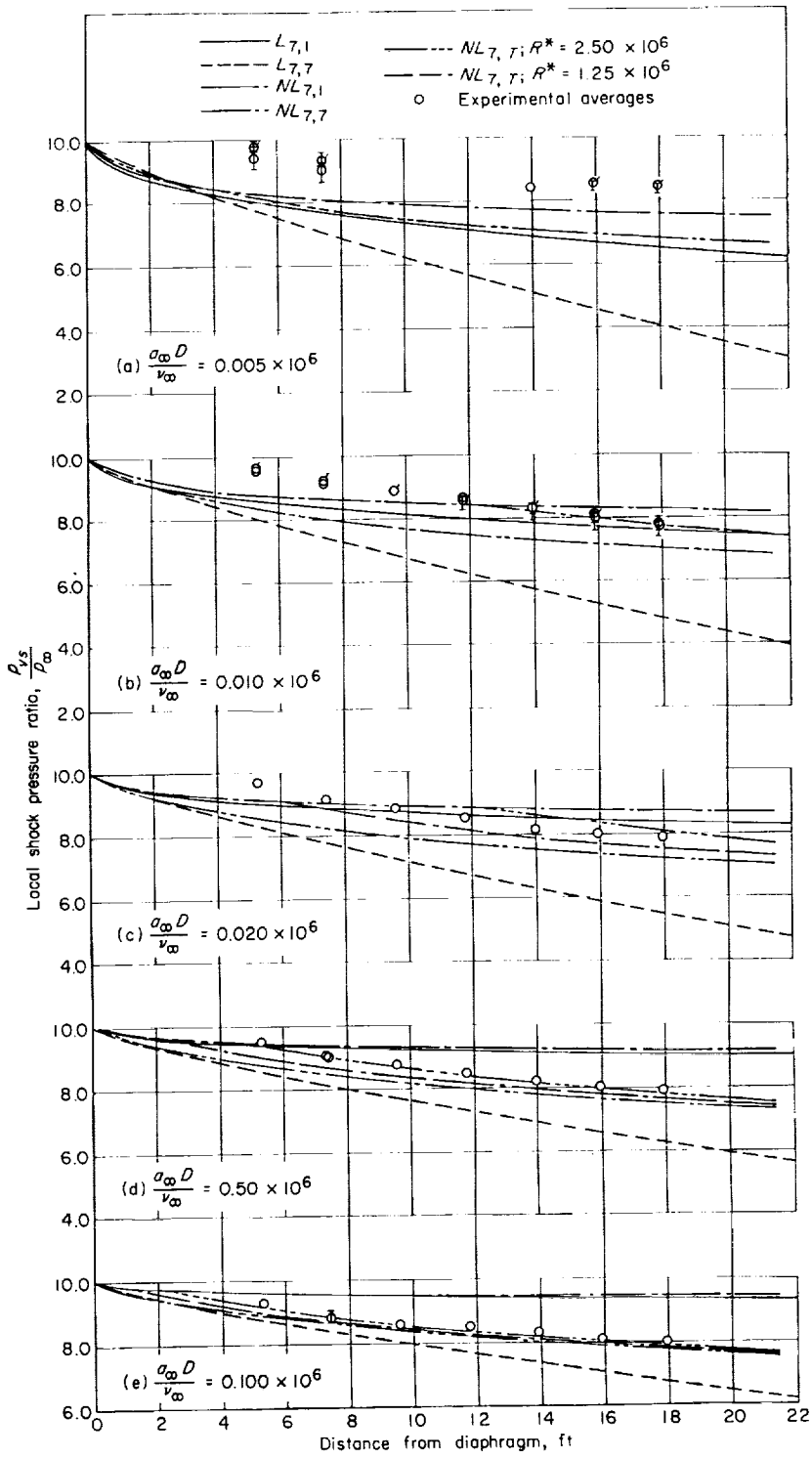

FIGURE 36.—Comparison of averaged experimental local shock pressure ratios with various theoretical predictions. $\frac{p_{\beta_0}}{p_\infty}=10.0$. The vertical lines in (a) and (b) show range of scatter in an averaged group when scatter exceeds symbol size. Flagged and unflagged symbols are used to distinguish between averages from different days.

For the lowest shock pressure ratios at the highest shock tube Reynolds numbers, the opposite trend (measured attenuation larger than theory) is apparent. An extreme example of this is the attenuation measured at the first station for $\frac{a_\infty D}{\nu_\infty}=15\times10^6$ and $\frac{p_{\beta o}}{p_\infty}=2$. (See fig. 25.) Three of the four runs used in obtaining this average value showed this behavior, which is attributed to the formation process.

The processes giving rise to the behavior for $l/D\to0$ are not understood. The experimental data of this report generally show a trend of decreasing $p_{vs}/p_{\beta o}$ with increasing $a_\infty D/\nu_\infty$ at the first station. If this effect were to be explained on a viscous basis, it would appear that an opposite trend would appear; hence, the diaphragm burst is probably the governing factor. The bursting phenomena are in turn governed by the diaphragm materials (weights and rupture characteristics) as well as the pressure load. The diaphragm opening time (time for the diaphragm sectors to fold against the wall) was estimated by a method which has previously been checked experimentally. No correlation was found between the opening time and the behavior near $l\to0$. It was noticed, however, that, in the experimental runs which exhibited the most marked inflections, foil diaphragms were used. On the other hand, some runs exhibiting very little or no inflection also used foil diaphragms. Therefore, it does not appear that foil diaphragms are solely responsible for the inflected data points.

Regardless of whether the maximum experimental value of p_{vs}/p_∞ is greater than or less than the ideal value, the behavior near the diaphragm station is not governed by wall effects but by the diaphragm burst and the resultant three-dimensional flow first established. This highly rotational viscous flow does eventually become essentially two-dimensional, with the exception of mixing and vorticity at the interface between the driver and driven gases. Consequently, any attenuation theory based on wall effects cannot predict the initial behavior near the diaphragm station. As the distance from the diaphragm station increases, the ratio of the influence of the initial bursting flow to the influence of the integrated wall effects decreases; therefore, the physical variation of p_{vs}/p_∞ should approach the theoretically predicted attenuated value asymptotically as l/D increases.

The experimental data of figures 23 to 36 approach the nonlinear theory (considering transition) in a manner very similar to that just described. For high values of $p_{\beta o}/p_\infty$ and low values of $a_\infty D/\nu_\infty$ where the effect of the formation process results in a significant inflection, the deviation from the nonlinear curve persists to the larger values of l/D. For $\frac{p_{\beta o}}{p_\infty}=10$, 9, and 8 with $\frac{a_\infty D}{\nu_\infty}=0.005\times10^6$, the formation effect was so large that the experimental data never approached closely the nonlinear curve for $\frac{l}{D}\leqq125$. As $a_\infty D/\nu_\infty$ increased and the formation effect decreased, agreement between experiment and nonlinear theory improved both in convergence of the experimental and theoretical values at a lower value of l/D and in maximum deviation at the highest values of l/D.

The nonlinear curve for $R^*=2.5\times10^6$ appears to agree more favorably with the data over most of the range of $p_{\beta o}/p_\infty$. At the lower values of $p_{\beta o}/p_\infty$ there appears to be a tendency for the data to depart from the $R^*=2.5\times10^6$ curve and approach the $R^*=1.25\times10^6$ curve. The interferometric measurements of reference 16 indicate such a trend of increasing R^* with increasing $p_{\beta o}/p_\infty$. This trend might also be expected from comparison with steady-flow experiments since the wall cooling increases as $p_{\beta o}/p_\infty$ increases.

The comparisons of figures 23 to 36 between the nonlinear transitional theory and the experimental data show that this theory is valid for the prediction of experimental attenuation except for the lower shock tube Reynolds numbers at the higher pressure ratios. These latter conditions are those under which it appears that the shock-formation processes dominate the entire flow.

As stated previously, errors of unknown magnitude were introduced by the averaging of wall effects across the flow. The fact that the present theory was able to predict fairly well the measured attenuations over the entire range of shock pressure ratios and Reynolds numbers (except near the diaphragm) indicates that the errors introduced in the averaging process are either not serious or else self-compensating.

The range of boundary-layer thicknesses in region β (which has the predominant influence on attenuation) was determined by methods similar

to those of references 14 and 15 for laminar and turbulent flows, respectively. In the experiments reported herein, with the shock 20 feet from the diaphragm, the maximum boundary-layer thickness varied approximately from 0.006 to 0.25 inch for laminar flow and from 0.07 to 1 inch for turbulent flow. When compared with the 0.75-inch half-width of the shock tube, the turbulent thickness was significant for much of the experimental data. On the other hand, laminar boundary-layer thickness was generally small. Thus the averaging process as used for this theory appears to apply equally well to thick as well as to thin boundary layers.

MAGNITUDE OF OTHER NEGLECTED SECOND-ORDER EFFECTS

Since the treatment presented has considered only one source of nonlinearity, it is advisable to examine briefly the influence of other neglected sources. The three most obvious factors neglected are the finite extent of the expansion fan, the nonlinear effect of the wave interactions at the entropy discontinuity, and the reflections at the shock wave.

The effect upon attenuation of treating the expansion wave as one of finite width with varying free-stream properties was calculated by using the results of reference 14 for pressure ratios $p_{\beta o}/p_\infty$ of 1.6, 2.9, and 4.5 (ξ_{te} of -0.6, 0, and 0.5, respectively, in the notation of ref. 14). Computations were not made for higher shock pressure ratios because the solutions in reference 14 did not extend above $\xi_{te}=0.6$. The laminar-flow wall-shear and heat-transfer distributions through the cold-gas regions given by this reference were used to compute the skin-friction coefficient which was, in turn, utilized to compute the attenuation.

When the method of the present paper was used, it was found that, for the three cases computed, the net change in attenuation through approximation of the finite expansion by the negative shock was practically zero for $p_{\beta o}/p_\infty$ equal to 1.6, -0.3 percent for $p_{\beta o}/p_\infty$ equal to 2.9, and -0.6 percent for $p_{\beta o}/p_\infty$ equal to 4.5. Although the contribution of the cold gas was itself influenced by the finite expansion (up to a 50-percent decrease at the highest pressure ratio), the cold gas contributes so little to laminar-flow attenuation at these low pressure ratios that the error in assuming a negative shock is negligible.

For higher shock pressure ratios the effect of the finite expansion cannot be computed. However, examination of figure 5 indicates that, at a shock pressure ratio approximately equal to 6, the contribution of the cold gas (with the negative shock) vanishes. At higher pressure ratios the cold gas tends to decrease attenuation, but this effect remains small compared with the contribution of the hot gas. At a shock pressure ratio of 20, for example, the effect of the cold-gas region has reached only 4 percent of the total. Thus, the finite expansion fan can influence only a small part of the total attenuation, and the assumption of a negative shock should give reasonably accurate results.

The laminar boundary-layer finite-expansion-fan solutions of reference 14 were also used to estimate the effect of the negative shock assumption upon the attenuation predicted by reference 2 for the same three pressure ratios. The errors in attenuation which arise through the use of a negative shock are 1.4 percent at $p_{\beta o}/p_\infty$ equal to 1.6, 5.1 percent at $p_{\beta o}/p_\infty$ of 2.9, and 4.2 percent at $p_{\beta o}/p_\infty$ of 4.5. In this case, the contribution of the cold gas tends to decrease the attenuation at all pressure ratios of interest, the contribution for the negative shock assumption reaching a maximum at $p_{\beta o}/p_\infty$ equal to 4.5.

No means of computing turbulent boundary-layer flow inside a finite expansion are available. However, according to the linearized negative shock approach of this paper, the cold-gas contribution is always less than 16 percent for pressure ratios up to 20 and always less than 10 percent for pressure ratios up to 10. (See fig. 5.) If the effect of the finite expansion in turbulent flow is in the same direction as in laminar flow, the cold-gas contribution, when a finite expansion fan is considered, would be less than that for a negative shock. Thus it is assumed that the effects of the difference between the finite-expansion and negative-shock solutions for turbulent flow may be neglected, at least up to shock pressure ratios of 10.

The influence of nonlinearities in the reflection and transmission of waves at the entropy discontinuity was calculated for shock pressure ratios $p_{\beta o}/p_\infty$ equal to 1.25, 2.0, 4.0, 6.0, 8.0, and 10.0. The nonlinearities involved required that the shock-tube Reynolds number and station be specified in order to calculate the attenuation

for this case. The case of $a_\infty D/\nu_\infty$ equal to 0.1×10^6 was chosen, and the attenuations at l/D equal to 70 and 140 were calculated for completely laminar ($n=1$) flow and completely turbulent ($n=7$) flow.

For the laminar case, a difference of about one-half percent was found between linear and nonlinear calculations for the wave interactions at the entropy discontinuity for $p_{\beta o}/p_\infty$ of 10 and at l/D equal to 140, the nonlinear calculation predicting greater attenuation. Differences at l/D of 70 and at lower pressure ratios were smaller and generally in the same direction, except at a value of $p_{\beta o}/p_\infty$ of 1.25 where the nonlinear entropy result gave slightly less attenuation than the linear result. The deviations, which were small in all cases, were also somewhat erratic in their behavior.

Differences in the turbulent case were somewhat larger and ranged up to 10 percent for a value of l/D of 140 and a value of $p_{\beta o}/p_\infty$ of 10. This condition is attributed to the larger relative contribution of the cold-gas region α to the total attenuation for turbulent flow. (See table I and fig. 5.) Again, the nonlinear entropy calculation predicted greater attenuation than the linearized except at a value of $p_{\beta o}/p_\infty$ of 1.25 where the trend was reversed. However, at the low pressure ratios the deviation was less than 1 percent and this trend is not considered to be significant.

The effect of reflection of waves at the shock was estimated by the following treatment: The unattenuated shock was assumed to be overtaken by a single isentropic wave of strength equal to the total attenuation for a given condition and station. The resulting one-dimensional interaction was computed and the strength of the shock after interaction compared with the strength predicted by the linearized theory. These results were computed for shock pressure ratios of 10 and 4.

For $p_{\beta o}/p_\infty$ equal to 10, the three cases were compared and the results are given in the following table:

$\frac{a_\infty D}{\nu_\infty}$	$\frac{l}{D}$	Attenuation		Percent difference in attenuation
		No reflection	With reflection	
0.1×10^6	140	$L_{1,1}=-0.60$	$L_{1,1}=-0.55$	8
.1	140	$L_{7,7}=-3.57$	$L_{7,7}=-3.16$	11
.005	154	$L_{7,7}=-7.0$	$L_{7,7}=-6.14$	12

The conditions of $\frac{a_\infty D}{\nu_\infty}=0.005\times10^6$ and $\frac{l}{D}=154$ represent the conditions under which maximum attenuation would be expected for the experimental range of this paper.

In all cases, the shock is slightly strengthened by the interaction, that is, attenuation is decreased. This is a trend which is opposite to that generally computed for the exact entropy discontinuity. For $p_{\beta o}/p_\infty$ equal to 4, only one case was computed, that corresponding to the largest predicted attenuation, $a_\infty D/\nu_\infty$ equal to 0.02×10^6, l/D equal to 154. In this case, the predicted attenuation was $\frac{p_{vs}-p_{\beta o}}{p_\infty}$ equal to -2. The consideration of reflection gave $\frac{p_{vs}-p_{\beta o}}{p_\infty}$ equal to -1.8. The difference in attenuation was 10 percent, again in the direction of decreasing attenuation.

In general, then, the effects of the entropy discontinuity and the reflected wave at the shock which were neglected in the linearized theory tend to oppose one another and are of about the same order of magnitude for the worst cases (turbulent flow, strong shocks).

For the pressure range of this report it has been shown in the preceding discussion that the two nonlinear effects having the largest magnitude are of opposite sign. The effect of neglecting the finite expansion-fan width is small for laminar flow and is also presumed to be small for turbulent flow. Consequently, the neglect of these three effects, which have a net influence much smaller than the nonlinear $\hat{P}$ effect considered, appears to be justified for attenuation. Although the aforementioned effects are negligible for attenuation, they can appreciably influence the pressure, density, and velocity distribution at points removed from the shock. This behavior arises from the fact that the relative influence of the $\hat{P}$ waves of region β decreases as the distance behind the shock increases; the influence reduces to zero at and behind the entropy discontinuity. (See pages 33 and 34 and fig. 13 of ref. 1 for further discussion.)

CONCLUDING REMARKS

The theory of NACA Technical Note 3375, in which shock-wave attenuation is calculated by use of a linearized form of the hyperbolic system

of equations of motion and energy and through the assumption of equivalent incompressible steady-flow friction and heat-transfer coefficients, has been modified in the following manner:

(1) Incompressible unsteady skin-friction coefficients have been determined by an integral method. The resulting unsteady incompressible skin-friction coefficient is corrected for compressibility by a reference temperature method.

(2) A nonlinear regional approach has been employed to permit the extensions of the theory to large attenuations. This approach modifies only the forward running waves generated in the hot-gas region; these waves are shown to dominate the attenuation process.

(3) Transition effects are considered. The method assumes instantaneous transition from laminar to turbulent flow. The Reynolds number of transition then becomes a parameter of the attenuation problem.

The modified theory has been evaluated for a range of shock pressure ratios of general experimental interest. Curves are presented to permit easy prediction of attenuation for shock pressure ratios to 20 and a range of shock-tube Reynolds numbers. Results for the linearized theory with all laminar and all turbulent flow are compared with results of NACA Technical Note 3278, and the predicted attenuations are found to be in fair agreement.

Experimental local shock pressure ratios have been determined for ideal shock pressure ratios from 1.5 to 10 for a range of shock-tube Reynolds numbers and position from the diaphragm station.

Comparison of the modified nonlinear theory using a transition Reynolds number based on flow length of 2.5×10^6 with the experimental results shows good agreement except for the following situations:

(1) The highest shock pressure ratios at the lowest shock-tube Reynolds numbers where the effects of the nonperfect diaphragm burst are believed to dominate the flow.

(2) The lowest shock pressure ratios, for which a lower transition Reynolds number (1.25×10^6) appears to give better agreement.

The effects of considering a finite expansion fan, the exact interaction at the entropy discontinuity, and reflection at the shock wave (all of which are neglected in the present treatment) are calculated for certain cases. The net effect of these three contributions is shown to be small compared with the nonlinearities accounted for in the stepwise regional calculation.

LANGLEY RESEARCH CENTER,
NATIONAL AERONAUTICS AND SPACE ADMINISTRATION,
LANGLEY FIELD, VA., *June 25, 1958.*

APPENDIX A

SUMMARY OF LINEARIZED ATTENUATION EQUATIONS

The changes in the characteristic parameters P, Q, and S/R as a function of local skin friction are derived in reference 1 and those appropriate to shock-wave attenuation are summarized in this appendix. Subscripts refer to positions on the wave diagram of figure 1.

$$\frac{P_c-P_b}{a_\epsilon}=\frac{P_c-P_{\alpha 0}}{a_\epsilon}=\phi_{P,\alpha}\frac{M_\alpha+\eta}{M_\alpha+\eta+1}\frac{1}{D}\int_0^{\xi_d}c_{f,\alpha}(\xi)\,d\xi \tag{A1}$$

$$\frac{P_{vs}-P_f}{a_\epsilon}=\phi_{P,\beta}\frac{\sigma M_s-M_\beta}{\sigma M_s-M_\beta-1}\frac{1}{D}\int_{\xi_f}^{0}c_{f,\beta}(\xi)\,d\xi \tag{A2}$$

$$\frac{Q_f-Q_0}{a_\epsilon}=\frac{Q_f-Q_{3v}}{a_\epsilon}=\phi_{Q,\beta}\frac{\sigma M_s-M_\beta}{\sigma M_s-M_\beta+1}\frac{1}{D}\int_0^{\xi_f}c_{f,\beta}(\xi)\,d\xi \tag{A3}$$

$$\frac{P_f-P_c}{P_{\beta 0}-P_{\alpha 0}}=1+\frac{(P_c-P_b)+(Q_f-Q_0)}{P_{\alpha 0}+Q_{\beta 0}}+\frac{\gamma-1}{\gamma}\frac{a_{\beta 0}/a_{\alpha 0}}{\left(\frac{a_{\beta 0}}{a_{\alpha 0}}\right)^2-1}\left[\phi_{S,\beta}\frac{1}{D}\int_0^{\xi_d}c_{f,\beta}(\xi)d\xi-\phi_{S,\alpha}\frac{1}{D}\int_0^{\xi_d}c_{f,\alpha}(\xi)d(\xi)\right] \tag{A4}$$

where

$$\phi_{P,\alpha}=\frac{2}{\eta}\left\{[(\gamma-1)M_\alpha-1]M_\alpha+\frac{M_\alpha+\eta+1}{M_\alpha+\eta}M_\alpha^2+\frac{(T_w-T_{aw})_\alpha}{T_\alpha}N_{Pr}^{-2/3}\left[1+\frac{M_\alpha+\eta+1}{(M_\alpha+\eta)(\gamma-1)}\right]\right\} \tag{A5}$$

$$\begin{pmatrix}\phi_{P,\beta}\\ \phi_{Q,\beta}\end{pmatrix}=2\frac{a_\beta}{a_\epsilon}\left\{[(\gamma-1)M_\beta\mp 1]M_\beta+\frac{\sigma M_s-M_\beta\mp 1}{\sigma M_s-M_\beta}M_\beta^2+\frac{(T_w-T_{aw})_\beta}{T_\beta}N_{Pr}^{-2/3}\left[1+\frac{\sigma M_s-M_\beta\mp 1}{(\gamma-1)(\sigma M_s-M_\beta)}\right]\right\} \tag{A6}$$

$$\phi_{S,\alpha}=2\gamma\left[M_\alpha^2+\frac{1}{\gamma-1}\left(\frac{T_w-T_{aw}}{T}N_{Pr}^{-2/3}\right)_\alpha\right] \tag{A7}$$

$$\phi_{S,\beta}=2\gamma\left[M_\beta^2+\frac{1}{\gamma-1}\left(\frac{T_w-T_{aw}}{T}N_{Pr}^{-2/3}\right)_\beta\right] \tag{A8}$$

$$T_{aw}=T\left(1+\eta_r\frac{\gamma-1}{2}M^2\right) \tag{A9}$$

APPENDIX B

DERIVATION OF EQUATION FOR Z_N

The derivation for Z_I will be obtained and then generalized to arbitrary N. The wave diagram of figure 9(a) shows the location of the numbered points. The symbol x_6 denotes the distance of the point 6 from the origin, and so forth. The following equations are obtained by simple geometry from figure 9(a):

$$x_2 = U_{sI} t_2 \tag{B1}$$

$$x_2 = U_{sI} t_1 + U_{II}(t_7 - t_1) + (U+a)_I (t_2 - t_7) \tag{B2}$$

Combining equations (B1) and (B2) yields

$$\frac{t_7}{t_1} = \left[1 + \frac{U_{sI} - U_{II}}{U_{II} - (U+a)_I}\right] \frac{t_2}{t_1} - \frac{U_{sI} - U_{II}}{U_{II} - (U+a)_I} \tag{B3}$$

Also from figure 9(a),

$$x_{11} = U_{sI} t_{11} \tag{B4}$$

$$x_{11} = U_{sI} t_1 + U_{II}(t_7 - t_1) - U_{sI}(t_7 - t_{10}) + (U+a)_I (t_{11} - t_{10}) \tag{B5}$$

$$x_{11} = U_I t_{10} + (U+a)_I (t_{11} - t_{10}) \tag{B6}$$

Combining equation (B4) with equation (B6) and combining equation (B5) with equation (B6) yields

$$\frac{t_{11}}{t_{10}} = \frac{a_I}{(U+a)_I - U_{sI}} \tag{B7}$$

and

$$\frac{t_{10}}{t_1} = \frac{U_{sI} - U_{II}}{U_{sI} - U_I}\left(\frac{t_7}{t_1} - 1\right) \tag{B8}$$

Now

$$\frac{l_{11}}{l_1} = \frac{t_{11}}{t_1} = \frac{t_{11}}{t_{10}} \frac{t_{10}}{t_1} \tag{B9}$$

Substitution of equations (B3), (B7), and (B8) into equation (B9) produces

$$\frac{l_{11}}{l_1} = \frac{U_{sI} - U_{II}}{U_{sI} - U_I} \frac{a_I}{(U+a)_I - U_{II}}\left(\frac{t_2}{t_1} - 1\right) \tag{B10}$$

or

$$\frac{l_{11}}{l_1} = Z_I\left(\frac{l_2}{l_1} - 1\right) \tag{B11}$$

Since the origin in figure 9 could be shifted to any arbitrary location and the same geometrical relations above could be derived in the new location the generalized formula for Z_N can be written from inspection of equations (B10) and (B11) as

$$Z_N = \frac{U_{sN} - U_{N+1}}{U_{sN} - U_N} \frac{a_N}{(U+a)_N - U_{N+1}} \tag{B12}$$

REFERENCES

1. Trimpi, Robert L., and Cohen, Nathaniel B.: A Theory for Predicting the Flow of Real Gases in Shock Tubes With Experimental Verification. NACA TN 3375, 1955.
2. Mirels, Harold: Attenuation in a Shock Tube Due to Unsteady-Boundary-Layer Action. NACA Rep. 1333, 1957. (Supersedes NACA TN 3278.)
3. Hollyer, Robert N., Jr.: A Study of Attenuation in the Shock Tube. Project M720-4 (Contract No. N6-ONR-232-TO IV), Eng. Res. Inst., Univ. of Michigan, July 1953.
4. Glass, I. I., Martin, W., and Patterson, G. N.: A Theoretical and Experimental Study of the Shock Tube. UTIA Rep. No. 2, Inst. of Aerophysics, Univ. of Toronto, Nov. 1953.
5. Donaldson, Coleman duP., and Sullivan, Roger D.: The Effect of Wall Friction on the Strength of Shock Waves in Tubes and Hydraulic Jumps in Channels. NACA TN 1942, 1949.
6. Emrich, R. J., and Curtis, C. W.: Attenuation in the Shock Tube. Jour. Appl. Phys., vol. 24, no. 3, Mar. 1953, pp. 360–363.
7. Wheeler, Donald B., Jr.: Density Variation in Shock Tube Flow—A Comparison of Trimpi-Cohen Theory With Data of Mack. Tech. Rep. No. 8 (Contract N7 onr 39302), Inst. Res., Lehigh Univ., Aug. 15, 1956.
8. Boyer, D. W.: Effects of Kinematic Viscosity and Wave Speed on Shock Wave Attenuation. UTIA Tech. Note No. 8, Inst. of Aerophysics, Univ. of Toronto, May 1956.
9. Jones, Jim J.: Experimental Investigation of Attenuation of Strong Shock Waves in a Shock Tube With Hydrogen and Helium as Driver Gases. NACA TN 4072, 1957.
10. Emrich, Raymond J., and Wheeler, Donald B., Jr.: Wall Effects in Shock Tube Flow. The Physics of Fluids, vol. 1, no. 1, Jan.–Feb. 1958, pp. 14–23.
11. Huber, Paul W., and McFarland, Donald R.: Boundary-Layer Growth and Shock Attenuation in a Shock Tube With Roughness. NACA TN 3627, 1956.
12. Mirels, Harold, and Braun, W. H.: Nonuniformities in Shock-Tube Flow Due to Unsteady-Boundary-Layer Action. NACA TN 4021, 1957.
13. Cohen, Nathaniel B.: A Power-Series Solution for the Unsteady Laminar Boundary-Layer Flow in an Expansion Wave of Finite Width Moving Through a Gas Initially at Rest. NACA TN 3943, 1957.
14. Trimpi, Robert L., and Cohen, Nathaniel B.: An Integral Solution to the Flat-Plate Laminar Boundary-Layer Flow Existing Inside and After Expansion Waves and After Shock Waves Moving Into Quiescent Fluid With Particular Application to the Complete Shock-Tube Flow. NACA TN 3944, 1957.
15. Mirels, Harold: Boundary Layer Behind Shock or Thin Expansion Wave Moving Into Stationary Fluid. NACA TN 3712, 1956.
16. Gooderum, Paul B.: An Experimental Study of the Turbulent Boundary Layer on a Shock-Tube Wall. NACA TN 4243, 1958.
17. Rott, N., and Hartunian, R.: On the Heat Transfer to the Walls of a Shock Tube. Graduate School Aero. Eng., Cornell Univ. (Contract AF 33(038)-21406), Nov. 1955.
18. Rose, P. H.: Physical Gas Dynamics Research at the AVCO Research Laboratory. Res. Rep. 9, AVCO Res. Lab., May 1957. (Formerly AVCO Res. Note 37.)
19. Schlichting, H.: Lecture Series "Boundary Layer Theory." Part II—Turbulent Flows. NACA TM 1218, 1949.
20. Rubesin, M. W., and Johnson, H. A.: A Critical Review of Skin-Friction and Heat-Transfer Solutions of the Laminar Boundary Layer of a Flat Plate. Trans. A.S.M.E., vol. 71, no. 4, May 1949.
21. Sommer, Simon C., and Short, Barbara J.: Free-Flight Measurements of Turbulent-Boundary-Layer Skin Friction in the Presence of Severe Aerodynamic Heating at Mach Numbers From 2.8 to 7.0. NACA TN 3391, 1955.

TABLE I.—ATTENUATION FUNCTIONS AND COMPRESSIBILITY CORRECTIONS

$\frac{p_{\beta*}}{p_\infty}$	$(\Omega g)_{\alpha,1}$	$(\Omega g)_{\alpha,7}$	$(\Omega g)_{\alpha,13}$	$\Omega_{\alpha,1}$	$\Omega_{\alpha,7}$	$\Omega_{\alpha,13}$	$(\Omega g)_{\beta,1}$	$(\Omega g)_{\beta,7}$	$(\Omega g)_{\beta,13}$	$\Omega_{\beta,1}$	$\Omega_{\beta,7}$	$\Omega_{\beta,13}$	$(\Omega g)_{\alpha,1}+(\Omega g)_{\beta,1}$	$(\Omega g)_{\alpha,7}+(\Omega g)_{\beta,7}$	$(\Omega g)_{\alpha,13}+(\Omega g)_{\beta,13}$
1.00	0	0	0	1.000	1.000	1.000	0	0	0	1.000	1.000	1.000	0	0	0
1.25	−.0367	−.000223	−.0000410	.996	.980	.976	−2.627	−.0142	−.00255	1.004	1.018	1.022	−2.663	−.0144	−.00259
1.50	−.0844	−.000943	−.000200	.992	.962	.954	−3.775	−.0338	−.00695	1.006	1.032	1.038	−3.859	−.0348	−.00715
1.75	−.126	−.00200	−.000461	.989	.945	.933	−4.705	−.0549	−.0121	1.009	1.043	1.052	−4.832	−.0569	−.0126
2.0	−.161	−.00326	−.000795	.986	.928	.914	−5.531	−.0765	−.0176	1.011	1.052	1.064	−5.692	−.0797	−.0184
2.4	−.199	−.00531	−.00138	.981	.903	.884	−6.733	−.111	−.0269	1.014	1.065	1.080	−6.932	−.116	−.0282
2.6	−.210	−.00626	−.00167	.978	.891	.870	−7.302	−.128	−.0316	1.015	1.071	1.087	−7.512	−.135	−.0333
3.0	−.219	−.00785	−.00218	.974	.868	.843	−8.394	−.163	−.0412	1.017	1.081	1.099	−8.613	−.171	−.0434
3.6	−.205	−.00919	−.00267	.967	.835	.804	−9.961	−.214	−.0558	1.020	1.094	1.115	−10.166	−.224	−.0584
4.0	−.180	−.00925	−.00275	.963	.815	.780	−10.973	−.248	−.0655	1.022	1.102	1.125	−11.153	−.257	−.0683
5.0	−.081	−.00637	−.00199	.953	.765	.723	−13.444	−.332	−.0900	1.025	1.118	1.145	−13.525	−.339	−.0920
6.0	.056	.00008	.00003	.943	.719	.671	−15.860	−.416	−.114	1.028	1.131	1.161	−15.804	−.415	−.114
7.0	.214	.0115	.00376	.933	.675	.622	−18.243	−.498	−.136	1.031	1.142	1.175	−18.029	−.486	−.132
8.0	.386	.0255	.00863	.924	.634	.576	−20.603	−.580	−.163	1.033	1.152	1.187	−20.217	−.555	−.154
9.0	.560	.0418	.0144	.914	.596	.534	−22.953	−.661	−.187	1.035	1.160	1.197	−22.393	−.620	−.173
10.0	.736	.0600	.0210	.905	.559	.494	−25.292	−.743	−.211	1.036	1.168	1.207	−24.556	−.683	−.190
12.0	1.072	.0995	.0357	.886	.490	.422	−29.945	−.904	−.259	1.039	1.180	1.222	−28.873	−.804	−.224
15.0	1.514	.160	.0592	.859	.401	.330	−36.911	−1.143	−.331	1.043	1.194	1.240	−35.397	−.983	−.271
20.0	1.756	.213	.0808	.812	.278	.212	−49.167	−1.559	−.454	1.047	1.211	1.261	−47.411	−1.346	−.373

U.S. GOVERNMENT PRINTING OFFICE: 1961